Universitatea
Transilvania
din Brașov

HABILITATION THESIS

The use of lightweight structures and optimization methods – a need for a more effective engineering

Domain: Mechanical Engineering

Assoc. Prof. Dr. Eng. Marian Nicolae Velea

Transilvania University of Brasov

BRAŞOV, 2024

CONTENTS

(A) Rezumat

Această teză de abilitare descrie realizările științifice și profesionale atinse de autor între anii 2012 și 2024 și este structurată în cinci capitole legate de domeniile structurilor ușoare și metodelor de optimizare.

Primul capitol prezintă conceptul de structuri sandwich ierarhice și contribuția autorului în acest domeniu. A fost dezvoltată o structură sandwich ierarhică de ordinul doi, realizată din polimeri termoplastici auto-ranforsați printr-un proces de pliere continuă și analizată în comparație cu alte soluții existente din perspectiva rezistenței și rigidității statice, precum și din perspectiva capacității de absorbție a energiei de impact.

Al doilea capitol descrie conceptul de structuri hibride. O abordare practică este parcursă aici pentru a demonstra beneficiile utilizării PET-ului armat cu fibră de carbon atunci când este utilizat pentru a înlocui oțelul în componentele structurale. Alte două studii de caz investigate în acest capitol sunt legate de dezvoltarea unui șurub cu bile cu arbore din CFRP și piuliță din oțel precum și dezvoltarea unei flanșe de roată, ambele produse fiind supuse unor cereri de brevet de invenție.

Al treilea capitol tratează tema optimizării structurilor și sistemelor mecanice și este împărțit în patru subcapitole: descrierea temei, optimizarea parametrică, optimizarea neparametrică și optimizarea multi-obiectiv.

O scurtă descriere a ceea ce înseamnă procesul de optimizare în cadrul dezvoltării unui produs mecanic este dată mai întâi, arătând care sunt pașii necesari pentru definirea și rezolvarea unei probleme de optimizare.

Legat de subiectul optimizare parametrică, sunt abordate două cazuri de studiu. Primul caz este legat de optimizarea grafică, pe baza unui model analitic, a rigidității și rezistenței în raport

cu masa proprie a unei structurii sandwich ierarhice de ordinul doi realizată din polimeri termoplastici auto-ranforsați. Al doilea caz de studiu abordează problema optimizării unui sistem mecanic, cu scopul de a demonstra funcționalitatea conceptului și de a crește eficiența acestuia încă din faza de dezvoltare conceptuală.

Subiectul de optimizare neparametrică este acoperit de un caz de studiu legat de optimizarea topologică a unui vas sub presiune de înaltă temperatură din cadrul unei pompe de căldură ThermoLift de 20 kW. Pe lângă optimizarea topologică, sunt abordate pe scurt și celelalte tehnici de optimizare neparametrică existente: optimizarea formei, optimizarea topografică, optimizarea grosimii și optimizarea liberă a dimensiunii.

Optimizarea multi-obiectiv este mai întâi descrisă succint din punct de vedere teoretic, indicând modul în care trebuie interpretat rezultatul unei astfel de optimizări. În continuare, este discutată contribuția autorului în cadrul proiectului de cercetare intitulat OptFRPBody (Optimization of Body in FRP-Composite for small Electric Vehicle), la KTH – Royal Institute of Technology, Department of Aeronautical and Vehicle Engineering. Un alt studiu de caz prezentat se referă la optimizarea multi-obiectiv a îmbinărilor hibride oțel-compozit solicitate termo-mecanic.

În cele din urmă, sunt detaliate evoluția și planurile de dezvoltare pentru dezvoltarea carierei autorului.

(A) Summary

This habilitation thesis describes the scientific and professional achievements reached by the author within 2012 and 2024 and it is organized in five chapters which are related to the fields of lightweight structures and optimization methods.

The first chapter presents the concept of hierarchical sandwich structures and the contribution of the author in this field. A second order hierarchical sandwich structure made of self-reinforced polymers by means of a continuous folding process was developed and analyzed in comparison with other existing solutions from a static strength and stiffness perspective, as well as from the impact energy absorption capacity perspective.

The second chapter describes the concept of hybrid structures. A practical approach is used here to prove the benefits of using carbon fiber reinforced PET when used to substitute steel in structural components. Another two investigated case studies in this chapter are related to the development of a hybrid ball screw drive with CFRP shaft and steel nut and the development of a hybrid wheel flange, both products being subjected to patent applications.

The third chapter discusses the topic of optimization of mechanical structures and systems, and it is split into four sub-chapters: the description of the topic, the parametric optimization, the non-parametric optimization and the multi-objective optimization.

A short description of what the optimization process means within the development of a mechanical product is given first, by showing what are the required steps for defining and solving an optimization problem.

Related to the parametric optimization subject, two study cases are addressed. The first one is related to the stiffness and strength graphical optimization of the second order hierarchical sandwich structure made of self-reinforced polymers based on an analytical model. The

second study case is addressing the problem of mechanical system optimization, with the aim of proving the functionality of the concept and of increasing its efficiency.

The non-parametric optimization subject is covered by a study case related to the topology optimization of high-temperature pressure vessel of a 20KW ThermoLift Heat Pump. Apart from the topology optimization, the other existing non-parametric optimization techniques are shortly addressed: shape optimization, topography optimization, size optimization and free-size optimization are shortly addressed.

The multi-objective optimization is first described from a theoretical point of view, indicating how the result of such optimization needs to be interpreted. Further on, the contribution of the author within the research project entitled *OptFRPBody* (Optimization of Body in FRP-Composite for small Electric Vehicle), at KTH – Royal Institute of Technology, Department of Aeronautical and Vehicle Engineering, is further on discussed. Another presented case study refers to the multi-objective optimization of thermally stressed steel-composite hybrid joints. Eventually, the evolution and development plans for future career development of the author are detailed.

(B) Scientific and professional achievements and the evolution and development plans for career development

(B-i) Scientific and professional achievements

Introduction

The scientific and professional achievements presented in this habilitation thesis are registered in the period 2012-2024. The topics addressed are related to the field of lightweight structures and optimization methods and there are structured in five main categories:

- Hierarchical sandwich structures,
- Hybrid structures,
- Parametric optimization,
- Non-parametric optimization,
- Multi-objective optimization.

Thus, the following five chapters will detail the actual contributions of the author in these fields.

1 Hierarchical sandwich structures

1.1 Description of the topic

One way to reduce the vehicles' parts weight is to use materials that provide higher specific stiffness and strength to weight ratios. Therefore, material (re)selection represents an important weight optimization criterion and composite materials having improved mechanical properties are usually searched (M. F. Ashby, 2011). However, apart from material type, shape criterion is also important, and it may represent an added advantage (M. F. Ashby, 2013; M. F. Ashby & Bréchet, 2003). An example of a near optimal use of material is given by the sandwich concept (Zenkert, 1997) where the bending stiffness of the structure is increased by placing a lightweight and thicker core between two thin and stiff face sheets while the weight is negligibly increased. The continuing research on improving the overall mechanical performance of sandwich structures focuses also on developing novel core configurations, made of composite materials, to gain an improved mechanical behavior of the core. Examples of such efforts include composite corrugated cores (Russell et al., 2010), square honeycomb cores (Russell et al., 2011), rhombic and Kagome honeycombs (X. Zhang & Zhang, 2013), pyramidal lattice truss cores (Kooistra & Wadley, 2007; Queheillalt et al., 2008; Y. Sun & Gao, 2013; Wadley & Kooistra, 2009; Xiong et al., 2010; G. Zhang et al., 2013) or novel expanded cores(Velea et al., 2012; Velea & Lache, 2011). Although many of these structures provide competitive weight specific strength and stiffness, their main drawback is related to manufacturing steps which are often complicated and difficult to be integrated within a continuous production line. The more recent development of additive manufacturing technologies allows generating complicated and efficient cellular shapes but on a limited scale yet (Dragoni, 2013; Rezaei et al., 2016).The hierarchical sandwich concept has been introduced as a solution to increase the in-plane shear and the out of plane compression performance (Fan et al., 2014; Kazemahvazi et al., 2009; Kazemahvazi & Zenkert, 2009; Kooistra et al., 2007; Yin et al., 2013). The up to date developed hierarchical sandwich structures are obtained by assembling at least three separate components through a specific joining method, the contact area being placed within geometric planes that are parallel to the middle surface of the structure. This configuration leads to a disadvantageous way of transferring loads between components because the in-plane shear behavior of the structure is influenced by the shear properties of the joint. Moreover, the recycling capability represents another important issue which is currently difficult to deal with as typical hierarchical sandwich structures consist of several different materials.

1.2 Achievements

I. Second order hierarchical sandwich structure made of self-reinforced polymers by means of a continuous folding process (Velea et al., 2016)

In this study a novel second order hierarchical sandwich structure and its manufacturing principle were described. The whole hierarchical structure is made of a fully recyclable material – different forms of poly-ethylene terephthalate (PET): PET matrix, reinforced with PET fibers (Self reinforced - SrPET) and PET foam resulting in a recyclable structure. The manufacturing path is developed such that it can be implemented within a continuous production line. Out-of-plane compression tests were carried out in order to determine the stiffness and strength properties of the proposed structure. An analytical model is developed for evaluating the out-of-plane stiffness and strength properties and used for investigating the influence of the geometric parameters on the structural performance of the proposed hierarchical sandwich structure.

The second order hierarchical sandwich structure is obtained through a continuous flow of operations described further on, related to Figure 1.

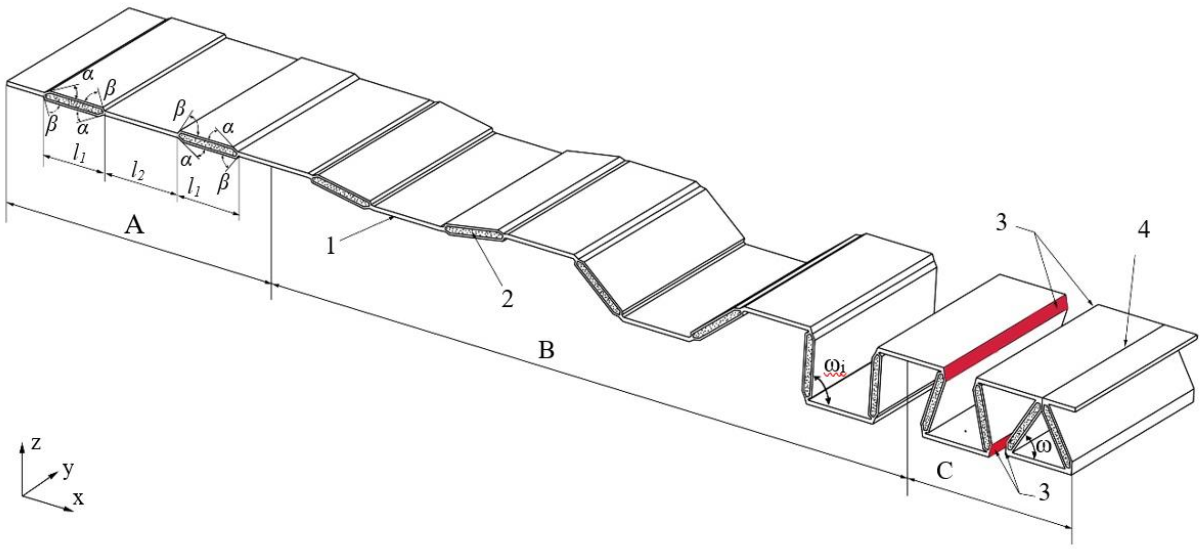

Figure 1 Schematic illustration of the manufacturing principle for the second order hierarchical sandwich structure

The process starts with the first phase (A) from a single sheet material which contains monolithic (1) and sandwich sections (2) arranged in an alternative way; the folding begins within the second phase (B) where the sandwich sections (2) are rotated along their edges with an angle equal to $90+\omega-\alpha$. The joining (4) of the sandwich sections is made within phase (C) through the contact areas (3) which are placed perpendicular to the neutral plane of the structure and which are obtained by the definition of the α and β angles in terms of the desired final angle ω and of the sandwich sections length l2.

The used SrPET composite material (poly-ethylene terephthalate fibres (SrPET) and poly-ethylene terephthalate foam (PET)) proves to be a good alternative with respect to lightweight design but also considering its lower life cycle environmental impact (Poulikidou et al., 2015) an high impact energy absorption capacity (Kazemahvazi et al., 2015a). The SrPET composite consists of a low melting temperature matrix PET (termed LPET) and a high tenacity PET (termed HTPET) as fibre material. The LPET is chemically modified to melt at approximately 170°C whereas the HTPET melts at 260°C. During consolidation, the temperature should be as high enough to melt the LPET and wet the fibres but not too high so that the HTPET fibres degrade and lose their reinforcing properties. A previous study showed that laminates with good mechanical properties can be consolidated at 220°C for 20min under a pressure of 1.5bar above ambient pressure (Schneider et al., 2013). The SrPET material used in this study is a commingled balanced 2/2 twill fabric with an areal weight of 0.75kgm-2 and 50% reinforcement fibres measured by weight (supplied by Comfil®APS (Comfil® APS. Thermoplastic Composites Denmark, www.comfil.biz, 2014)). Using the above-mentioned process parameters, one layer of woven fabric results in a lamina with a thickness of 0.45mm and a material density of 1380kgm-3.

The compression modulus and ultimate compression strength for the SrPET composite is 5.3±0.2GPa and 94.7±0.7MPa, respectively. A material yield point is observed at 35MPa after which the stiffness of the material reduces and results in softening. For details on test procedures and specimens dimension readers are referred to previous work performed by Schneider et al (Kazemahvazi et al., 2015b; Schneider et al., 2013).

The foam used is an ArmaForm PET AC with a density of 100kgm-3. According to the manufacturer reference, the compression modulus is 105MPa, the shear modulus is 25MPa while the compression strength is 1.5MPa and the shear strength is 0.9MPa (*Armacell Benelux. ArmaFORM PET/W Technical Data, Rue de Trois Entities 9-B-4890 Thimister Clermont. <www.Armacell.Com> [Accessed 02.04.2014].*, n.d.).

No additional materials are used for joining.

A hot-press is used for consolidating the SrPET fabric and at the same time joining it with the foam, thus the unfolded plate containing the alternative monolithic and sandwich sections results. Firstly, the bottom aluminum profiles (see Figure 2) are arranged parallel to each other at a specific offset in such way to allow the profiled PET foam and the layer(s) of fabric to fit in between.

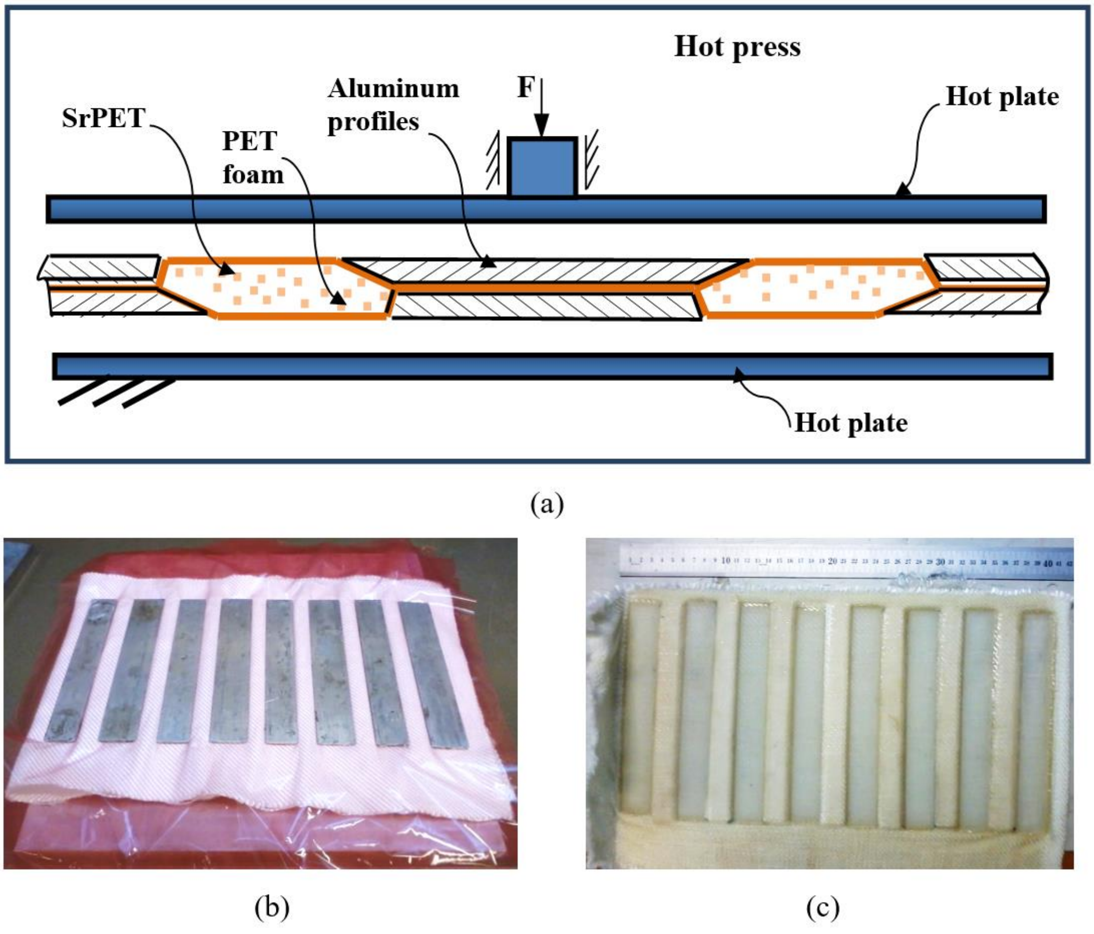

Figure 2 (a)Schematic illustration for the manufacturing of the unfolded structure (b) positioning the foam profiles and the fabric between the aluminum profiles; (c) consolidated plate with alternative monolithic and sandwich sections

Secondly, the top aluminum profiles are aligned correspondingly, being guided by the edges of the profiled foam covered with the fabric. A release film is used between the aluminum profiles and the fabric. The previously described package is placed in the hot-press where it is heated up to 220°C within a heating rate of 20°Cmin^{-1}, it is held at 220°C under a pressure of 1.5bar above the ambient pressure for 20min and cooled to room temperature. The resulted consolidated plate is extracted from the hot-press; cross-section within the resulted consolidated plate with alternative monolithic and sandwich sections is presented within Figure 4.

Figure 3 Cross-section within the resulted consolidated plate with alternative monolithic and sandwich sections

Different values for the geometric parameters l1 and l2 are possible to be obtained by arranging the aluminum profiles having the same shape and same cross-section as shown within Figure 4.

Figure 4 (a) single aluminum profile – l_2 ; (a) grouped aluminum profiles – $3l_2$

The resulting second order hierarchical corrugated sandwich structure results by simply folding the consolidated plate described in Figure 3. Starting from the consolidated plate (see Figure 5), the folding edges are locally heated until the PET matrix is softened. The sandwich sections are then bent around the folding lines until they close the triangle and form the unit cell. The joining between the folded sections is formed with no additional material (see Figure 5), just by means of the melted PET matrix.

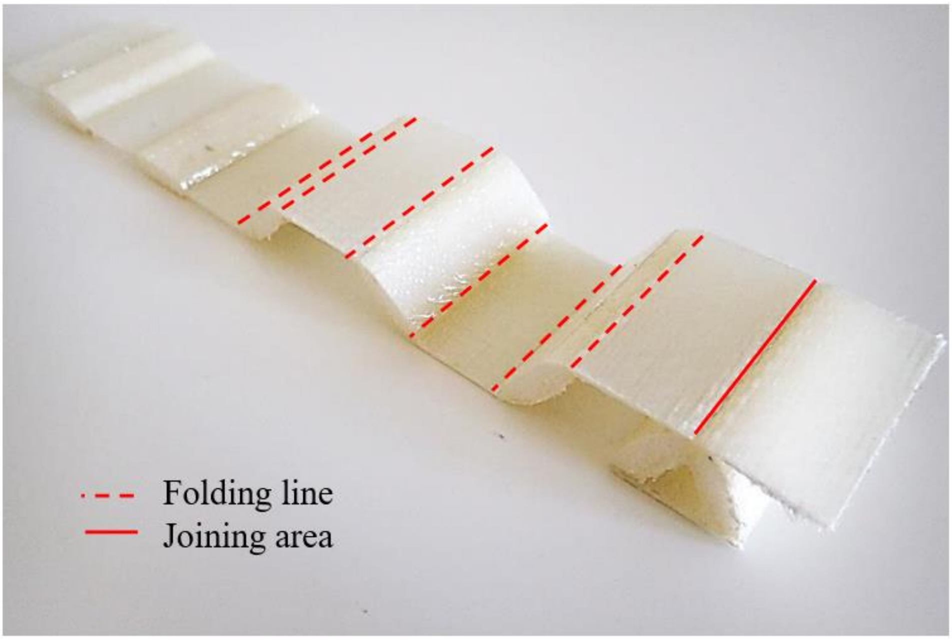

Figure 5 Folding the consolidated laminate with foam inserts to a hierarchical sandwich structure

Figure 6(a) illustrates the resulted hierarchical sandwich structure after the folding process is finished. A more detailed image of the joining area is given in Figure 7(b). Apart from the material joining, there is a mechanical interlocking between the sandwich sections that contributes to a better load transfer within the structure. In terms of a specific application, the resulting structure might be used as it is, meaning that the thickness of the monolithic sections can play the role of the structural face sheets or, if required, additional structural face sheets can be added.

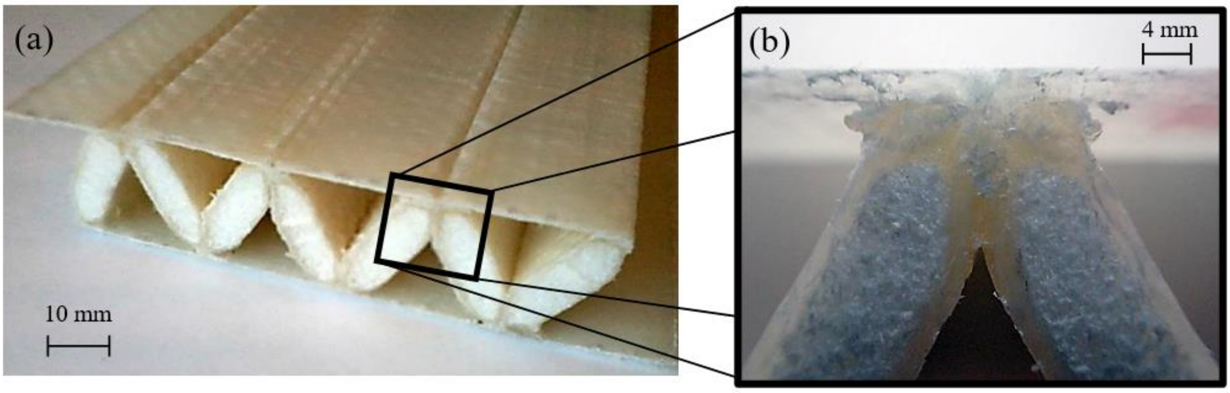

Figure 6 (a) The resulted hierarchical sandwich structure (b) Cross section within the joining area

The parameterized topology of the unit cell is shown in Figure 7, where: l_1 – length of the sandwich section, l_2 – length of the monolithic section, h – height of the sandwich unit cell, t_c – thickness of the foam, t_f – thickness of the face sheets, ω – folding angle.

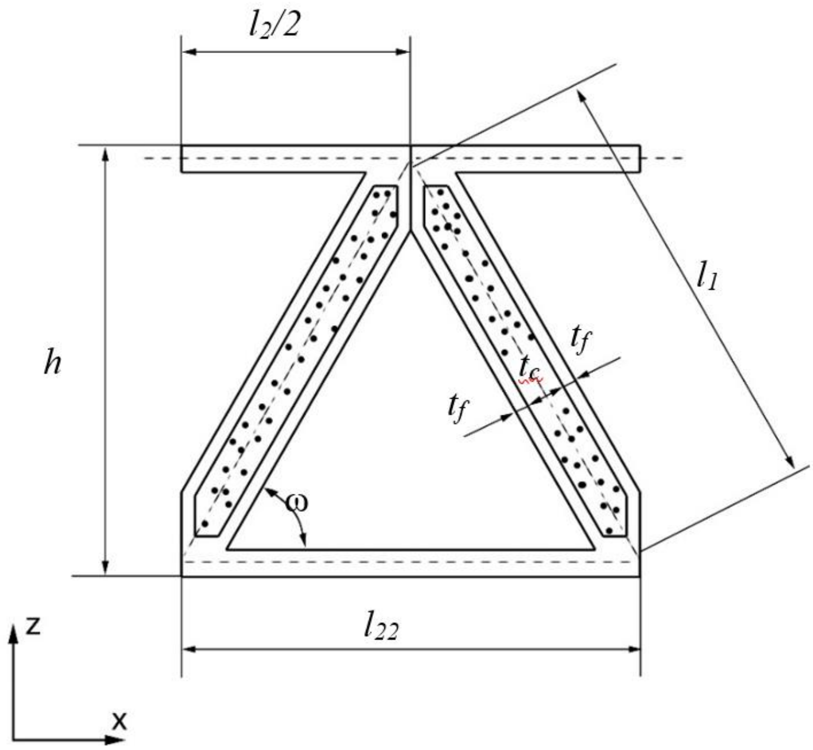

Figure 7 Unit cell and its geometric parameters. The dotted area is representing the structural foam

The relative density of the sandwich ρ_r is defined with:

$$\rho_r = \frac{l_1\left(t_c + 2t_f + 4t_f \cos\ \omega\right) + 4{t_f}^2}{\left(t_f + l_1 \cos\omega\right)\left(4t_f + l_1 \sin\omega\right)} \tag{1}$$

The density of the structure, including the monolithic elements (e.g. face sheets), can be derived further on by:

$$\rho = \rho_r\left(\rho_{solid}\frac{V_{solid}}{V_{structure}} + \rho_{foam}\frac{V_{foam}}{V_{structure}}\right) \tag{2}$$

where

- ρ_{solid} – represents the density of the solid material
- ρ_{foam}– represents the density of the foam
- V_{solid}= $(4t_f(l_1+l_2)+t_c(t_f/2\cos\omega+t_f/2\sin\omega))b$; V_{foam}= $2l_1 t_c b$; $V_{structure}$= bhl_2 , where b is the unit cell width and V comes from *Volume*.

The out-of-plane compression properties are evaluated through experimental tests using a hydraulic Walter + Bai testing machine with a load cell of 63kN. The tests were displacement driven with a constant crosshead speed of 2mm min-1.

The experimental investigation is done on unit cells. However, in order to avoid the edge effects, each specimen is glued using epoxy-based glue - Araldite®- on a metal block having a U shape thus simulating the continuity of the structure (see Figure 8).

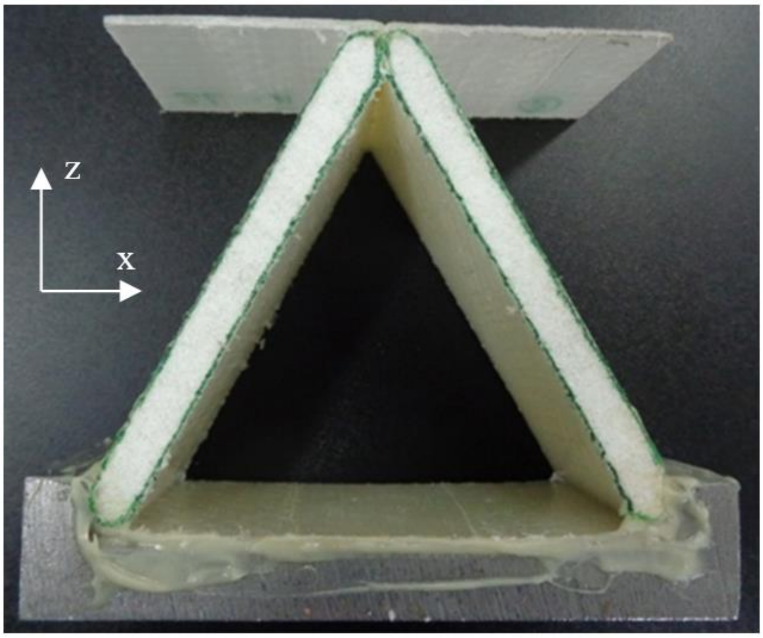

Figure 8 Specimen used for mechanical testing in out of plane compression

The effective elastic modulus Ez and the ultimate strength σz are determined based on the measured reaction force correlated with the imposed displacement and the specimens' geometric dimensions.

Four geometric configurations were tested by varying the value of foam thickness tf and length l1, (see Table 1). These configurations were possible to be made with the same shape for the aluminium profiles as shown in Figure 4. Three specimens have been tested for each geometric configuration.

Table 1 Geometric configurations investigated experimentally

Configuration	t_f [mm]	l_1 [mm]	t_c [mm]	ρ_r [-]	ρ [kgm^{-3}]
I	0.45	24	7.1	0.738	232
II	0.90	25	6.2	0.715	346
III	0.45	81	7.1	0.245	23
IV	0.90	82	6.2	0.259	41

The effective compressive elastic modulus is theoretically obtained by means of an analytical model based on elementary sandwich beam theory. Similar investigations were carried by Kazemahvazi et. al (Kazemahvazi & Zenkert, 2009) for corrugated cores and by Yin et. al (Yin et al., 2013) for pyramidal cores with sandwich core members.

Assuming an unit imposed displacement δz applied on the unit cell a total reaction force Fz results (see Figure 9).

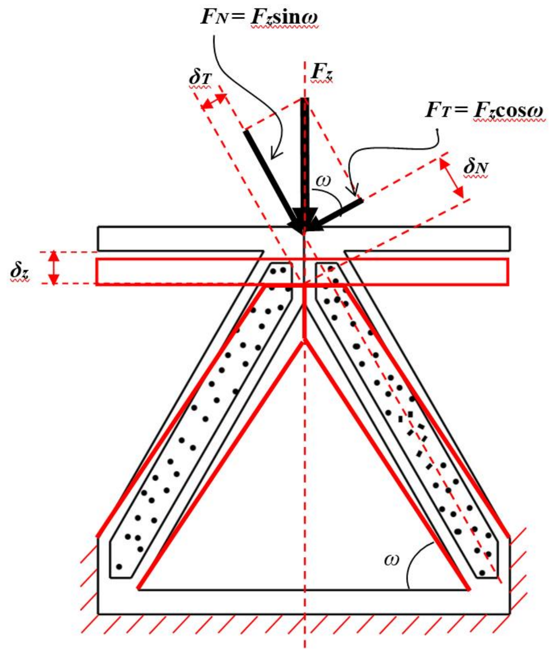

Figure 9 Unit cell under out-of-plane compression loading

Due to the structures' symmetry the analytical model can be built by analysing the deformation of a single sandwich strut. When looking at the right-hand side sandwich strut the reaction force Fz can be decomposed in the two components: F_N – representing the force acting along the sandwich strut and F_T – representing the force acting perpendicular to the sandwich strut, where $Fz=F_N\sin\omega + F_T\cos\omega$.

Based on the sandwich beam theory (Zenkert, 1997), the resulted forces F_N and F_T may be calculated according to Equations (3) and (4):

$$F_T = \frac{\delta_T}{\frac{l_1^3}{3D} + \frac{l_1}{S}} \tag{3}$$

$$F_N = \frac{A\delta_N}{l_1} \tag{4}$$

where:

- $\delta_N = \delta_z \sin\omega$; $\delta_T = \delta_z \cos\omega$
- $A = 2t_f E_f$, represents the extensional stiffness
- $D = \frac{E_f t_f (t_c + t_f)^2}{2}$, represents the bending stiffness
- $S = \frac{G_c (t_c + t_f)^2}{t_c}$, represents the shear stiffness
- l_1 represents the length of the strut (see Figure 9).

The nominal stress that occurs within the investigated structure is

$$\sigma_z = \frac{F_z}{2l_1 \cos\omega} \; . \tag{5}$$

The nominal strain within the structure is defined as:

$$\varepsilon_z = \frac{\delta_z}{h} \; . \tag{6}$$

The effective elastic modulus in out of plane compression E_z is defined as:

$$E_z = \frac{\sigma_z}{\varepsilon_z} \; . \tag{7}$$

Eventually, from Equations (3)-(6), E_z becomes:

$$E_z = \frac{\sin\omega \left(\frac{\cos\omega^2}{\frac{2l_1^3}{3E_f t_f (t_c + t_f)^2} + \frac{l_1 t_c}{G_c (t_c + t_f)^2}} + \frac{2E_f t_f \sin\omega^2}{l_1} \right)}{\cos\omega} \; . \tag{8}$$

The out-of-plane compressive strength of the hierarchical sandwich structure made of self-reinforced polymers is determined here based on the previous work of Yin et al. (Yin et al., 2013, 2014) and Kazemahvazi et al. (Kazemahvazi & Zenkert, 2009). Four failure modes are considered when calculating the theoretical strength: local buckling, general buckling, core shear buckling and shear failure of the core.

- *Local buckling*

  The face sheets of the sandwich core element can buckle when they are relatively thinner due to the existing in-plane loads. When such a failure mode occurs, the out-of-plane strength of the structure can be determined through Equation (9):

$$\sigma_z = \frac{\sqrt[3]{E_f E_c G_c} t_f \sin\omega \left(\frac{\cos\omega^2}{\frac{l_1^2 \sin\omega^2}{3\left(t_c + t_f\right)^2} + \frac{t_c}{G_c\left(t_c + t_f\right)^2}} + 1 \right)}{\cos\omega\left(l_1 + 2t_f\right)} \quad . \tag{9}$$

- *General Buckling of sandwich struts*

  For longer sandwich struts and lower core thicknesses, the expected failure mode is general buckling. The compressive strength of the hierarchical structure is therefore determined by Equation (10):

$$\sigma_z = \frac{2E_f \pi^2 t_f \sin\omega \left(t_c + t_f\right)^2 \left(\frac{\cos\omega^2}{\frac{l_1^2 \sin\omega^2}{3\left(t_c + t_f\right)^2} + \frac{t_c}{G_c\left(t_c + t_f\right)^2}} + 1 \right)}{l_1^2 \cos\omega\left(l_1 + 2t_f\right)} \quad . \tag{10}$$

- *Core shear buckling*

  The compressive strength of the hierarchical structure in case when the shear buckling failure of the sandwich struts occur can be determined by Equation (11):

$$\sigma_z = \frac{G_c t_c \tan\omega \left(\dfrac{\cos\omega^2}{\dfrac{l_1^2 \sin\omega^2}{3\left(t_c + t_f\right)^2} + \dfrac{t_c}{G_c\left(t_c + t_f\right)^2}} + 1 \right)}{l_1 + 2t_f} \quad . \tag{11}$$

- *Shear failure of core*

  This failure mode occurs when the shear stress in the core equals the shear strength of the core material [19]. The compressive strength of the hierarchical structure can be calculated using Equation (12):

$$\sigma_z = \frac{\tau_c t_c \left(t_c - \dfrac{\dfrac{G_c l_1^2 (\cos\omega^2 - 1)}{3}}{G_c \cos\omega^2 \left(t_c + t_f\right)^2} + 1 \right)}{l_1 + 2t_f} \quad . \tag{12}$$

Figure 10 shows the experimental compressive stress-strain response for the configuration I and III where tf = 0.45mm, Table 1; this value for tf corresponds to a single layer of SrPET material. As expected, lower values for the tc/l1 ratio will provide higher ultimate strength, 2.9 MPa vs. 1.6 MPa.

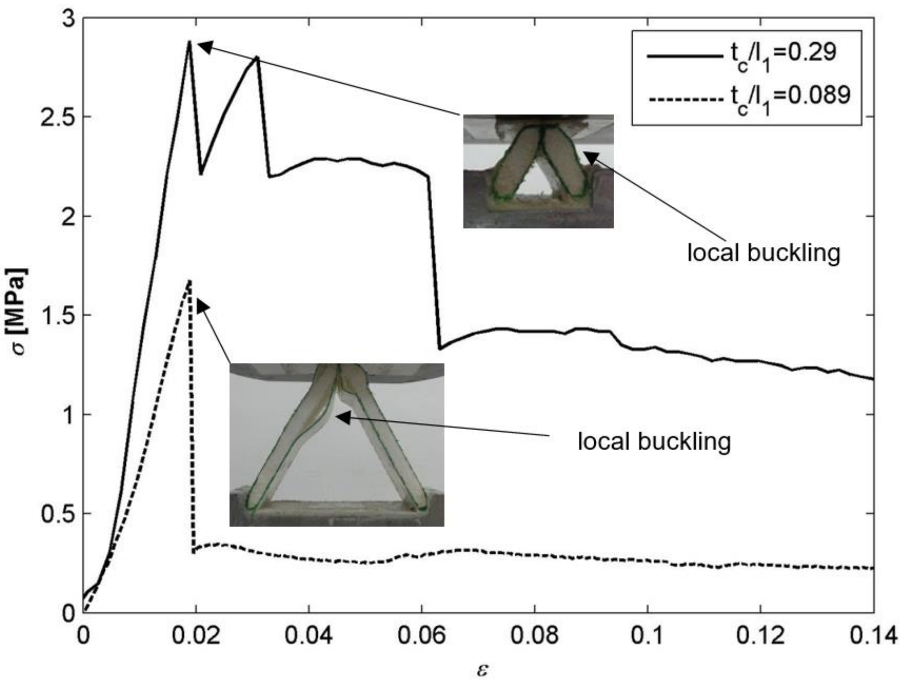

Figure 10 Out-of-plane compression stress –compression strain response fort he investigated geometric configurations I and III, Table 1.

However, the resulting specific strength indicates approximately the same performance for both I and III geometric configurations, see Table 2. Local buckling failure mode is found when testing both configuration I and III. The determined out-of-plane compression stiffness values Ez indicates a more than two times increase for configuration I with respect to configuration III. However, this ratio is inversed when it comes to the specific stiffness, and it has a value of 3.8 (see Table 2), meaning that a higher stiffness performance with respect to weight is offered by configuration III.

The experimental results obtained for the investigated geometric configurations II and IV where tf = 0.9mmare presented within Figure 11.

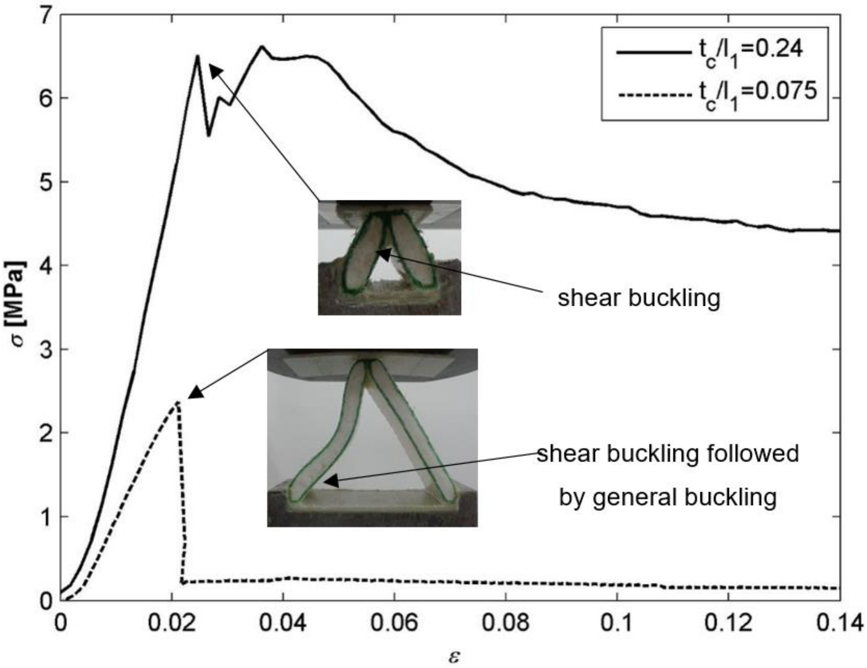

Figure 11 Out-of-plane compression stress – compression strain response for the investigated geometric configurations II and IV (see Table 1).

The strength behavior is similar with the one for configurations I and III only that the recorded magnitudes are higher for II and IV (6.5MPa and 2.2MPa respectively), as expected. The shear buckling failure mode is found for both configurations II and IV. However, for a lower t_c/l_1 ratio, the general buckling of the sandwich strut was recorded as a post-failure mode (see Figure 11).

The obtained stiffness is approximately two times higher for configuration II compared to configuration IV. When it comes to the weight specific stiffness, the value is four times higher for configuration IV compared to configuration II, see Table 2.

Table 2 Stiffness and strength results

Config	Experimental results					Analytical predictions	
	E_z [MPa]	σ_z [MPa] / Failure mode	E_z/ρ [MPa / kg m^{-3}]	σ_z/ρ [MPa / kg m^{-3}]		E_z [MPa]	σ_z [MPa] / Failure mode
I	185	2.9 / Local buckling	0.79	0.012		236.9	6.2 / Local buckling 419/ General buckling 10.3 / Shear buckling 24.6 / Core shear
II	271	6.5 / Shear buckling	0.78	0.019		455	11.4 / Local buckling 336/ General buckling 8.3 / Shear buckling 20 / Core shear
III	70	1.6 / Local buckling	3.02	0.069		73	1.9 / Local buckling 11.8/ General buckling 3.1 / Shear buckling 7.5 / Core shear
IV	141	2.2 / Shear buckling	3.42	0.054		142	3.7 / Local buckling 11/ General buckling 2.6 / Shear buckling 6.4/ Core shear

Figure 12 illustrates, based on the developed analytical model, the way the out-off plane stiffness is influenced by ω angle and by the t_c/l_1 ratio, where t_c=8-2t_f with t_f= 0.45 for geometric configurations I and III and t_f= 0.9mm for geometric configurations II and IV (see Figure 10).As expected, E_z is increasing with the increase of ω angle. Moreover, higher values for the t_c/l_1 provide higher stiffness properties but also higher densities.

A good agreement was found between the analytical model and the experimental results for geometric configurations III and IV (longer sandwich core elements). However, differences were found between the analytical model and the experimental results for geometric configurations I and II, mainly due to manufacturing of the specimens with higher t_c/l_1 ratios (shorter sandwich core elements). One issue is the misalignment of folding edges during the folding process which was difficult to control for higher t_c/l_1 ratios.

The misalignment is causing a not even distribution of the load on the sandwich struts during testing of the specimens. Another issue is related to the obtained ω angle for the specimens that vary from 55° to 60°. Apart from the geometric imperfections, material imperfections also occur with an important contribution to the structure's behavior: the foam core degrades during manufacturing and the resulted bonding is not perfect at the sides which can initiate a premature failure.

The out-of-plane stiffness of the investigated structure is compared as function of density with several cellular structures in Figure 12. The investigated configurations III and IV show a higher stiffness compared with the commercially available foam structures (Armacell Benelux. ArmaFORM PET/W Technical Data, Rue de Trois Entities 9-B-4890 Thimister Clermont. <www.Armacell.Com> [Accessed 02.04.2014]., n.d.; DIAB Group. Divinycell® H Technical Data, SE-31222 Laholm, Sweden, <www.Diabgroup.Com> [Accesed 21.11.2013], n.d.; Evonik Industries AG, ROHACELL® IG/IG-F Properties, 64293 Darmstadt, Germany. <www.Rohacell.Com> [Accesed 21.11.2013], n.d.) and with the pyramidal cores made of Titanium alloy (Queheillalt & Wadley, 2009) and carbon fiber composite (Xiong et al., 2010) at similar densities.

However, another pyramidal carbon fiber composite structure proposed by Li, M., et al. (Li et al., 2011) indicates a significantly higher stiffness at approximately the same density. The configurations I and II reach higher stiffness values but also higher densities.

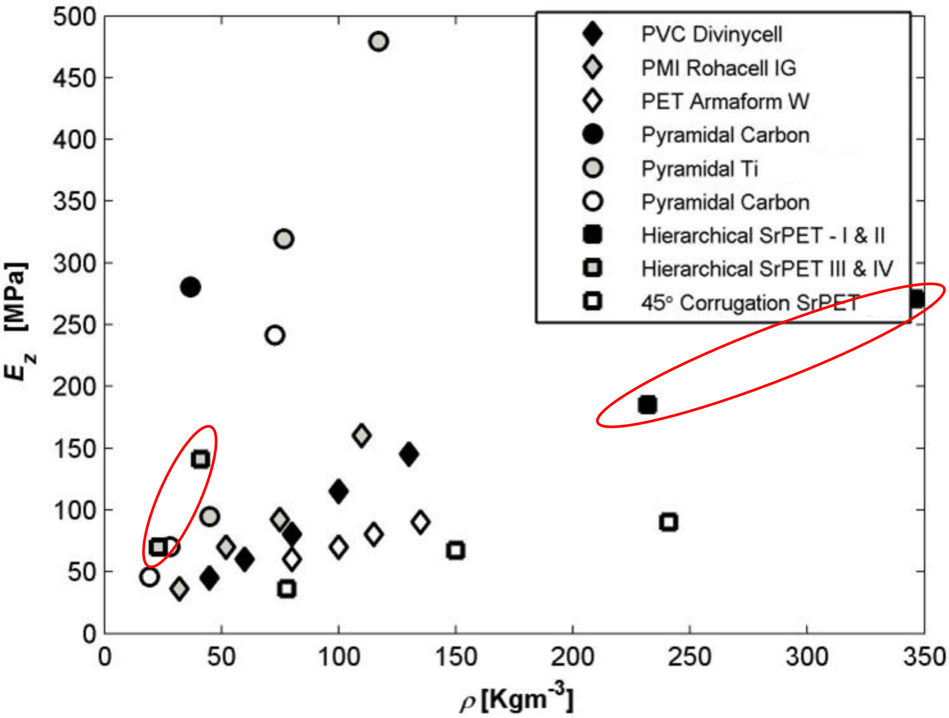

Figure 12 Stiffness properties as a function of structures' density

The out-of-plane strength of the investigated structure is compared as function of density with several cellular structures in Figure 13. At lower densities, configurations III and IV indicate higher strength than the Titanium lattice structures (Queheillalt & Wadley, 2009) and similar strength compared to the tetrahedral structure made from aluminum (Kooistra et al., 2004). Higher strength performance is found at lower densities compared with the commercial foam structures (Armacell Benelux. ArmaFORM PET/W Technical Data, Rue de Trois Entities 9-B-4890 Thimister Clermont. <www.Armacell.Com> [Accessed 02.04.2014]., n.d.; DIAB Group. Divinycell® H Technical Data, SE-31222 Laholm, Sweden, <www.Diabgroup.Com> [Accesed 21.11.2013], n.d.; Evonik Industries AG, ROHACELL® IG/IG-F Properties, 64293 Darmstadt, Germany. <www.Rohacell.Com> [Accesed 21.11.2013], n.d.) . A small increase in strength is found at higher densities for configuration III and IV resulting in a worse strength performance compared to the other types of structures.

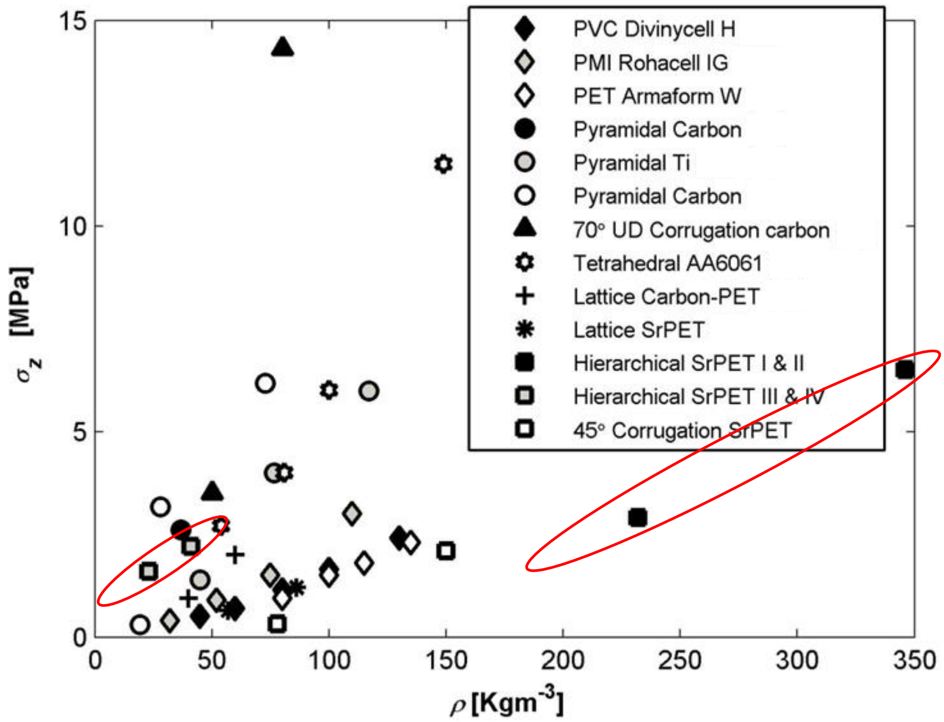

Figure 13 Strength properties as a function of structures' density

The experimental investigations indicate that the best performance with respect to the weight specific stiffness is offered by configuration IV. When it comes to weight specific strength, the best performance is given by the geometric configuration III. It results that the investigated structure is very competitive at lower densities.

As shown by other authors, the SrPET material is suitable for impact energy absorption applications due to a high ductility characteristic; the herein proposed arrangement of the material may be an added advantage with respect to impact performance. This conclusion has led to the next study which is related to the investigation of the specific impact performance.

A patent of invention has been published for the herein presented and analysed hierarchical sandwich structure 2018 (Velea et al., 2018). An extract from this patent of invention is shown in Figure 14.

RO 130161 B1

(51) **Int.Cl.**
B32B 1/04 (2006.01)

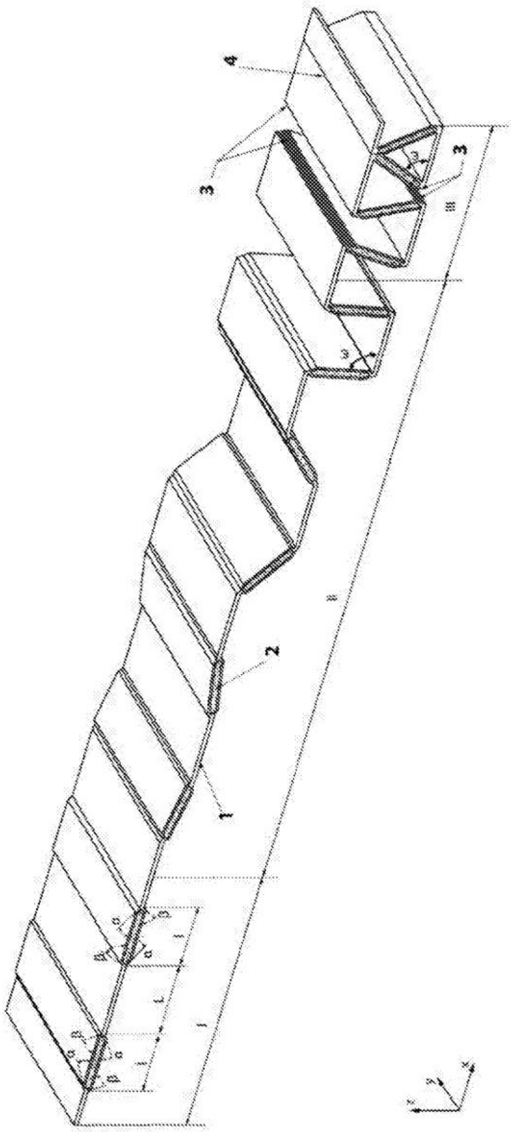

Fig. 1

6

Figure 14 Extract from the obtained patent of invention

II. *Energy absorption of all-PET 2nd order hierarchical sandwich structures under quasi-static loading conditions (Velea & Lache, 2019a)*

Apart from high strength and stiffness to weight ratios, the specific energy absorption (SEA) capacity of lightweight structures and, more specifically, of sandwich structures represents a major interest from an impact protection perspective (M. Ashby et al., 2000; Gibson & Ashby, 1999; Kazemahvazi et al., 2012). Several constructive solutions were proposed in order to reach higher SEA performance criteria. In general, the cellular cores of the sandwich structures are the components that count when it comes to impact performance. Whether these cellular structures are made of metallic materials (Cote et al., 2004; Smith et al., 2011; F. Sun et al., 2016), CFRP (Kazemahvazi et al., 2009; Sebaey & Mahdi, 2017; Xiong et al., 2012; G. Zhang et al., 2013) or a combination of several materials (Costas et al., 2016, 2017; G. Zhang et al., 2013) formed into simple (Shin et al., 2008; Yang & Qiao, 2008) or complex shapes (An & Fan, 2016; Fang et al., 2018; G. Sun et al., 2016; Sypeck & Wadley, 2001; Ullah et al., 2016; X. Wang et al., 2015,McKown et al., 2008) it is always a matter of finding the proper type and arrangement of material(s) that offer the highest absorbed impact energy to weight ratio. A consistent review with respect to the SEA performance of thin-walled tubes having different cross sections, filled or not with stochastic foams, is done by Baroutaji A. et al. (Baroutaji et al., 2017). A critical review done by Brathelat F. (Barthelat, 2015) emphasizes the benefits of using the so called architecture materials with respect to impact energy absorption.

Recently, the self-reinforced poly-ethylene terephthalate (SrPET) material (Schneider et al., 2013; J. M. Zhang et al., 2009; J. M. Zhang & Peijs, 2010) has been investigated and used for manufacturing different cellular topologies for sandwich structures (Schneider, Velea, et al., 2015; Velea et al., 2016). Kazemahvazi et al. (Kazemahvazi et al., 2015c) and Schneider et al. (Schneider et al., 2016) proved that these materials pose higher ductility compared to conventional glass and carbon reinforced plastics, which make them appropriate for impact protection applications (Schneider, Kazemahvazi, et al., 2015), apart from the obtained lower life cycle environmental impact (Poulikidou et al., 2015).

An all-PET 2nd order hierarchical sandwich structure has been previously proposed (Velea et al., 2016) based on a simple manufacturing route (i.e. folding of a single sheet of material which has monolithic and sandwich sections distributed in an alternate way), Figure 15, Figure 16, Figure 17. This structure is herein investigated based on a validated FE model, with respect to the specific energy absorption under quasi-static loading conditions, for several geometric configurations. A comparison of the specific energy absorption for the investigated structure is made with the state-of-the-art cellular structures found in the literature.

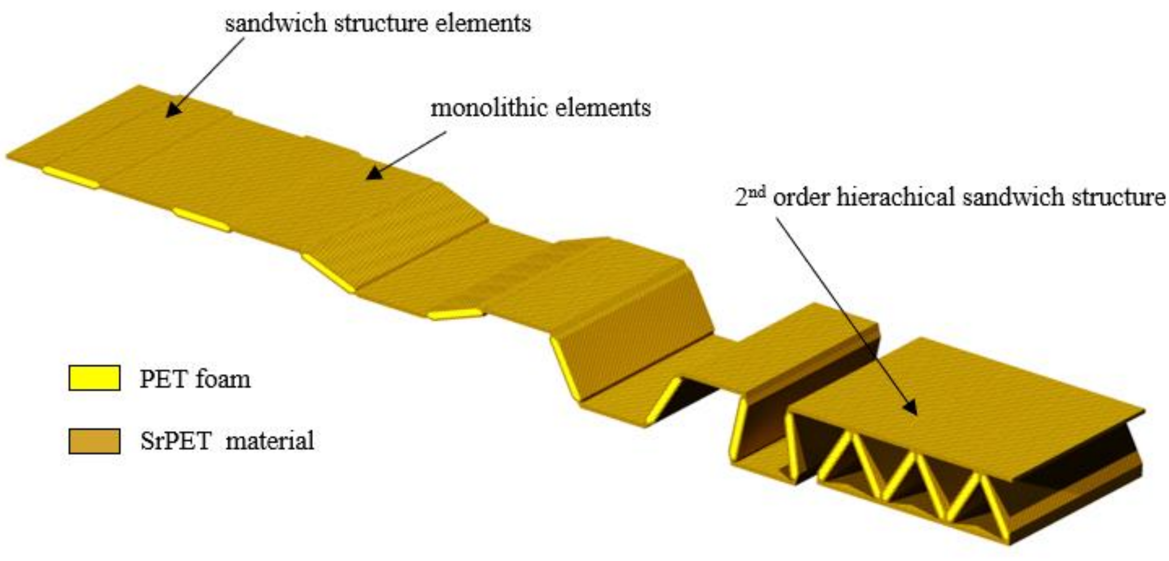

Figure 15 Manufacturing principle of the 2nd order hierarchical sandwich structure

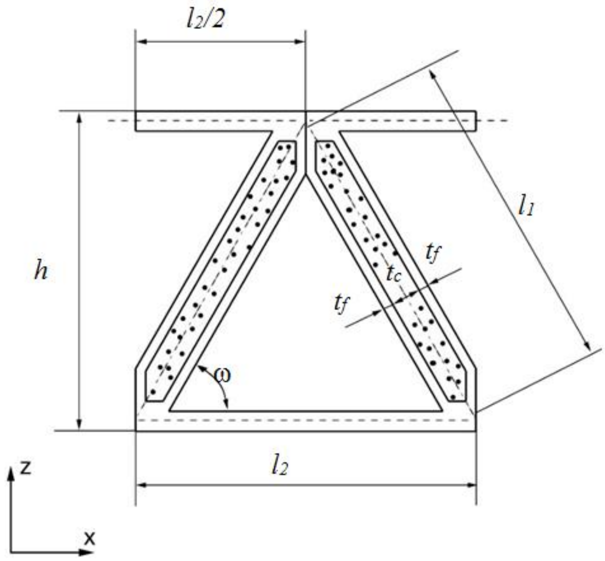

Figure 16 The unit cell of the investigated all-PET 2nd order hierarchical sandwich structure and its geometric parameters [29]. The dotted area represents the PET structural foam. Geometric parameters: l1 – length of the sandwich section, l2 – length of the monolithic section, h – height of the sandwich unit cell, tc – thickness of the PET foam, tf – thickness of the face sheets, ω – folding angle

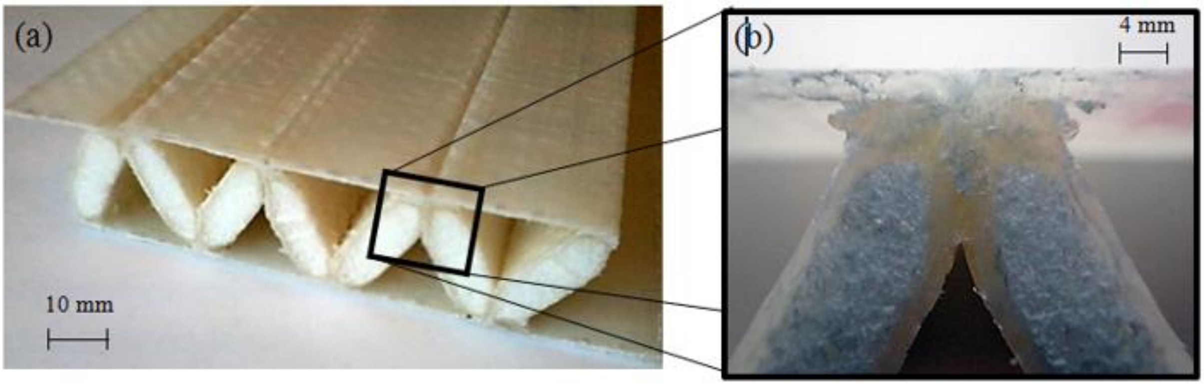

Figure 17 The all-PET 2nd order hierarchical sandwich structure (b) Cross section within the joining area – no additional material is used for the joining procedure; the joint is done by locally melting the PET on the face sheets, pressing and cooling [29].

The numerical investigation is performed based on a validated FE model developed in Abaqus commercial software to extract the force - displacement curve in out-of-plane compression quasi-static loading conditions for 10 geometric configurations (Table 3). Based on these results and by following the resulted deformation modes, an evaluation of the absorbed energy capacity can be performed.

Table 3 The investigated geometric configurations; ω is kept constant at 60°, as well as the width of the specimens, w = 40mm

Configuration	t_f [mm]	t_c [mm]	l_1 [mm]	l_2 [mm]	h [mm]	ρ [kg m−3]
I	0.45	7.1	24	25.8	23.64	232
II	0.9	6.2	25	27.6	25.94	346
III	0.45	7.1	81	80.8	70.99	23
IV	0.9	6.2	82	84.6	75.31	41
V	0.45	4.2	34	34.8	31.16	75
VI	0.9	8.5	35	36.6	33.74	254
VII	0.45	4.2	56	56.8	50.21	29
VIII	0.9	8.5	57	58.6	52.79	105
IX	0.45	4.2	100	96.8	84.85	10
X	0.9	8.5	97	98.6	87.43	39

The layers of SrPET material are modelled as shells while the PET foam is modelled as solid, Figure 18. 8-node linear solid elements, type C3D8R, with reduced integration and hourglass control are used for the discretization of the foam geometry (Figure 19). The shell geometry is meshed with 4-node linear elements, type S4R, also with reduced integration and hourglass control (Figure 19).

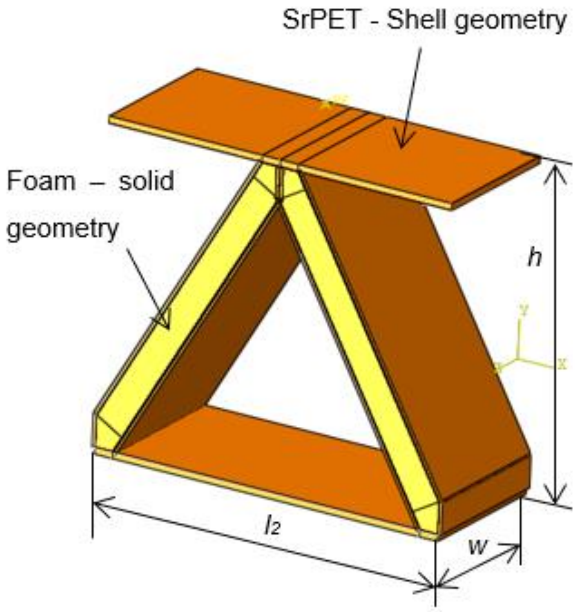

Figure 18 Type of geometry of the components (foamPET and SrPET).

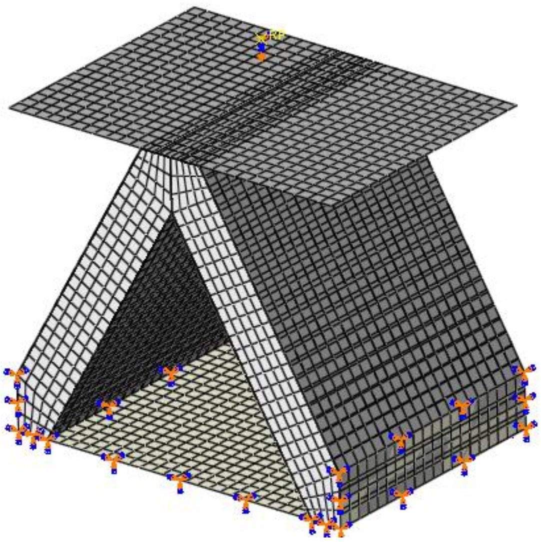

Figure 19 Discretization of the geometry with finite elements

The bottom and side surfaces of the unit cell are constrained, as shown in Figure 20, to avoid the edge effects. An imposed displacement is applied on point A, Figure 20, which is connected by means of a kinematic coupling constraint to the top surface of the structure. Along with the simulation history, the reaction force is recorded on the same point A. The imposed displacement δ is calculated, for each geometric configuration, to obtain $\varepsilon = \delta/h = 0.1$, where h represents the initial height of the structure.

The foam (solid elements) is connected to the SrPET face sheet (shell elements) through a tie constraint, Figure 20. A self-contact is defined by using the surface-to-surface discretization method (Dassault Systemes, n.d.) to avoid penetration of the surfaces during the out of plane compression of the structure (see Figure 20).

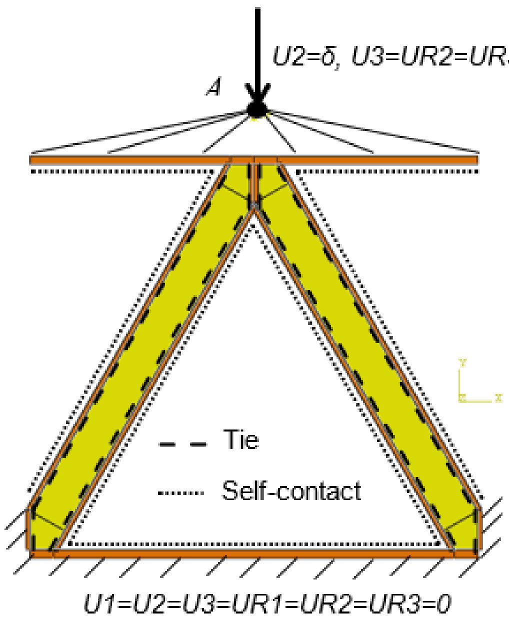

Figure 20 The applied boundary conditions and constraints.

The elastic and plastic material data considered in the numerical model for the SrPET material are shown in Figure 21 and they are established according to the measurements published by Schneider et al. (Schneider et al., 2013) and by Kazemahvazi et al. (Kazemahvazi et al., 2015a).

The data describing the elastic and plastic material behavior for the PET foam material is shown in Figure 22 and it is based on the producer's technical sheet (*Armacell Benelux. ArmaFORM PET/AC Technical Data, Rue de Trois Entities 9-B-4890 Thimister Clermont. <www.Armacell.Com> [Accessed 02.04.2014].*, n.d.), correlated with the experiments carried out by Costas et al. (Costas et al., 2017).

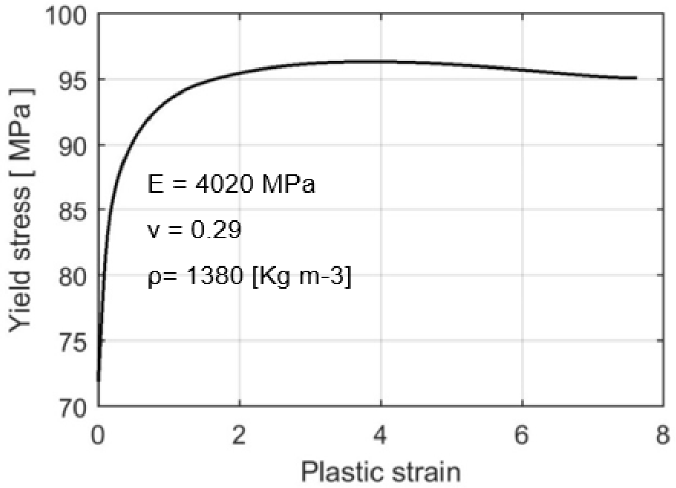

Figure 21 Plastic material behavior of the SrPET material considered within the FE model

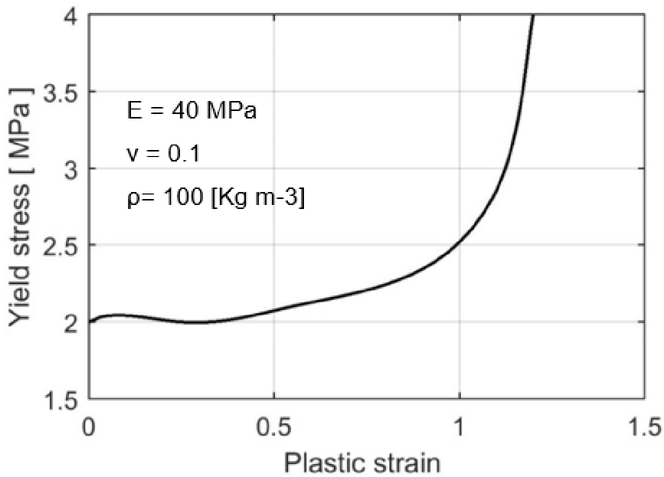

Figure 22 Plastic material behavior of the PET foam considered within the FE model

The developed FE model is validated by comparing the experimentally obtained stress-strain curves for the geometric configurations I, II, III and IV (see Table 3) and the corresponding analytical solution, both obtained by Velea et al. (Velea et al., 2016), with the ones numerically obtained herein, from Figure 23 to Figure 26. Based on the numerically obtained force-displacement curves, the stress σ is obtained by dividing the measured force F to the area of the unit cell ($w \cdot l_2$), while the strain ε is given by the δ / h ratio, where δ represents the imposed displacement and h is the initial height of the unit cell (see Figure 4), similar to Harris J.A. et al. in (Harris et al., 2017).

Figure 23 shows that, for case I, the peak strength is twice compared to the numerical and analytical results, the latter two being very close in value (3% difference). This major difference between the experiments and both the numerical and analytical solutions can be explained by a high sensitivity on the manufacturing method of the specimens (i.e. band saw cutting, at moderate speed, in order not to melt de PET under friction) where the foam suffered at the edges a premature crack at the interface with the SrPET face sheet. In addition, as shown in (Velea et al., 2016), the failure mode for this geometric case was the local buckling which is initiated by the above-mentioned premature crack. However, since both analytical and numerical results are close to each other, it is expected that an ideal manufactured sample will have a similar experimental behavior. In terms of stiffness, a slightly higher value is obtained numerically, as expected. The post-failure region of the numerical model is comparable with the experimental curve.

When looking at case III, Figure 24, the maximum strength is very well predicted by the numerical model compared to the experiments. The analytical solution is a bit higher but still within acceptable limits (1% difference). The numerical estimated stiffness is slightly lower compared to the experiments. The post-failure region of the numerical model fits very well the experimental curve. The failure of the core is initiated by local buckling.

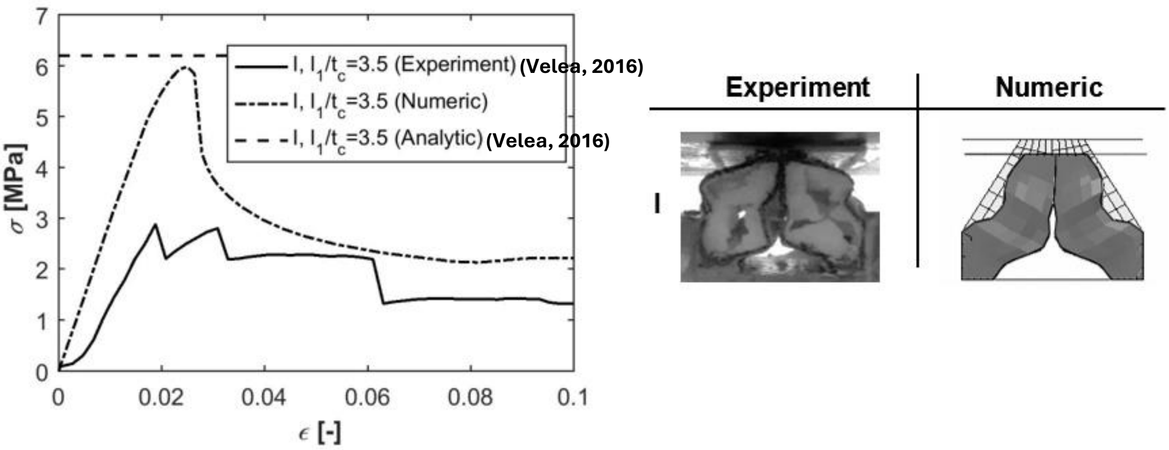

Figure 23 The obtained numerical results compared with the experimental results and analytical calculations for case I (Table 1).

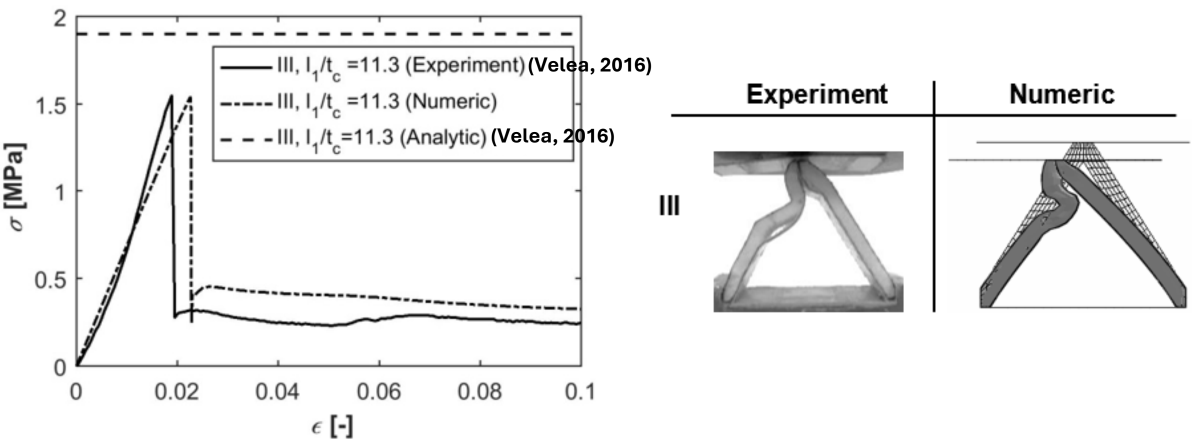

Figure 24 The obtained numerical results compared with the experimental results and analytical calculations for case III (Table 1).

Figure 25 shows that scattered solutions are obtained for case II, for the maximum strength point of view. We certainly have the same influence of the manufacturing method, like case I, that gives a difference of approximately 45% between the experimental and numerical results. However, the difference is not as big as in case I because the thickness of the SrPET material is doubled (0.9 mm instead of 0.45 mm) which increased the stiffness of the strut and therefore being more stable when cutting the specimens. The analytically obtained value is however close to the numerical one (15% difference). The structure fails, in this case, by shear buckling.

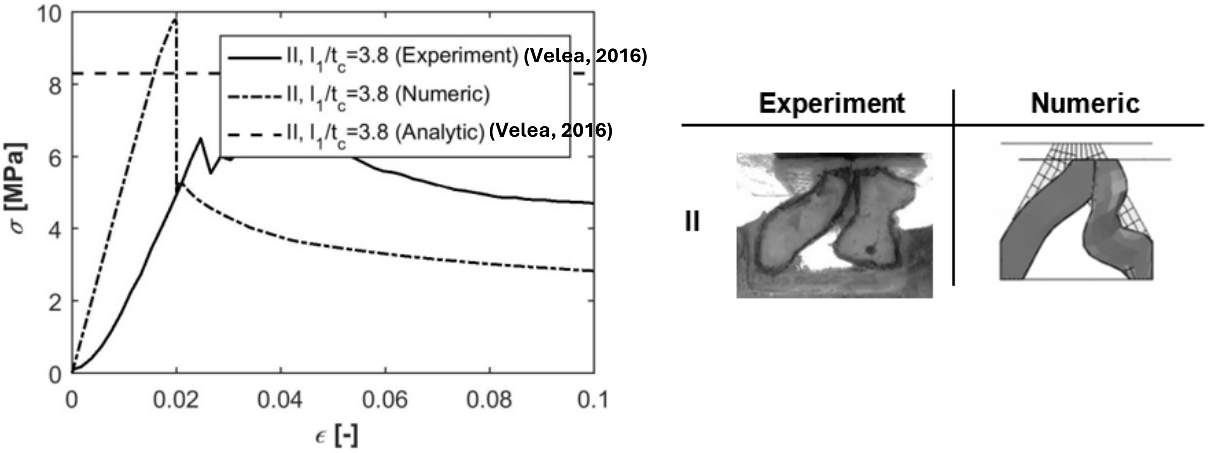

Figure 25 The obtained numerical results compared with the experimental results and analytical calculations for case II (Table 1).

For case IV, Figure 26, there is an almost perfect correlation between the numerical, analytical and experimental results. The observed failure mode is shear buckling followed by general buckling.

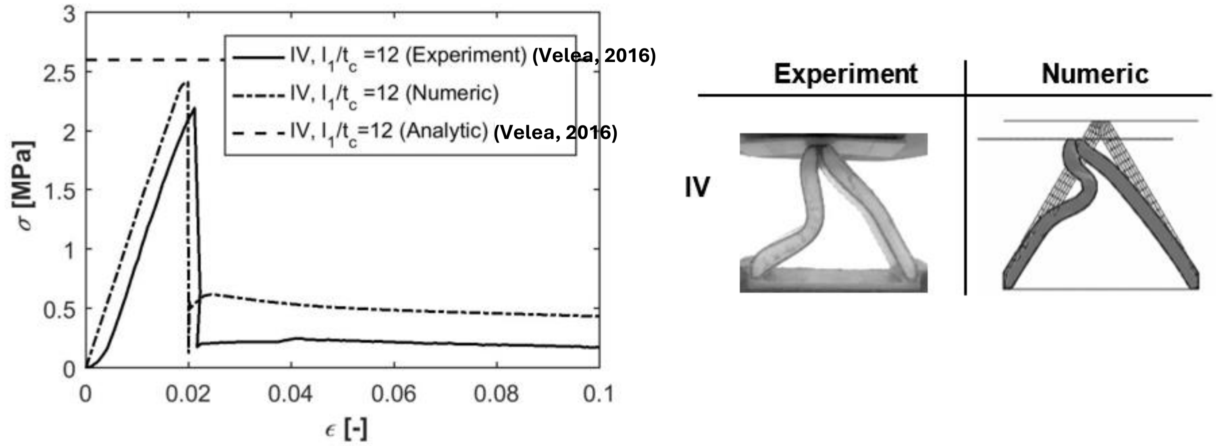

Figure 26 The obtained numerical results compared with the experimental results and analytical calculations for geometric configurations IV (Table 1).

It is therefore concluded that the FE model predicts very well the experimental behavior for case II and IV; these results are also strengthened by the analytical results. Differences exist for cases I and III, at higher l_1/t_c ratios, where the structure is denser and where there is a major influence of the manufacturing method on its experimental assessed behavior.

Based on the validated FE models for geometric cases I, II, III, and IV, additional geometric cases V to X, Table 1, have been investigated in quasi-static loading conditions to extract the force - displacement curve, Figure 27.

By having the force - displacement data, and by taking into consideration the size of the specimens, Table 3, for each investigated case, the Stress - Strain relationship is reached, Figure 28 Strain - Stress curve for the investigated geometric configurations.

The corresponding deformed shapes of the geometric configurations V, VI, VII, VIII, IX and X, at $\varepsilon = 0.1$ are shown in Figure 29 The deformed shapes of the structures (V to X) for $\varepsilon = 0.1$.

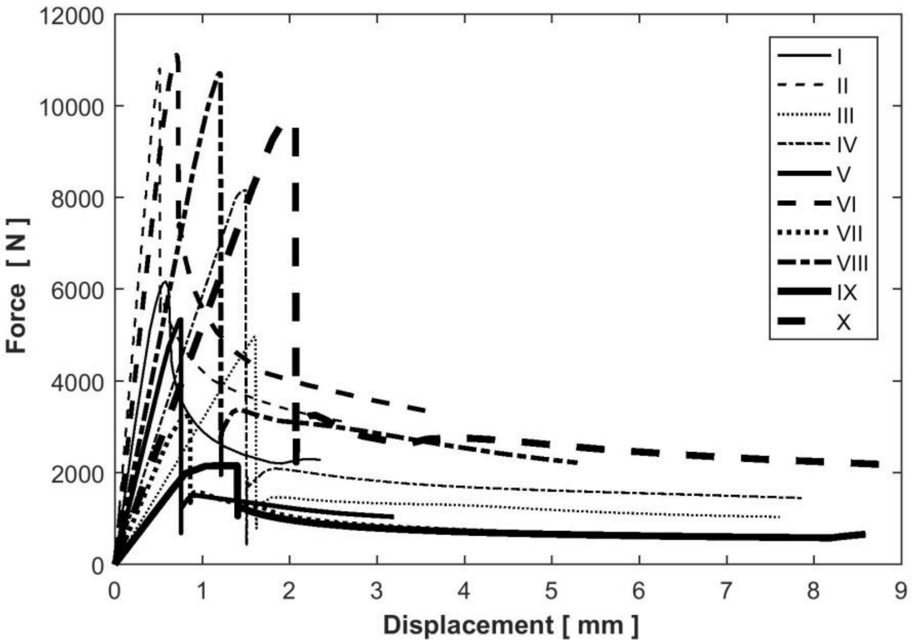

Figure 27 Force - Displacement curve for the investigated geometric configurations.

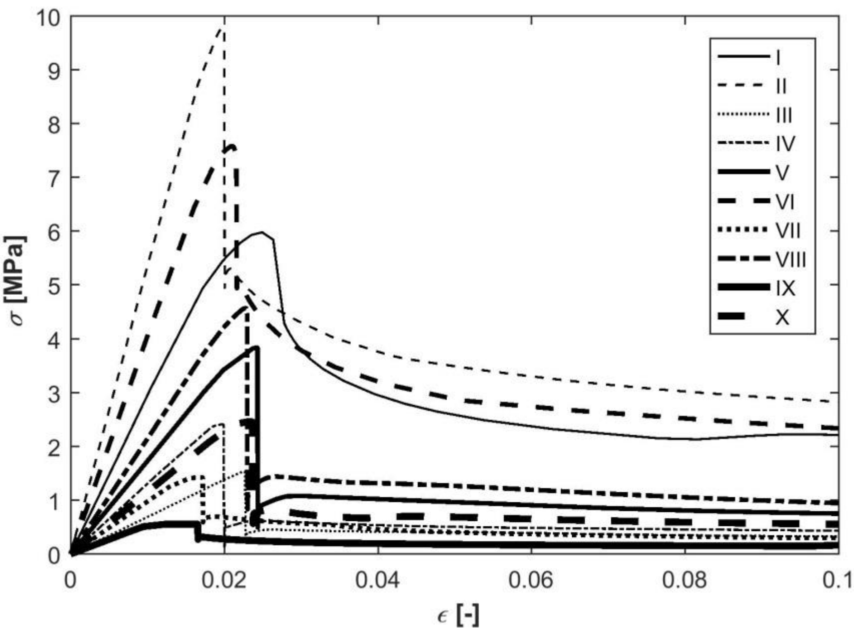

Figure 28 Strain - Stress curve for the investigated geometric configurations.

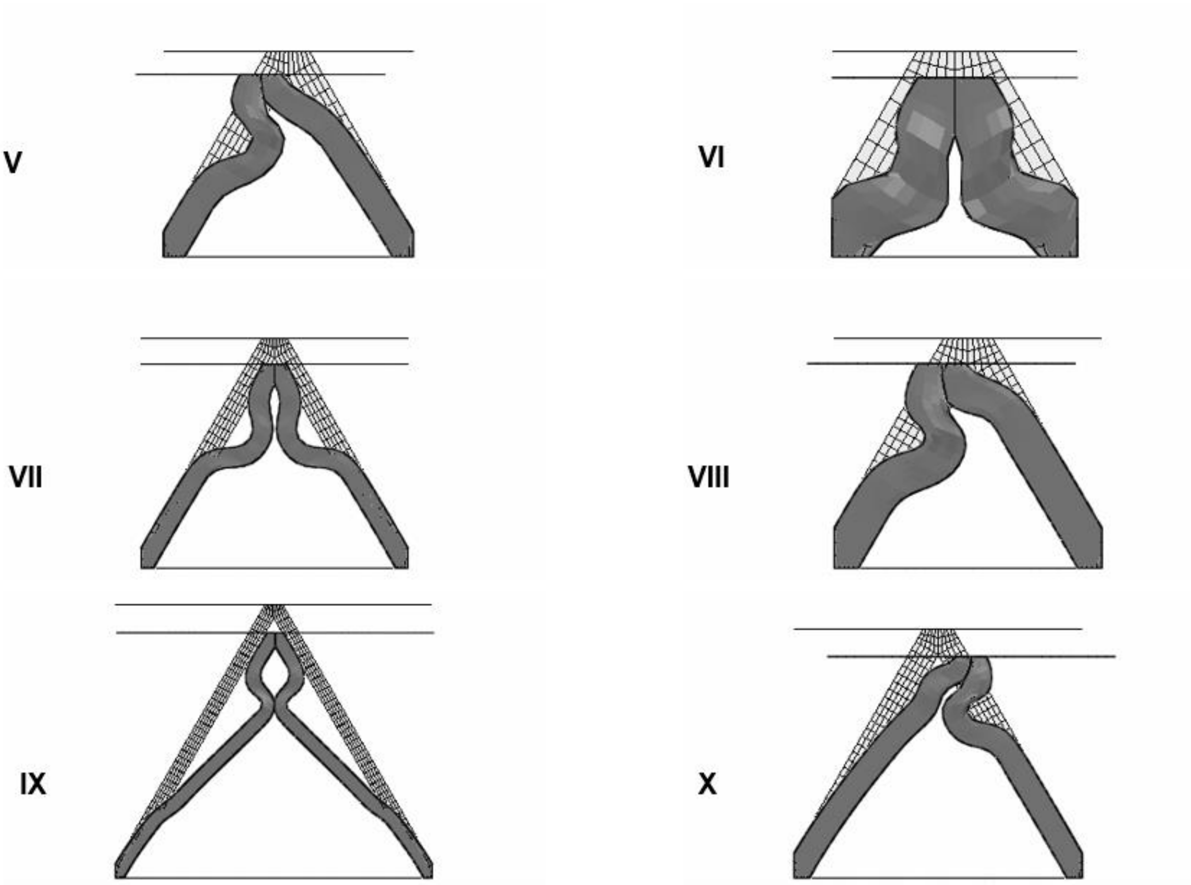

Figure 29 The deformed shapes of the structures (V to X) for ε = 0.1.

Several quantitative criteria exist for the evaluation of the energy absorption capacity (Gibson & Ashby, 1999; Nagel, n.d.). One of the most used refers to the determination of the specific energy absorption capacity E_m [KJ/Kg], which is the absorbed energy per unit mass. Thus, the specific energy absorption capacity of a structure is calculated as the ratio between the absorbed energy E_{abs} and its mass m, equation (13).

$$E_m = SEA = \frac{E_{abs}}{m}, \quad (13)$$

where,

$$E_{abs} = \int_0^{\delta_{max}} F(\delta)\, d\delta, \tag{14}$$

with: m – mass of the structure; F – measured force; δ – crushing distance

It is known that higher values for the reaction forces are obtained at higher strain rates when compared to a quasi-static loading (S. Lee & Espinosa, 2005; Tancogne-Dejean et al., 2016; Xiao & Song, 2018), meaning that higher SEA capacity results as the strain rate is increasing. Therefore, the current SEA estimation, based on quasi-static loading conditions, allows obtaining the lower boundary for the energy absorption capacity.

The energy absorption E_{abs} and the corresponding specific energy absorption E_m are calculated herein for ε = 0.1. This condition results from the need of a comparison base between the investigated geometric cases (see Figure 27, where the compression depth differs from one geometric case to the other) and the other types of cellular structures from the technical literature. Figure 30 shows that, for the investigated hierarchical sandwich structure, the specific energy absorption E_m increases while the l_1/ t_c ratio decreases. For the same t_c/ t_f ratio, the specific energy absorption E_m increases twice for the case I (232 kg m−3) compared to the case III (23 kg m−3). The same behavior is similar for case II (346 kg m−3) compared to case IV (41 kg m−3), which indicates, as expected, an increase of the E_m values with the density. The value of the E_m doubles while the density of the structure is ten times increased. Another observation is that the E_m is increasing by 20% while doubling the thickness t_f of the face sheets.

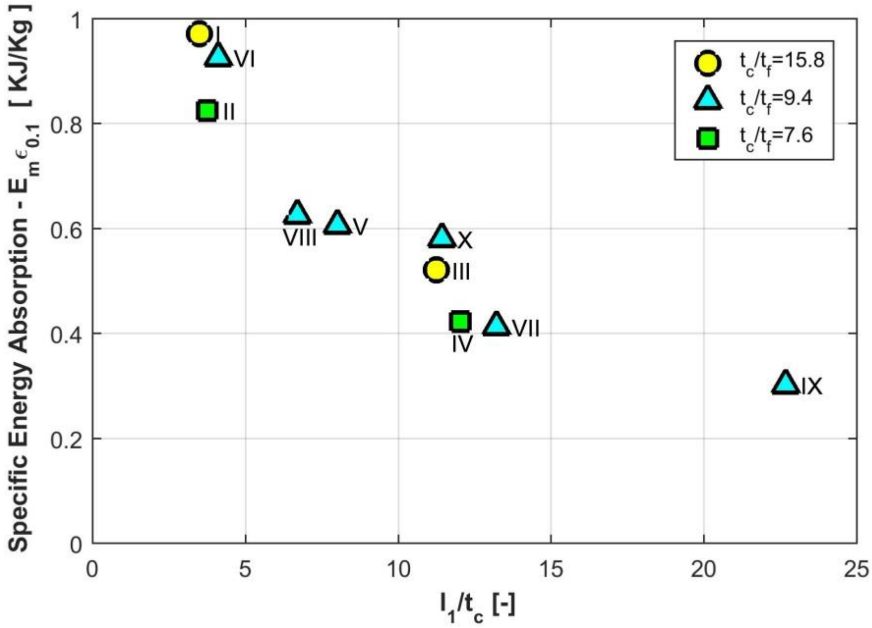

Figure 30 The resulted E_m in terms of the geometric parameters of the investigated structure

Figure 31 shows a comparison of the specific energy absorption E_m obtained for the investigated structure with the one of different types of structures found in the literature (Figure 32), in terms of structures' density. For the same specific energy absorption (approx. 1 KJ/Kg), the density of the all-PET 2nd order hierarchical sandwich structure is five times lower compared to the one of the lattice structures made by steel through additive manufacturing (McKown et al., 2008) and seven times lower when compared to the micro-trusses made from Nichrome alloy (Sypeck & Wadley, 2001). It can also be observed that, for the same density value (~40 kg m−3), the all-PET 2nd order hierarchical sandwich structure can reach a three times higher specific energy absorption capacity compared to the lattice structures made from CFRP (Sebaey & Mahdi, 2017). However, a better behavior at the same weight is observed for a hybrid structure that contains Aluminum, PET foam and GFRP reinforcements [11] and for a type of pyramidal structure made from CFRP (G. Zhang et al., 2013).

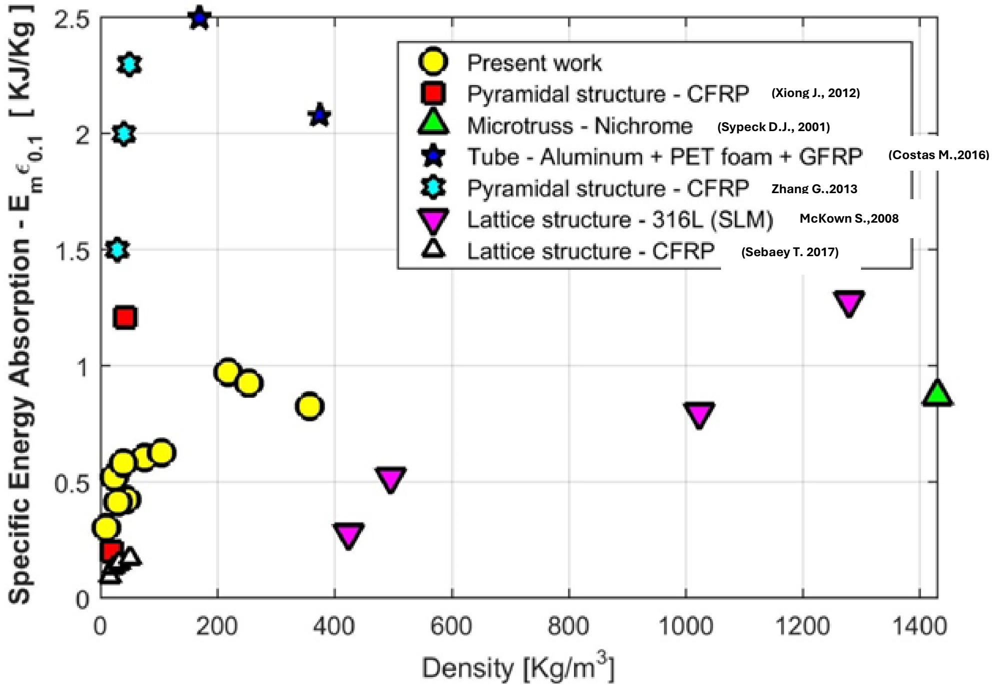

Figure 31 Comparison of the specific energy absorption E_m for different proposed cellular structures for ε = 0.1

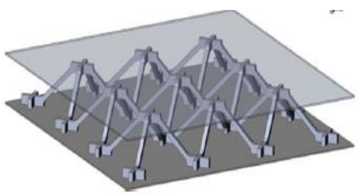

(Zhang G., 2013)

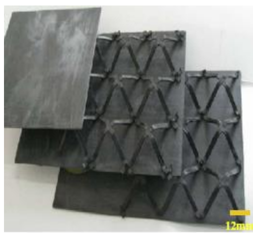

(Xiong J., 2012)

(Costas M., 2016)

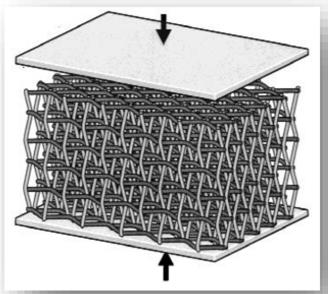

(Sypeck D.J., 2001)

(McKown S., 2008)

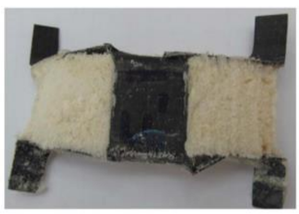

(Sebaey T., 2017)

Figure 32 Types of cellular structures used for comparison of the impact performance

The investigated all-PET 2nd order hierarchical sandwich structure proves to be a competitive constructive solution with respect to energy absorption capacity when compared to other existing cellular configurations which are made through more complicated manufacturing routes. The herein proved characteristics come both from the ductile behavior of the SrPET material, combined with the PET foam, and from the geometric arrangement of the investigated cellular structure. This competitive behavior represents an added value for the investigated 2nd order hierarchical sandwich structure in addition to the already proved advantages, such as mechanical performance in out-of-plane compression and a lower life cycle environmental impact through a high degree of recyclability.

2 Hybrid structures

2.1 Description of the topic

Hybrid materials or arhitectured materials as they are defined by prof. Ashby (M. F. Ashby, 2013; M. F. Ashby & Bréchet, 2003) are obtained through "combinations of two or more materials or of materials and space, configured in such a way as to have attributes not offered by any one material alone". In other words, hybrid materials are obtained "by combining two or more monolithic materials in chosen configurations and connectivity", (M. Ashby, 2011). While for composite materials and structures the concept of hybridization is done at a microstructure level, within the hybrid materials and structures the hybridization is done at the macrostructure level.

2.2 Achievements

I. Study case: Connecting rod for the anti-roll bar made of CFRP combined with steel (Velea M.N., 2020)

The main purpose of this work was to evaluate the possibility of using thermoplastic composite materials (LPET reinforced with carbon fiber) for structural a component from the suspension system of a vehicle – i.e. connecting rod ( ). A hybrid structure therefore results by replacing a portion of steel in the connecting rod of the antiroll bar with the carbon fiber reinforced LPET, to achieve lower weight while meeting the performance requirements of the original component.

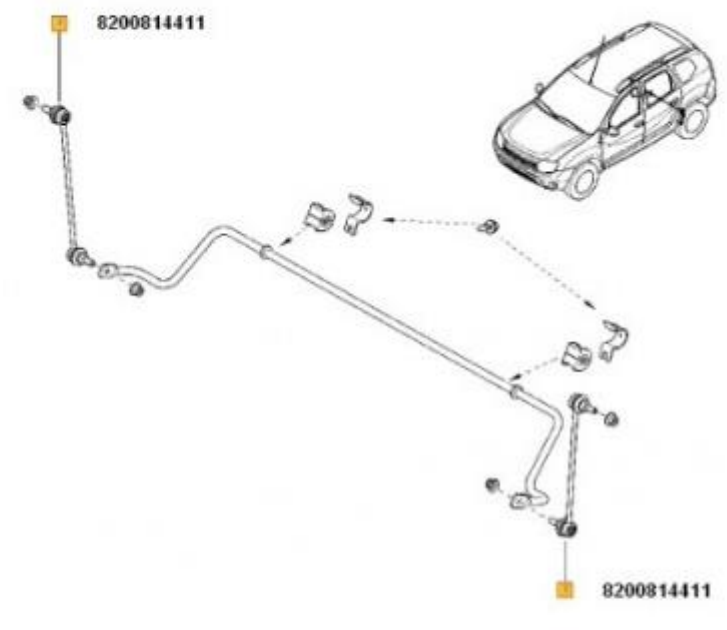

Figure 33 Anti-roll connecting rod

For the construction of the hybrid connecting rod, a 195 mm section was cut from the steel central rod (Figure 34) and replaced with an aluminum tube of the same diameter as the steel rod (Figure 35 and Figure 36). The role of the thin aluminum tube is to provide support for rolling the C/LPET fabric

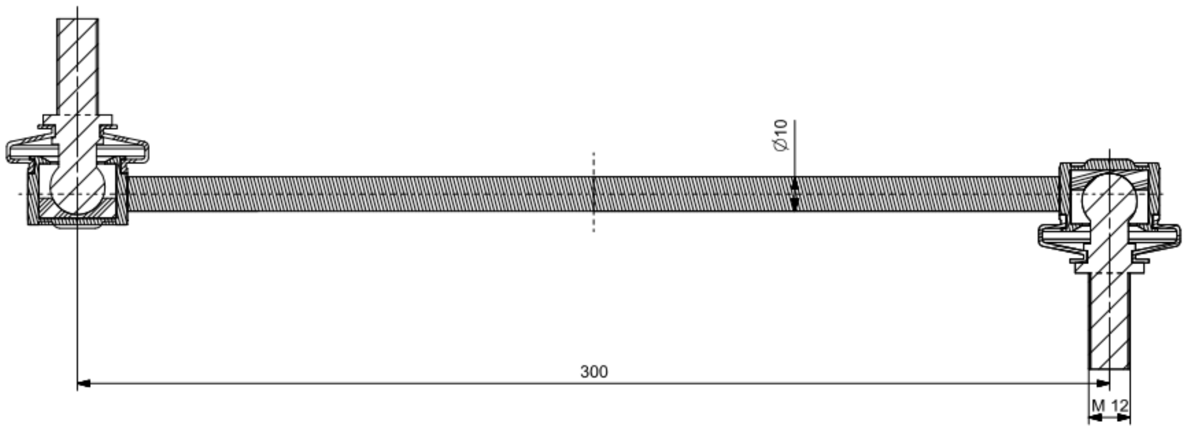

Figure 34 Connecting rod – original concept

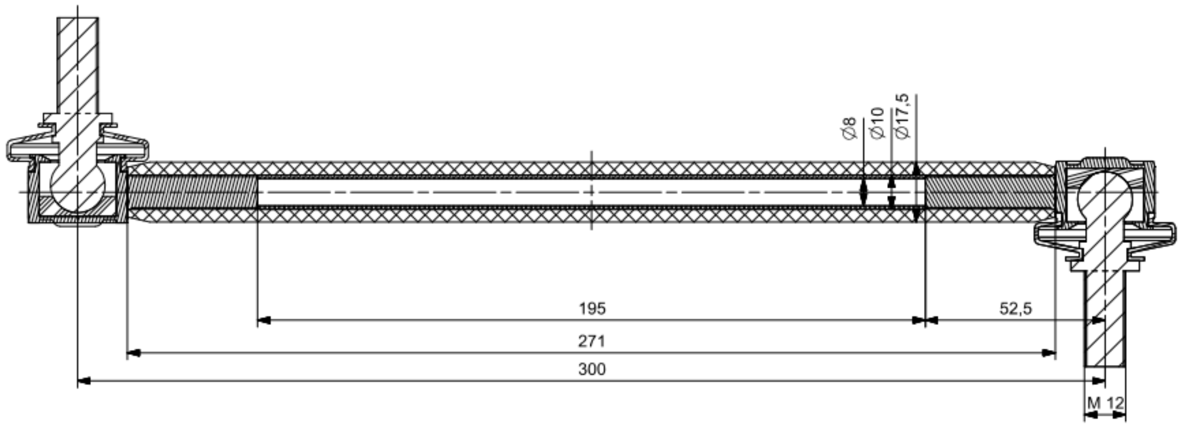

Figure 35 Connecting rod – hybrid structure concept

(a) Steel components

(b) Thin aluminum tube

(c) C/LPET weave wrapped around the steel end and aluminum tube

Figure 36 Elements of the hybrid connection rod - grooves were made on the ends of the connecting rod to increase the connection strength between the steel and the C/LPET

Figure 37 Rolling the C/LPET weave

After the C/LPET weave was rolled, Figure 37, the connecting rod was wrapped with non-stick foil and with heat shrink tape, to keep it together, Figure 38.

Figure 38 The CPET weave is covered with heat shrink tape

The created assembly was placed in the oven, and the consolidation process took place for 180 minutes, at a temperature of 200°C. During the entire process, a vacuum pump was used to create negative pressure in the vacuum bag (Figure 39 and Figure 40). The LPET melts and washes the carbon fiber at the same time while connecting the steel ends. No adhesive was used for joining the elements. The LPET provides also a surface finish for the component (Figure 41).

Figure 39 Hybrid connecting rod in the vacuum bag prepared for the thermal consolidation process

Figure 40 Hybrid connecting rod in the oven, at the end of the consolidation process

Figure 41 The resulted hybrid connecting rod

A Zwick testing machine was used for compression testing of both connecting rods (original and hybrid one), Figure 42. An imposed force of 5000N was applied while measuring the resulted displacement. At 5000N, an elongation of 0.8 mm resulted in the case of the steel rod while a slightly higher elongation is observed for the hybrid connecting rod (approx. 1.3 mm).

(a) Steel connecting rod

(b) Hybrid connecting rod

Results:

	Legends	Nr	Pull out force N
Bieletă oțel		1	5005
Bieltă hibridă		2	5001

Series graph:

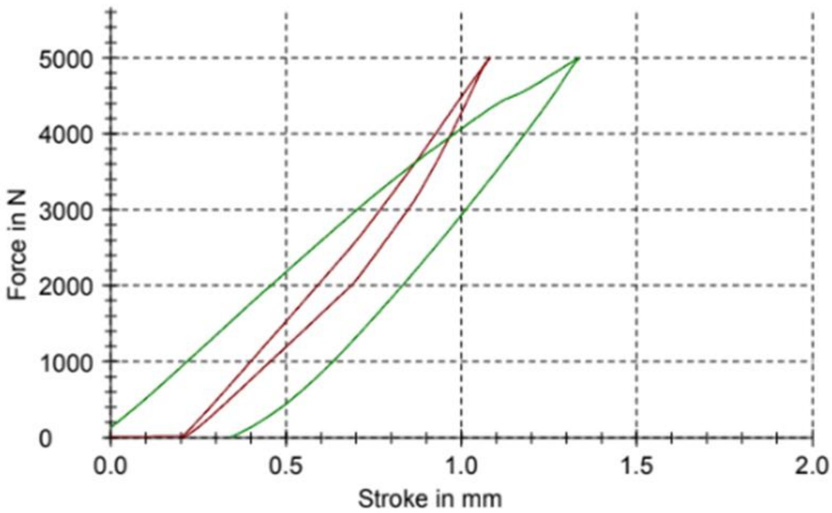

Figure 42 Comparative results between the original and the hybrid connecting rod

However, a permanent deformation of 0.35 mm was observed for the hybrid connection rod without any visible cracks (Figure 42). This hysteresis like behavior could be an advantage in a dynamic loading regime. The hybrid concept for the connection rod provides a mass reduction of 16,6%.

II. Study case: Ball screw drive with CFRP shaft and steel nut (D. G. Dima et al., 2016)

Figure 43 represents an extract from the patent number DE102017114852A1 and RO132354A2, coauthored by Velea M.N. This invention relates to a ball screw drive, comprising a threaded spindle (1) and a threaded nut (2) which is rotatably mounted on the threaded spindle (1) via balls (4) guided in a ball channel (3), wherein the threaded spindle (1) has a shaft (5) and a helical spring (6) wound around the shaft (5) in a helical manner, which engages in a recess (7) wound around the shaft in the outer peripheral surface of the shaft (5), and wherein the helical spring (6) delimits the ball channel (3) for partially receiving and guiding the balls (4) on the threaded spindle (1).

According to the invention, the shaft (5) is made of a fiber-plastic composite material, wherein the recess (7) is formed by the heat effect of the helical spring (6) in the outer peripheral surface of the shaft (5). Furthermore, the invention also relates to a method for producing the ball screw drive. (Dima et al., n.d.)

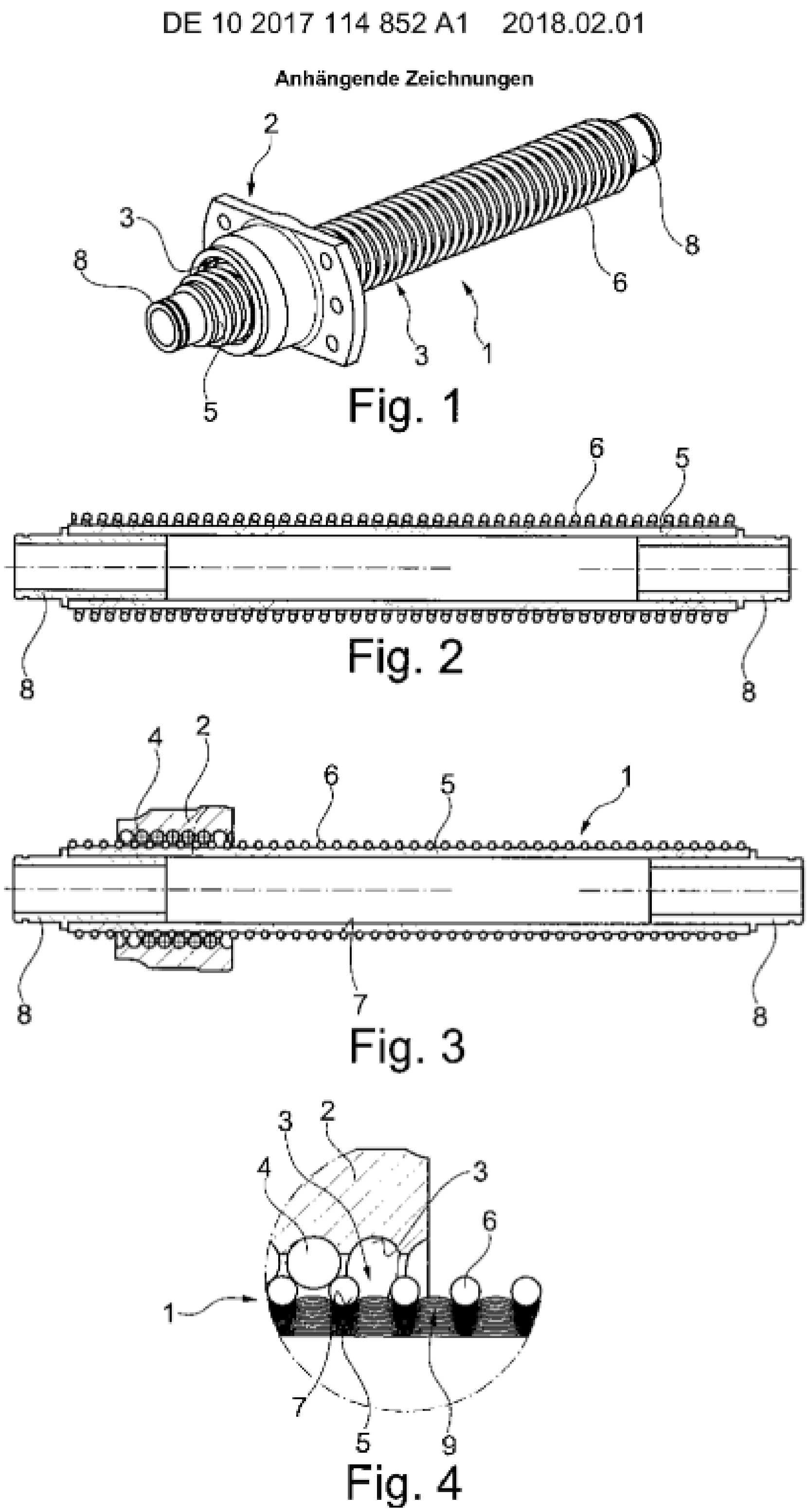

Figure 43 Ball screw drive – the shaft represents a hybrid structure made out of metal (rolling path) and fiber reinforced plastics (the body of the shaft) (D. G. Dima et al., 2016)

III. *Study case: Hybrid wheel flange and method for producing the wheel flange (D. Dima & Velea, 2016)*

Figure 44 represents an extract from the patent number DE102016205493A1, coauthored by Velea M.N. The invention relates to a wheel flange (20) for wheel bearing arrangements comprising a thin-walled base body (30) made of sheet metal, wherein the base body (30) has a first central opening into which a first metal insert (40) is inserted and has further openings arranged around the central opening into which further metal inserts (50, 60, 70, 80) are inserted, wherein a fiber composite material (60) is guided starting from the first metal insert (40) around one of the further metal inserts (50, 60, 70, 80) and from the one of the further metal inserts (50, 60, 70, 80) back to the first metal insert (40), wherein the fiber composite material (60) is guided starting from the first metal insert (40) around all the further metal inserts (50, 60, 70, 80) accordingly.

DE 10 2016 205 493 A1 2017.10.05

Anhängende Zeichnungen

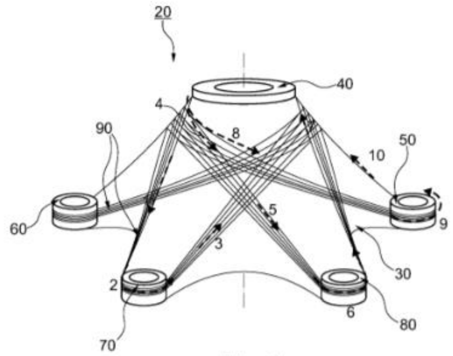

Fig. 1

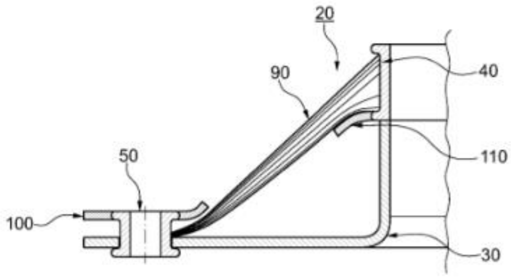

Fig. 2

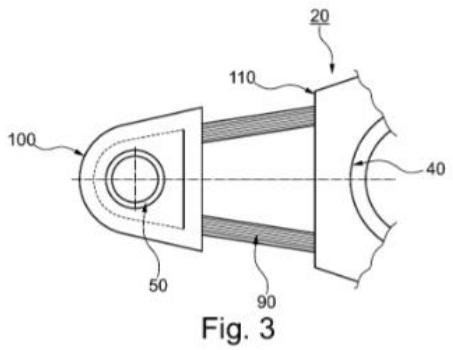

Fig. 3

Figure 44 Flange – a hybrid structure made from metallic parts (inserts) and unidirectional fiber reinforced plastic that carries the load (D. Dima & Velea, 2016)

3 Optimization of mechanical systems / structures

3.1 Description of the topic

In various branches of engineering, the general design process of a system/product can be described in stages according to the scheme in Figure 45.

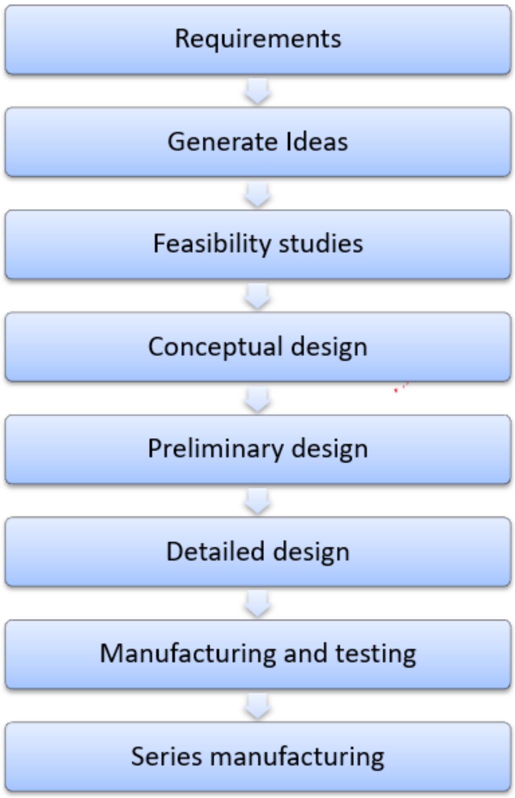

Figure 45 The overall design process of a system / product

Starting from the identification of a problem, the design team goes through several steps to develop the system/product that meets the specifications defined in advance. The ideas generated in brainstorming sessions are subjected to a feasibility study after which the concepts with the potential to meet the imposed criteria are selected. The selected concepts are then ordered in a ranking based on a multi-criteria analysis. Up to this point, we work with simplified schemes that describe the logic of the system's operation, most of the time these are represented by hand sketches. For the first concepts in the ranking, the design stage follows, which, most of the time, is divided into:

- conceptual design, where the operating principle is validated, for example by carrying out energy balance analyzes of the system; the fulfillment of the desired functionalities is verified using simple specific technical calculations;
- the preliminary design, where the system components are assigned a preliminary geometry, the necessary elements for the connection with other systems are taken into account, if necessary, the type of material is chosen for each individual component, etc.;
- detailed design, where it is considered, for example, the integration into the system of all components or subassemblies, the development of the manufacturing process, the finalization of the specifications for the manufacturing conditions, etc.

In the manufacturing stage, the prototype of the developed system is made in the first phase. Depending on the results of the tests carried out on this prototype, it moves to the next stage – series manufacturing, or it returns to one of the previous stages to correct any design mistakes.

In a traditional design process, the evaluation of the degree of fulfillment of the performance criteria is carried out based on a model of the system, usually developed in the conceptual or preliminary design stage. Analyzing this model allows understanding and quantifying the behavior of the system. If the performance resulting from the analysis of the model is not satisfactory, then it is returned to the concept and/or to the model to adjust the parameters that influence the behavior of the system. Figure 46 describes this iterative process whose success depends largely on the experience of the specialist who models and analyzes the system.

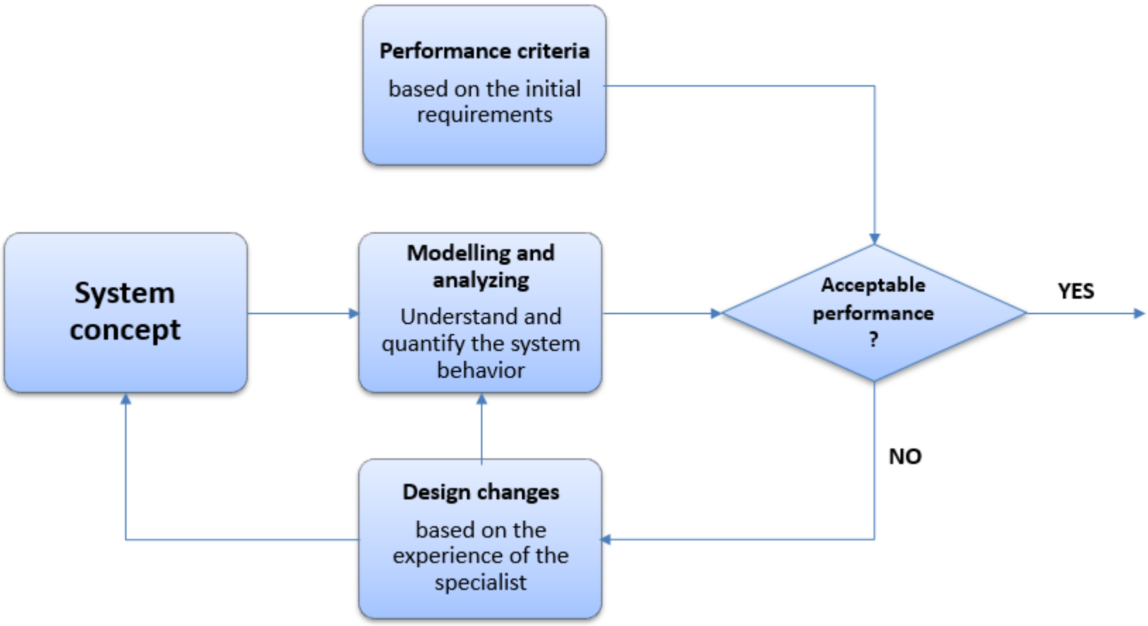

Figure 46 The traditional design process

An optimal design process involves the automation of the search stage for the values of the parameters that influence the behavior of the analyzed system with the aim of reaching the imposed performance criteria (Figure 47). Thus, optimal design involves defining an optimization problem based on a model of the system and analyzing it based on an algorithm for finding the optimal solution / solutions (optimization algorithm). It is important to note, in Figure 47, that the optimization algorithms can act on the parameters that define the system model but not on the system concept, this remains the task of the design engineer.

In relation to Figure 4, within an optimal design process, the conceptual, preliminary or detailed design stages involve the use of two types of models of the designed system: a model describing the behavior of the system (used for its analysis) and a model for formulating optimization problem (used to search for the optimal solution).

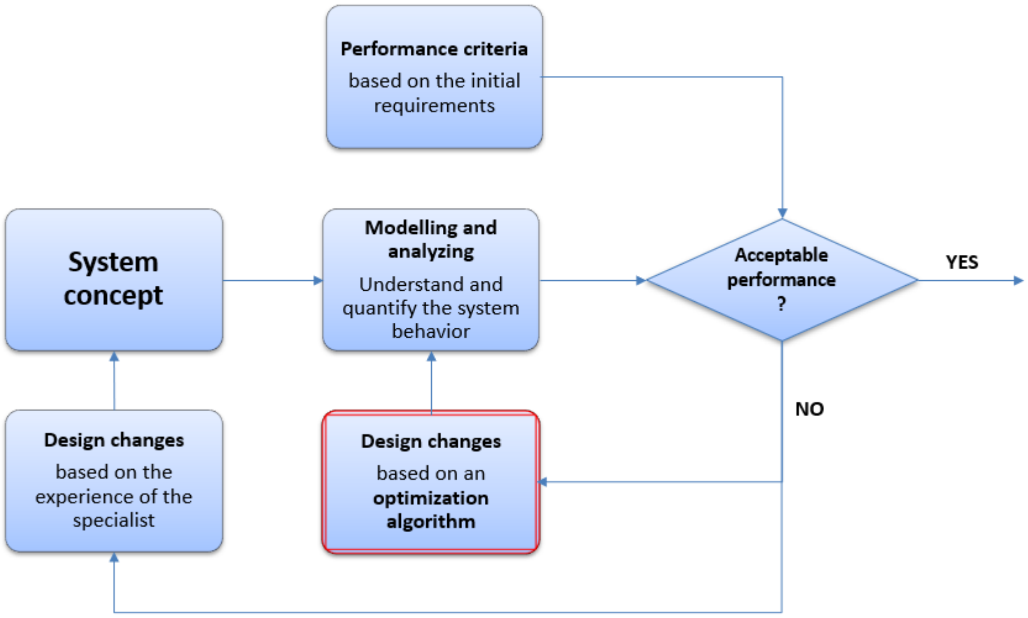

Figure 47 The optimal design process

In relation to Figure 48,, within an optimal design process, the conceptual, preliminary or detailed design stages involve the use of two types of models of the designed system: a model describing the behavior of the system (used for its analysis) and a model for formulating optimization problem (used to search for the optimal solution).

The model for optimization must be coherent with the model that describes the behavior of the system, so that the objective functions pursued in the optimization process are found as outputs in the behavioral model (the model for analysis). Also, if the analyzed system presents a non-linear behavior, then the optimization problem must be formulated so that a non-linear optimization algorithm can be used to solve it.

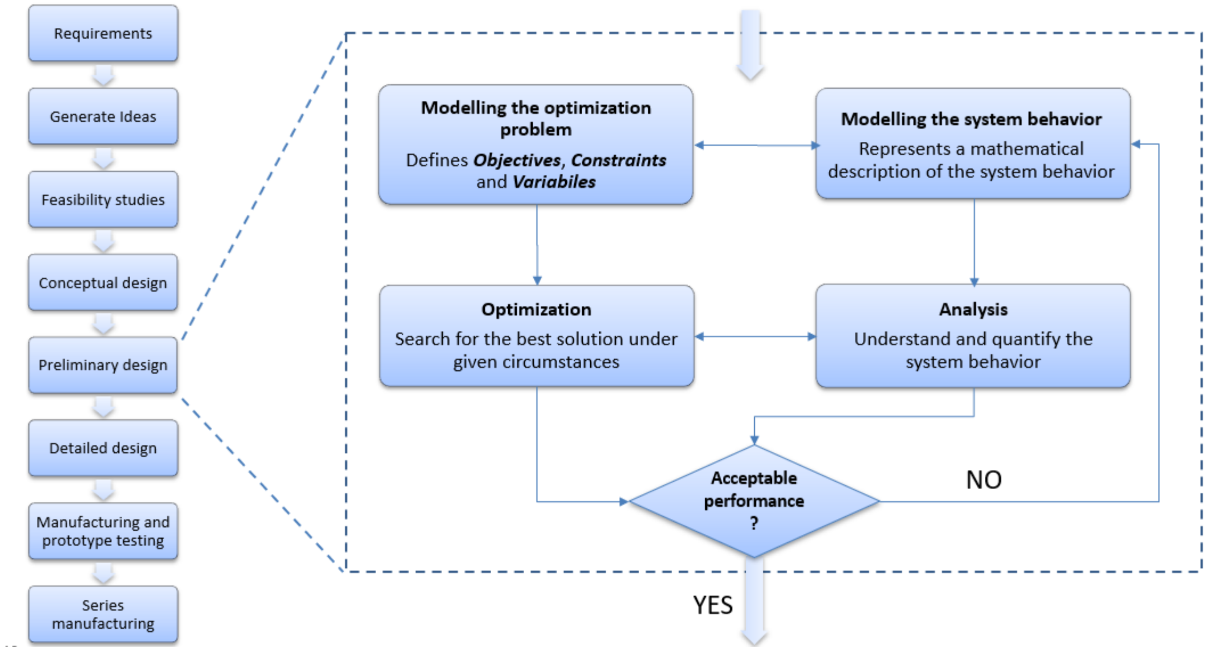

Figure 48 Interdependence of Design, Modeling, Analysis and Optimization

A system is a collection of components that interact to perform one or more functions (Figure 49). *x* represents the state variables of the system; they represent system state or memory. Initial states $x(t_0)$ and inputs $i(t)$ determine outputs $o(t)$ and state $x(t)$, where $t > t_0$.

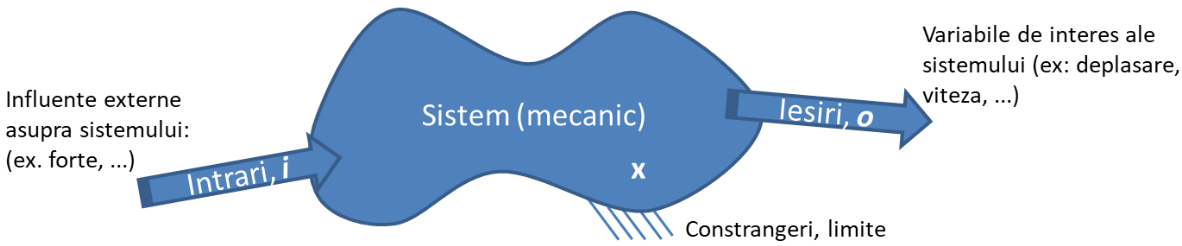

Figure 49

The model of a system is a description of the real system; it must capture the essential information about the system (depending on the purpose pursued). Modeling is the development of an approximate, simplified representation of a system.

So, the behavioral model of the system is usually a mathematical, analytical or numerical model, which is used to analyze the system in order to understand and quantify the behavior / physics of the system. They can also be used for the behavioral description of systems and meta-models or models based on Fuzzy logic.

Regardless of the type of model used, each system must be modeled at a particular level of detail that corresponds to the interests of the one studying the behavior of the system (Papalambros & Wilde, 1988). Thus, if we consider the general case of the transmission system of a motor vehicle, Figure 50, several levels of detail can be identified at which the desired model can be developed. Level 1 would involve modeling the transmission system as a single block with appropriate input and output quantities (e.g. chemical energy – fuel – input and mechanical energy output). Level 2 involves modeling the subsystems found in the transmission assembly. For example, one model / block with specific inputs and outputs for each of the engine, gearbox and clutch subsystems was considered. Level 3 corresponds to sub-sub systems modeling. For example, the engine subsystem is broken down into sub-subsystems or components, in the case of the engine it could be, for example, the crankshaft, connecting rod, etc. And so on, the decomposition continues down to a basic level, for example down to the material characteristics of each component or the heat treatment applied to the components in question (Level 5 in Figure 50).

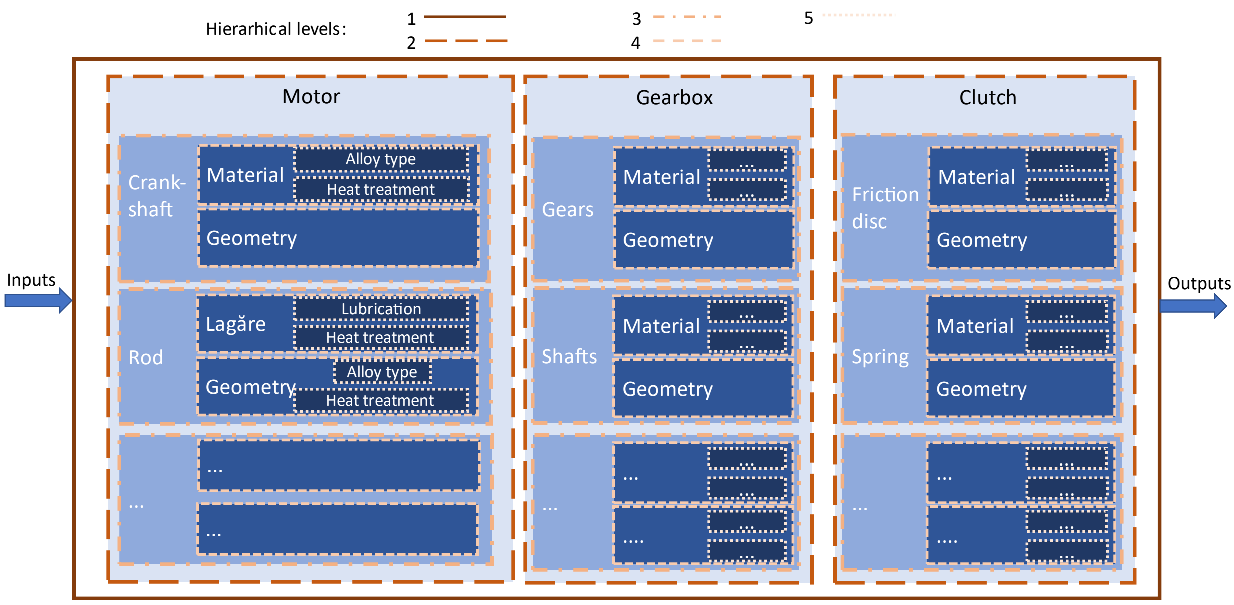

Figure 50 Transmission system of a motor vehicle broken down into different hierarchical levels

The classification presented on hierarchical levels is intended to exemplify the way of ranking according to the level of detail. Each block in Figure 7, regardless of the hierarchical level at which it is found, can be interpreted as a self-contained system and modeled as such, with specific input and output quantities, based on which the analyzes of interest can be developed. By solving the mathematical model of a system, its simulation and analysis is carried out.

The analysis of the system involves the use of its behavioral model for checking and evaluating the responses of interest (of the output quantities) under certain operating conditions (for certain values of the input quantities). In other words, system analysis means solving the mathematical model (analytical or numerical) of a system. The results of the system analysis basically represent the dependence of the input quantities of the system on its output quantities. The results obtained from the analysis, before any other interpretation, must be validated with the reference system. The validation of the theoretical model with the experimental system can be done in several stages, as shown in Figure 8. First, the existence of the same functions of interest (functional role) must be validated. After that, the conceptual validation can be done based on the input quantities of the system (representation details). Finally, the behavioral validation is done, i.e. the comparison of the output quantities (of the functions of interest).

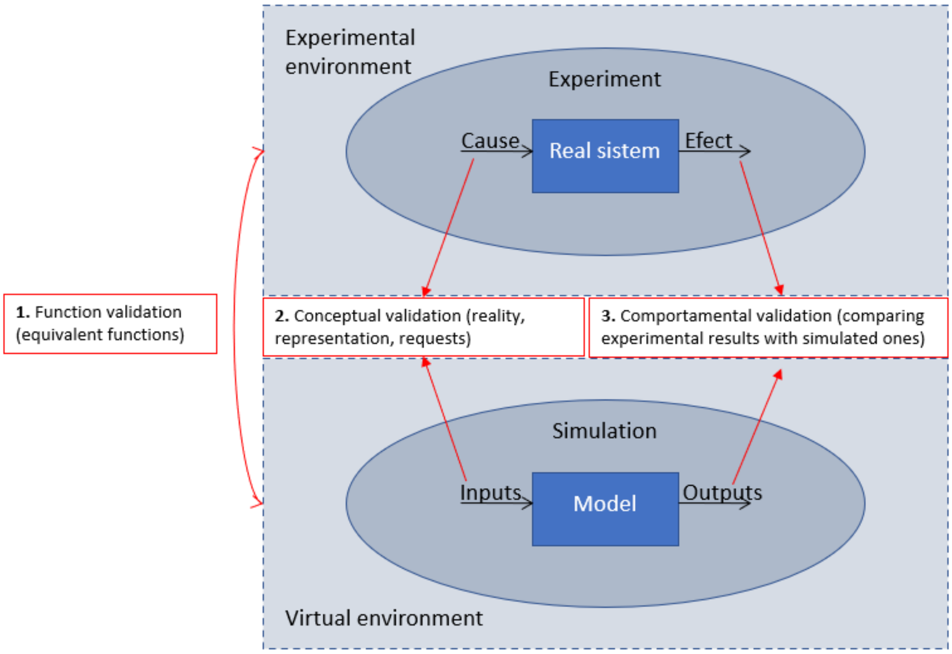

Figure 51 Steps in validating mathematical models with real systems

The model used in the optimization process may be the same as the behavioral model or may be derived from it, depending on the type of problem being studied. In any case, the model of the optimization problem must be validated with the behavioral model, as shown in Figure 48.

Formulating the optimization problem involves identifying the design variables (input quantities) and defining their lower and upper bounds, establishing the objective function or functions, and defining constraints, if applicable.

The general form, expressed mathematically, of an optimization problem is of the form:

$$\begin{gathered} min\, f(x) \\ g(x) \leq 0 \\ h(x) = 0 \\ \underline{x} \leq x \leq \overline{x} \end{gathered} \tag{15}$$

unde:

- *f(x)* represents the objective function
- *g(x)* represents the vector of inequality constraints
- *h(x)* represents the vector of equality constraints
- *x* represents the vector of design variables (independent variables)
- the limits applied to the design variables x are also constraints

Examples of objective functions:

- minimizes the weight of a system

- maximizes the rigidity of a system

- minimizes the size of a system

- maximizes the number of cyclic stresses that a given component can withstand

- maximizes the efficiency of a system

- minimizes the energy consumption of a system

- minimizes polluting emissions

- minimizes the cost of a system, etc.

Of course, these objective functions should be represented as mathematical functions, depending on the type of model used.

The quantities that are used to define equality or inequality constraints are of three kinds:

- parameters

    - are quantities that remain constant throughout the optimization process
- independent variables
    - their values do not depend on the values of other variables
- dependent variables
    - their values from the values of other variables
    - the number of dependent variables is usually equal to the number of equality constraints

A set of independent design variables x (input quantities) that satisfies all applied constraints is called a feasible solution (even if it does not minimize/maximize the objective function). The optimal solution, if it exists, is found in the set of solutions that satisfy all the constraints considered.

Optimization is the process of maximizing and/or minimizing one or more objectives, without violating the imposed constraints, by adjusting a set of variable parameters (input quantities) that influence both the objectives (output quantities) and the constraints.

In other words, regarding the field of mechanical engineering, optimization refers to the application of mathematical reasoning by which the optimal values of the parameters that characterize a component or a set of components in a mechanical system are determined, values that correspond to the maximum/minimum points of response functions corresponding to the analyzed system.

Figure 9 shows the general steps taken to solve an optimization problem. Starting from the identification of the variables, the objective function and the constraints, the optimization model is developed, respectively the optimization problem is formulated. In the next step, the initial solution is estimated (that is, the output quantities are evaluated based on the initial input quantities – imposed as starting values). Then, the analysis of the system is carried out, the constraints are checked, if they are satisfied, after which it is checked whether the obtained solution also satisfies the imposed convergence criterion.

If the convergence criteria are not met, the values of the input quantities (of the design variables) will be changed, based on an algorithm for searching for optimal solutions (which we will discuss in the following chapters) and the analysis of the system is returned by entering thus in a new search loop. The process is iterative until the convergence criteria are satisfied.

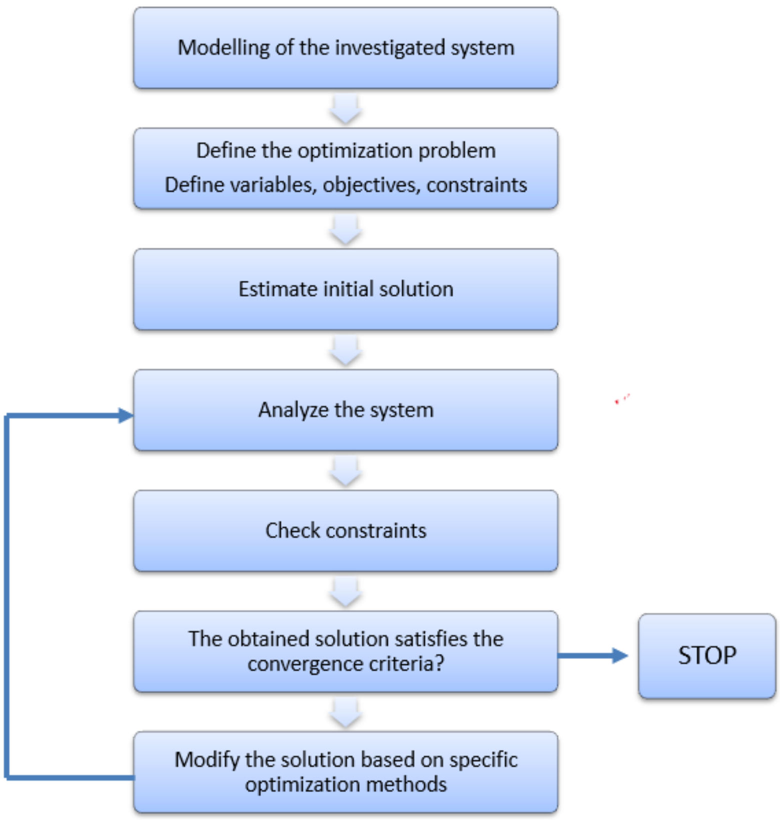

Figure 52 Steps in solving an optimization problem

There are two major categories of optimization techniques applied in mechanical engineering:

- Parametric optimization

- Non-parametric optimization

3.2 Parametric optimization

3.2.1 Description of the topic

In this optimization technique, the parameters that define the geometric model are used as design variables. In other words, all the dimensions that define a geometric shape in a model can be used as variable parameters in the optimization process. For example, the structural optimization of a cantilever beam, Figure 53, may refer to finding the values of the parameters b, h and L that will generate a beam of minimum mass m that satisfies certain imposed conditions of strength (σ) and stiffness (K_b and ω_n).

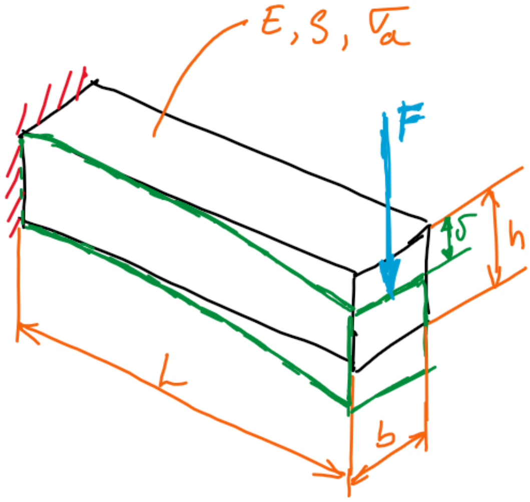

Figure 53 Cantilever beam loaded with a transverse force on the free end

This cantilever beam subjected to bending by the force F is geometrically characterized by the parameters b, h and L whose values can vary in a given range (variables / input quantities), Figure 11.

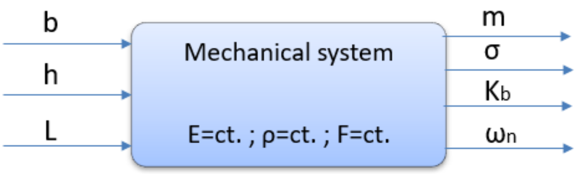

Figure 54

The modulus of elasticity *E* as well as the density ρ are material characteristics, with constant values in this example (assuming we cannot change the type of material). The responses of the analyzed system (parameters / output quantities) are in this case:

- mass m represented as a function of parameters *b*, *h*, *L* and ρ, Equation (16);
- the maximum stress in the beam σ_{max} represented as a function of the parameters *b*, *h*, *L* and *F*, Equation (17);
- stiffness K_b is represented as a function of parameters *b*, *h*, *L*, *E*, Equation (18);
- the first natural frequency ω_1 is represented as a function of parameters *b*, *h*, *L*, *E* and ρ, Equation (19).

$$m = f(b, h, L, \rho) = b \cdot h \cdot L \cdot \rho \tag{16}$$

$$\sigma_{max} = f(b, h, L, F) = \frac{6FL}{bh^2} \tag{17}$$

$$K_b = f(b, h, L, E) = \frac{3Ebh^3}{12L^3} \tag{18}$$

$$\omega_n = f(b, h, L, E, \rho) = \frac{\lambda_n^2}{2\pi}\sqrt{\frac{EI}{mL^4}} \tag{19}$$

The objective or objectives of the optimization problem as well as its constraints are defined using the responses of the analyzed system, i.e. its output parameters. In connection with the example above, we could define the optimization problem as follows:

$\boldsymbol{min\, m}$, such that:

$$\boldsymbol{\sigma_{max} \leq \sigma_{alloweble}}$$

$$\boldsymbol{\omega_1 > \omega_{imposed}}$$

$$\boldsymbol{K_b = K_{imposed}}$$

$$\underline{\boldsymbol{b}} \leq \boldsymbol{b} \leq \overline{\boldsymbol{b}}$$

$$\underline{\boldsymbol{h}} \leq \boldsymbol{h} \leq \overline{\boldsymbol{h}}$$

$$\underline{\boldsymbol{L}} \leq \boldsymbol{L} \leq \overline{\boldsymbol{L}}$$

The optimal solution can be further on reached in several ways: the most common way is to apply an automatic searching strategy on the defined model to reach the optimal solution by using one of the existing algorithms. Another way is to create a graphical map of complete possible solutions on which imposed constraints are applied and so identify the best solution for a given application. Such an example, of graphical optimization of parameterized models, is given further on.

3.2.2 Achievements

I. Graphical optimization of hierarchical sandwich structure (Velea & Lache, 2018).

When designing a lightweight structure, the type of material(s) and the shape of the structure are the most important selections to be made. With respect to the shape, an already classical solution used is represented by the sandwich concept (Zenkert, 1997), where different components are assembled in order to obtain an increased cross-section moment of inertia and therefore higher stiffness and strength to weight ratios.

Hierarchical sandwich structures represent a relatively new approach of arranging the material to increase even more the mechanical performance of the sandwich structures. Kooistra et al. (Kooistra et al., 2007) have shown that the specific strength in out of plane compression is significantly increased for a 2nd order corrugated hierarchical sandwich structure made from Aluminum alloy compared to a 1st order sandwich structure made of the same material. Yin et al. (Yin et al., 2013) have investigated the behavior of a 2nd order hierarchical pyramidal lattice structure made from CFRP. In another article, Yin et al. (Yin et al., 2014) studied the out of plane compression properties of a composite pyramidal structure where the core struts are represented by sandwich elements with a foam core. Kazemahvazi et al. have investigated the performance of all composite corrugated sandwich beams (Kazemahvazi et al., 2009; Kazemahvazi & Zenkert, 2009).

The benefit of using such a hierarchical configuration is obvious with respect to the out of plane compression properties. However, the topology of such kinds of structures is relatively complicated, with several geometric parameters that must be determined for the best mechanical performance. A way of dealing with this issue is to create failure mode maps that relate the values of the geometric parameters to the overall characteristics of the hierarchical structures (e.g. density, stiffness, strength).

Based on analytical estimates, failure modes maps are created for a novel 2nd order hierarchical sandwich structure, thus allowing searching for an optimum selection of the geometric parameters with respect to specific performance requirements. The investigated structure is produced through a simple manufacturing process from PET material, in three different forms: matrix, fiber and foam (Schneider, Velea, et al., 2015; Velea et al., 2016; Velea & Lache, 2019a). The potential benefits of using this type of material for producing different cellular structures have been also previously investigated (Kazemahvazi et al., 2015b; Poulikidou et al., 2015; Schneider et al., 2013, 2016; Schneider, Velea, et al., 2015).

The geometric parameters that describe the shape of the structure are presented in Fig. 1, where: l_1 – length of the sandwich section, l_2 – length of the monolithic section, h – height of the sandwich unit cell, t_c – thickness of the foam, t_f – thickness of the face sheets, ω – folding angle.

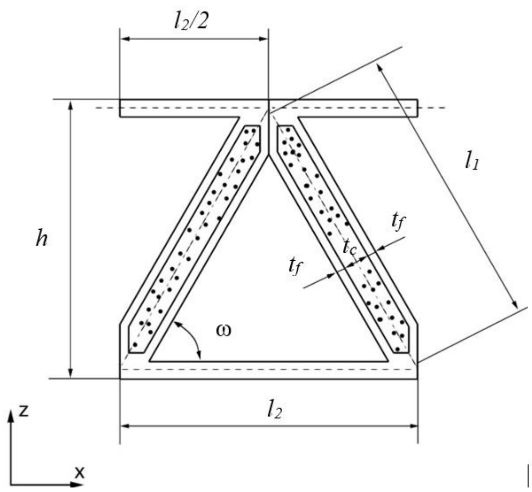

Figure 55 The unit cell of the investigated structure

The overall density of the structure shown in Fig. 1, can be derived by:

$$\rho = \rho_r \left(\rho_{solid} \frac{V_{solid}}{V_{structure}} + \rho_{foam} \frac{V_{foam}}{V_{structure}} \right) \quad (20)$$

ρ_r represents the relative density of the whole structures and it is calculated by:

$$\rho_r = \frac{l_1(t_c + 2t_f + 4t_f \cos\ \omega) + 4t_f^{\ 2}}{(t_f + l_1 \cos\omega)(4t_f + l_1 \sin\omega)} \quad (21)$$

ρ_{solid} represents the density of the solid material (1380Kgm^{-3} for SrPET) while ρ_{foam}–represents the density of the foam (100Kgm^{-3} for PET foam). *V* comes from *Volume* and V_{solid}= $(4t_f(l_1 + l_2) + t_c(t_f/2\cos\omega + t_f/2\sin\omega))b$; V_{foam}= $2l_1 t_c b$; $V_{structure}$= bhl_2 , where *b* is the width of the unit cell. The out-of-plane compressive strength of the hierarchical sandwich structure made out of SrPET material and PET foam is determined here based on the previous work of Velea et al. (Velea et al., 2016). The typical failure modes that occurred on the sandwich core elements, during experimental testing, are illustrated within Figure 56.

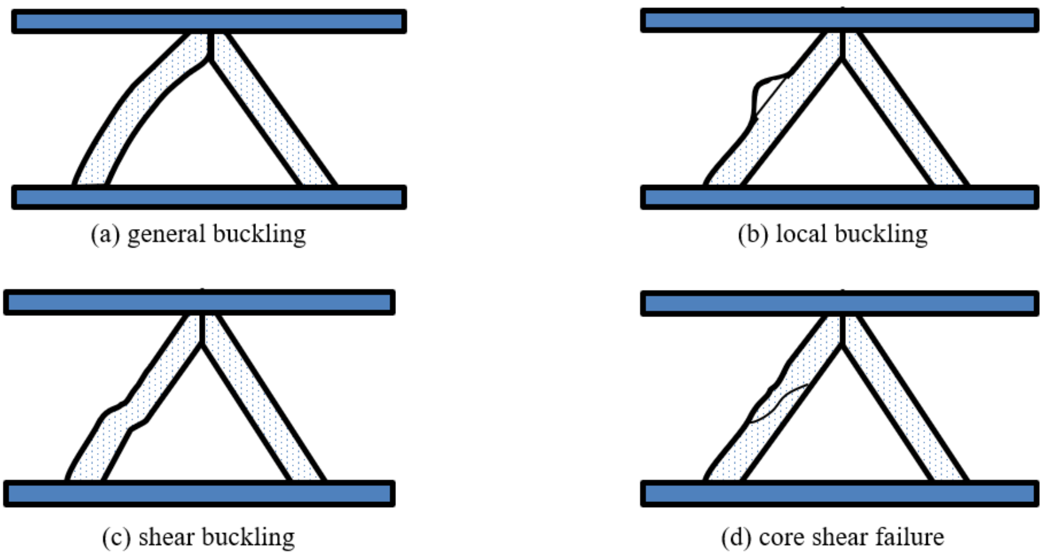

Figure 56 Failure modes of sandwich core elements

General Buckling

For longer sandwich elements and lower values for core thickness, the expected failure mode is general buckling. The compressive strength of the hierarchical structure is therefore determined by:

$$\sigma_z = \frac{2E_f\pi^2 t_f \sin\omega\left(t_c+t_f\right)^2\left(\frac{\cos\omega^2}{\frac{l_1^2\sin\omega^2}{3\left(t_c+t_f\right)^2}+\frac{t_c}{G_c\left(t_c+t_f\right)^2}}+1\right)}{l_1^2\cos\omega\left(l_1+2t_f\right)} \quad . \tag{22}$$

Local Buckling

For longer sandwich elements and lower values for core thickness, the expected failure mode is general buckling. The compressive strength of the hierarchical structure is therefore determined by:

$$\sigma_z = \frac{\sqrt[3]{E_f E_c G_c}\, t_f \sin\omega\left(\frac{\cos\omega^2}{\frac{l_1^2\sin\omega^2}{3\left(t_c+t_f\right)^2}+\frac{t_c}{G_c\left(t_c+t_f\right)^2}}+1\right)}{\cos\omega\left(l_1+2t_f\right)} \quad . \tag{23}$$

Shear Buckling

For longer sandwich elements and lower values for core thickness, the expected failure mode is general buckling. The compressive strength of the hierarchical structure is therefore determined by:

$$\sigma_z = \frac{G_c t_c \tan\omega\left(\frac{\cos\omega^2}{\frac{l_1^2\sin\omega^2}{3\left(t_c+t_f\right)^2}+\frac{t_c}{G_c\left(t_c+t_f\right)^2}}+1\right)}{l_1+2t_f} \quad . \tag{24}$$

Core Shear Failure

For longer sandwich elements and lower values for core thickness, the expected failure mode is general buckling. The compressive strength of the hierarchical structure is therefore determined by:

$$\sigma_z = \frac{\tau_c t_c \left(t_c - \dfrac{\dfrac{G_c l_1^2 (\cos \omega^2 - 1)}{3}}{G_c \cos \omega^2 \left(t_c + t_f\right)^2} + 1 \right)}{l_1 + 2t_f} \quad . \tag{25}$$

Each failure mode described previously has an associated weight that varies with the structure load carrying capacity (Vinson, 2005). It is therefore of high relevance to identify the set of geometrical parameters that assures the maximum load carrying capacity at the minimum weight, by investigating the potential failure modes. Theoretically, the minimum weight of the structure, for specific loading conditions, can be found by ensuring that the failure modes occur simultaneously (Vinson, 2005).

The failure modes maps presented in Figure 57 and Figure 58 are generated based on equations (28) to (31) that were implemented and calculated within a Matlab script. For this case, a set of 5 contour lines are obtained:

- the density of the structure calculated (black contour lines), according to equation (27);
- the strength for the general buckling failure mode (blue contour lines), according to equation (28);
- the strength for the local buckling failure mode (red contour lines), according to equation (29);
- the strength for the core shear buckling failure mode (yellow contour lines), according to equation (30);

- the strength for the core shear failure mode (green contour lines), according to equation (31).

For a constant value of 60° of the corrugation angle ω, it can be observed from Figure 57 that three failure modes occur simultaneously for the case when the t_c/t_f ratio has a value of about 9.4 while the length of the sandwich strut l_1 is about 33 mm. The strength contour lines indicate a maximum out of plane compression strength of about 5.5 MPa at the point where the lines of the corresponding failure modes intersect. For the same intersection point, the density contour lines indicate a value of 75 Kg m-3.

Figure 58 helps to identify the influence of the corrugation angle ω to the out of plane compression strength of the structure. For an increase in strength value, the ω angle should be increased. This will however add additional weight to the structure as it can be seen from the density contour lines, Figure 58.

The solid circles from Figure 57 indicate the configurations (I, II, III, IV) that were experimentally investigated in a previous article of Velea et al. (Velea et al., 2016). Configurations II, II and IV have been correctly predicted by using the failure modes maps. For configuration I, it was experimentally found (Velea et al., 2016) that the local buckling failure mode occurred first while on the failure mode maps the core shear failure mode will occur first. This is however close to the border of the local buckling failure mode, see Figure 58, and the difference is most probably caused by the values of the geometric parameters (theoretical values vs. actual values of the experimentally tested specimens) (Velea et al., 2016).

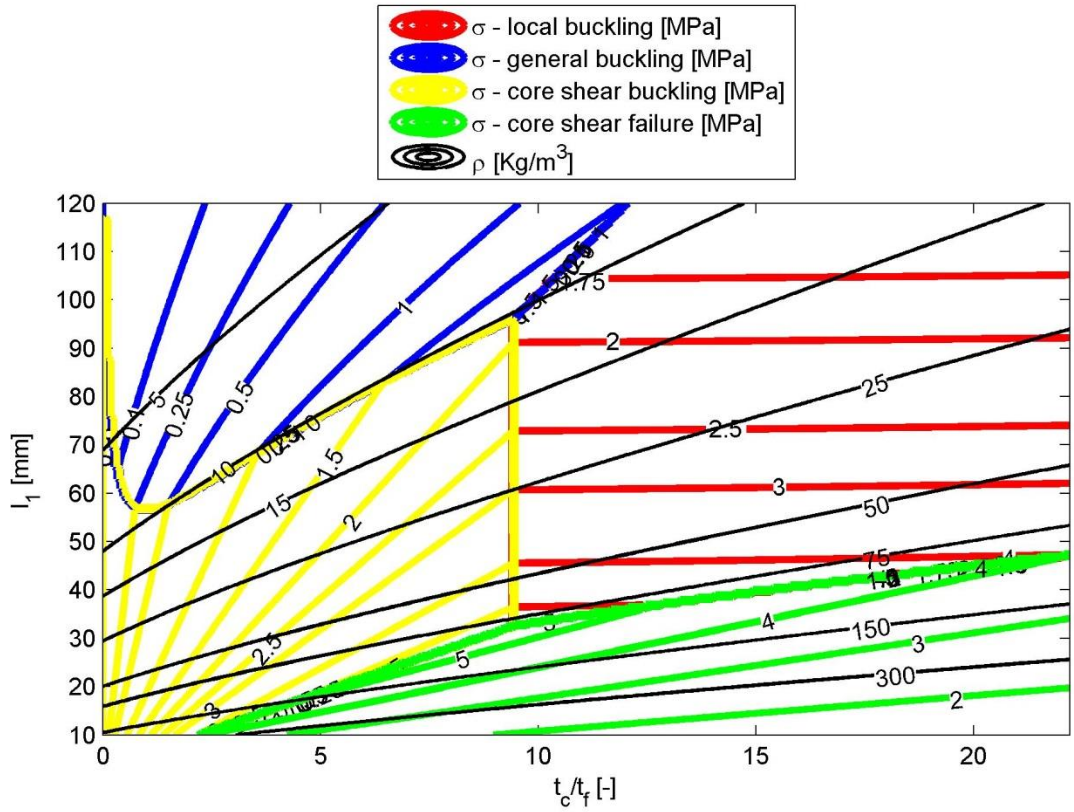

Figure 57 Failure modes maps for the investigated 2nd order hierarchical sandwich structure made from SrPET material and PET foam by assuming ω=60°

Such mode maps allow identifying the optimum geometric parameters for certain loading conditions by ensuring that at least 2 failure modes have a high probability to occur simultaneously.

For the investigated 2nd order hierarchical sandwich structure, the best mechanical performance in out of plane compression, with respect to weight, can be achieved for t_c/t_f=9.4, ω=60° and l_1=33mm. This is the configuration for which the local buckling, the core shear buckling and core shear failure modes will most probably occur simultaneously. For this specific configuration, the corresponding strength value is 5.5 MPa. If required, an increase in strength can be achieved by increasing the angle ω; however, this measure will also increase the weight of the structure.

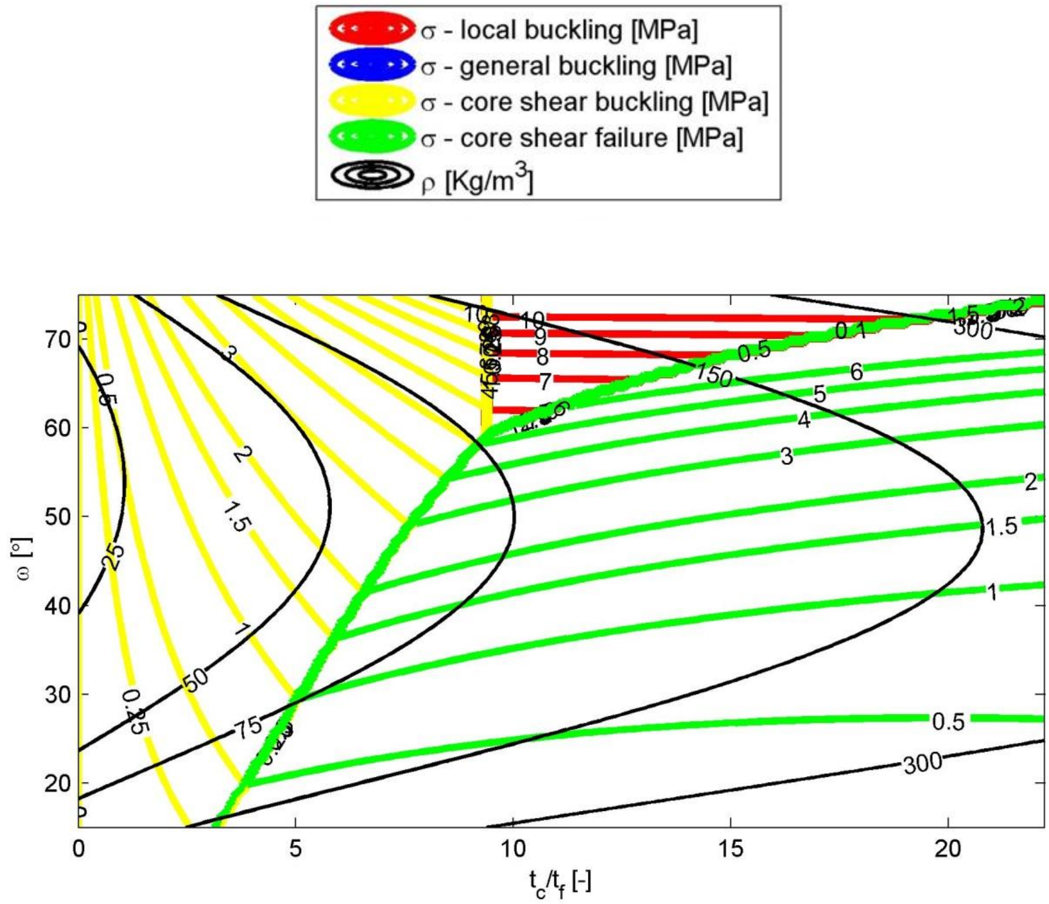

Figure 58 Failure modes maps for the investigated 2nd order hierarchical sandwich structure made from SrPET material and PET foam by assuming l1=33mm

II. Study case: Axial brake optimization

This example demonstrates how parametric optimization can be applied also on mechanical systems not only on mechanical structures. The application relates to an axial brake which is coupled / decoupled by a small linear actuator, Figure 59. The interest here is to succeed in braking axial forces as large as possible by acting with as little force as possible provided by the linear actuator at the same time by not exceeding the allowable contact pressure on the friction pads and by keeping a compact size for the overall system (minimizing travel distance of the actuator). An analytical model is therefore needed that describes the relevant functional behavior of the investigated system. This analytical model has been written in this case into an excel sheet, where each relevant parameter, for each component, is considered, as shown in Figure 60.

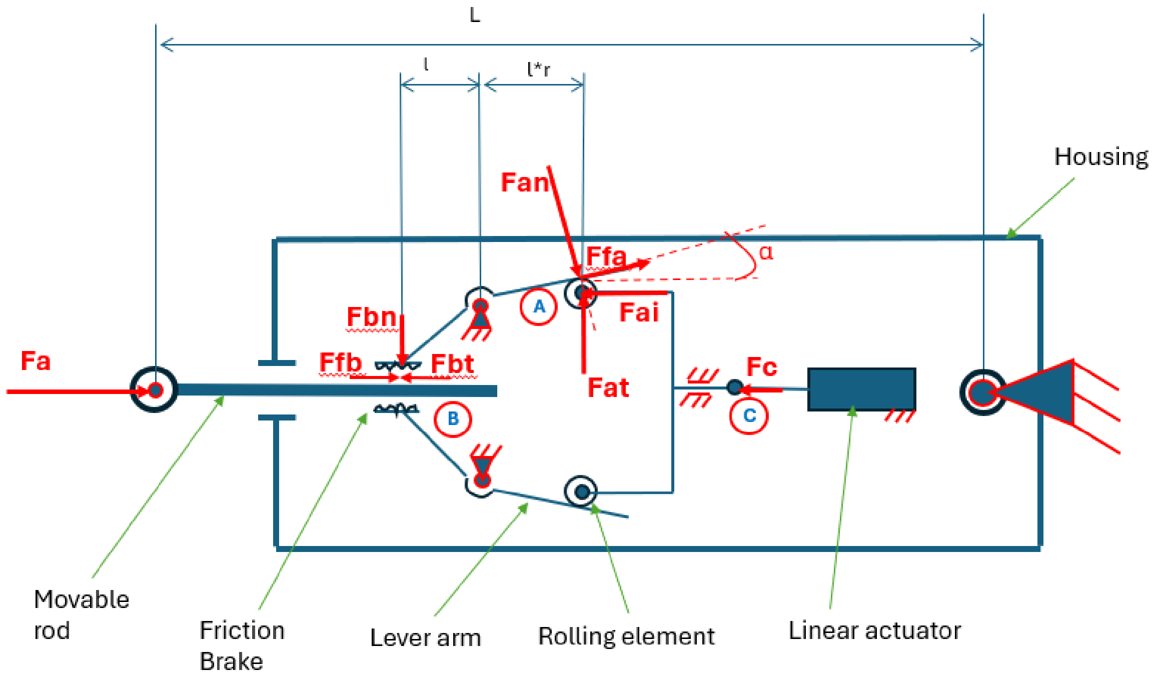

Figure 59 The investigated axial brake concept

Movable rod

Inputs			
Geometry			
Diameter	**d**	29.1142	mm
Loads			
Axial force	**Fa**	1000.0	N
safety factor	**beta**	1.5	-
Calculation force	**Fa**	1500	N

Brake

Inputs			
Geometry			
Friction surfaces (two pair pads)	**i_pads**	4	-
Friction radius	**Rmed**	14.5571	mm
Width of the pads	**l_pads**	40	mm
angle	**alpha**	90	deg
Friction area	**A**	3659	mm^2
Distance required to unlock the system	**du**	1	mm
Friction coefficient	**mu**	0.55	-
Loads			
Axial Force	**Fbt**	1500	N
Outputs			
Force needed to brake	**Fbn**	2727.3	N
Specific pressure	**p**	0.745	MPa

Lever arm

Inputs			
Geometry			
Length l	**l_lever**	49.9935	mm
Ratio	**r_lever**	5	-
Loads			
Force at point B required to lock	**Fbn**	2727.3	N
Outputs			
displacemnt of point A	**delta_A**	5	mm
Force at point A required to brake	**Fa**	545.5	N

Rolling elements and connical part

Inputs			
Geometry			
Angle	**alpha**	0.50	deg
Friction coefficient	**mu**	0.002	-
No of arms - rollers		2	-
Loads			
Force	**Fa**	545.46	N
Outputs			
Bending force on the arm	**Fat**	545.409	N
travel distance	**travel_actuator**	572.943	mm
Required force to brake	**Fai**	5.74	N

Actuator

Inputs			
Axial force	**Fc - actuator force**	11.5	N

Figure 60 Analytical model implemented within an excel sheet

Next step is to define the optimization problem based on the analytical model described above. This is done by using the Hyperstudy application from Altair®.

Figure 61 shows the selected input variables with the associated lower and upper boundary limits.

Bounds | Modes | Distributions | Links | Constraints

+ Add Input Variable | Remove Input Variable

	Active	Label	Varname	Lower Bound	Nominal	Upper Bound	Comment
1	☑	d	var_1	15.000000	20.000000	30.000000	
2	☑	i_pads	var_2	1.0000000	2.0000000	4.0000000	
3	☑	l_lever	var_3	10.000000	40.000000	50.000000	
4	☑	r_lever	var_4	1.0000000	3.0000000	5.0000000	
5	☑	alpha	var_5	0.5000000	1.8000000	10.000000	
6	☑	mu	var_6	0.3000000	0.5000000	0.5500000	

Figure 61 Input variables with the specified boundary conditions

Each input variable it is link to the corresponding cell in the excel file and can take discrete or continuous numbers, as it is shown in Figure 62.

Bounds | Modes | Distributions | Links | Constraints

+ Add Input Variable | Remove Input Variable

	Active	Label	Varname	Model Parameter	Model Type	Data Type	Format	Distribution Role
1	☑	d	var_1	m_1.row_6.col_4.C06_V2	Spreadsheet	Numeric	Continuous	Design
2	☑	i_pads	var_2	m_1.row_15.col_4.C06_V2	Spreadsheet	Numeric	Step: 1	Design
3	☑	l_lever	var_3	m_1.row_32.col_4.C06_V2	Spreadsheet	Numeric	Continuous	Design
4	☑	r_lever	var_4	m_1.row_33.col_4.C06_V2	Spreadsheet	Numeric	Step: 1	Design
5	☑	alpha	var_5	m_1.row_45.col_4.C06_V2	Spreadsheet	Numeric	Continuous	Design
6	☑	mu	var_6	m_1.row_21.col_4.C06_V2	Spreadsheet	Numeric	Continuous	Design

Figure 62 Input variables with the specified path to the analytical model (excel sheet)

The selected output parameters are show within Figure 63. For each of them, a goal is specified which can be an objective (minimize or maximize) or a constraint.

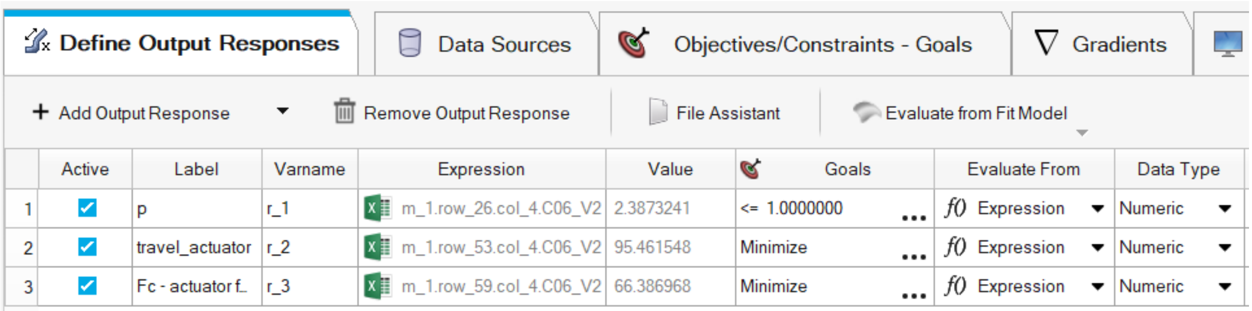

Figure 63 Output variables used to define the objectives and constraints

For this specific optimization problem, two objectives were considered which means that we must solve a multi-objective optimization problem. Two algorithms are available in Hyperstudy that can deal with multi-objective problems: GRSM – Global Response Search Method and MOGA – Multi-Objective Genetic Algorithm. The first one is selected for solving this specific problem.

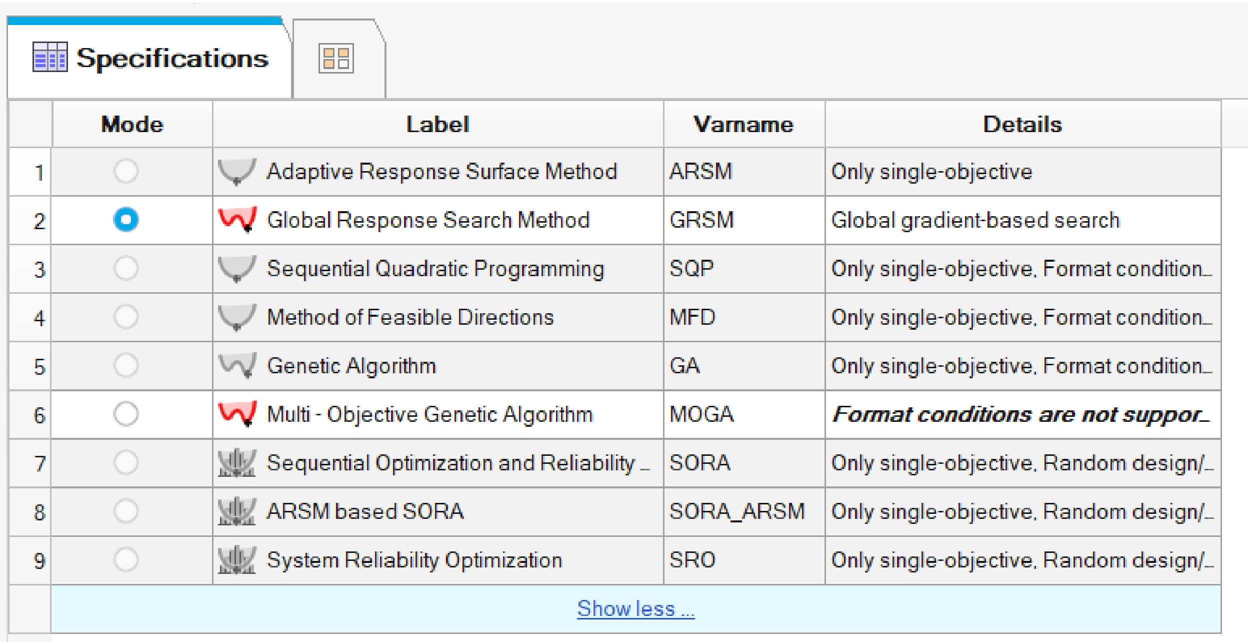

Figure 64 Available types of algorithms for solving the defined optimization problem

The graphs shown in Figure 65 and Figure 67 indicates the dependence between the actuator force and the required travel distance to brake 1500 N force applied on the movable rod.

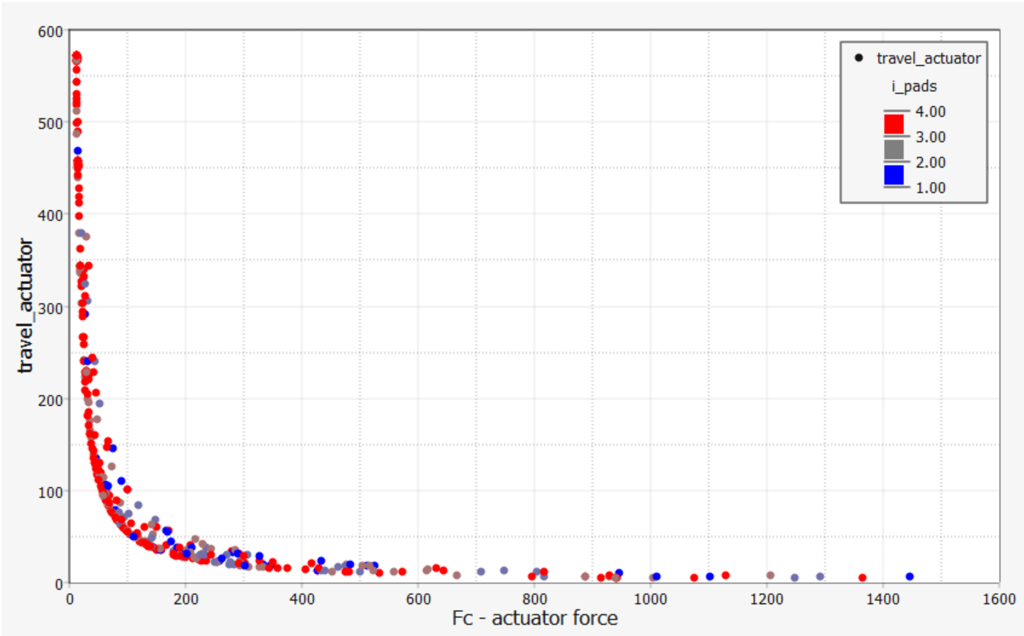

Figure 65 All calculated solution. Trade-off between actuator force and the required travel distance while indicating the number of friction pads

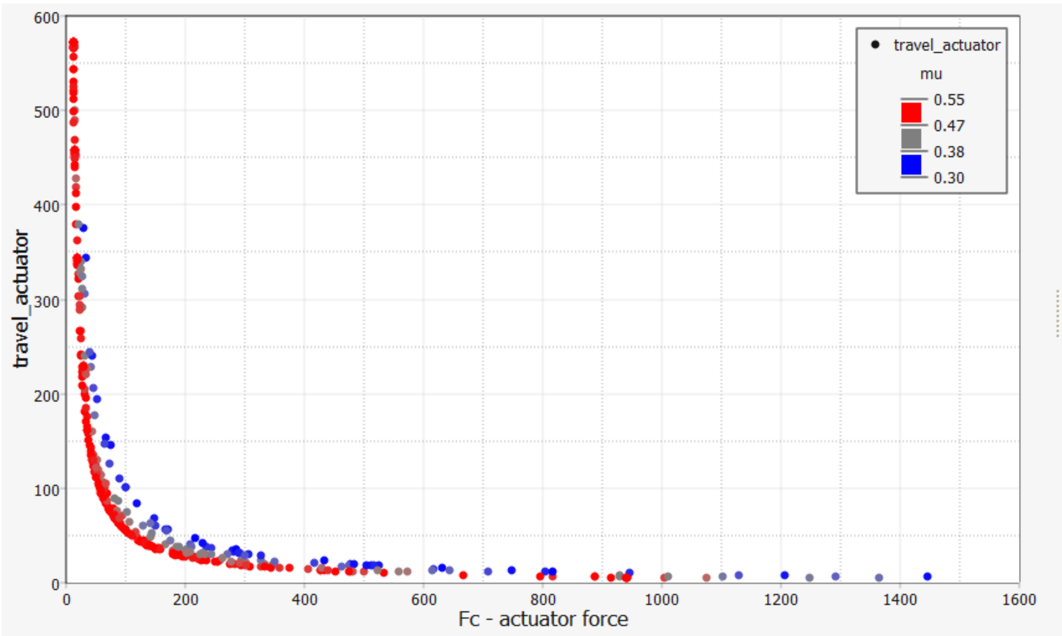

Figure 66 All calculated solution. Trade-off between actuator force and the required travel distance while indicating the required value of the friction coefficient

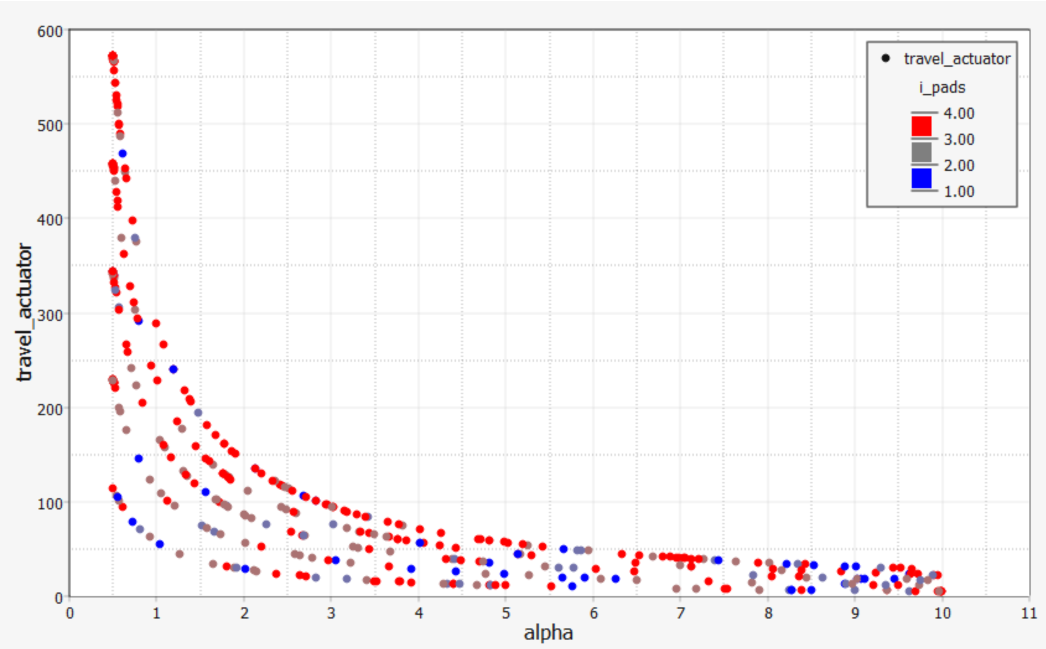

Figure 67 All calculated solution. Trade-off between alpha angle (see Figure 59) and the required travel distance

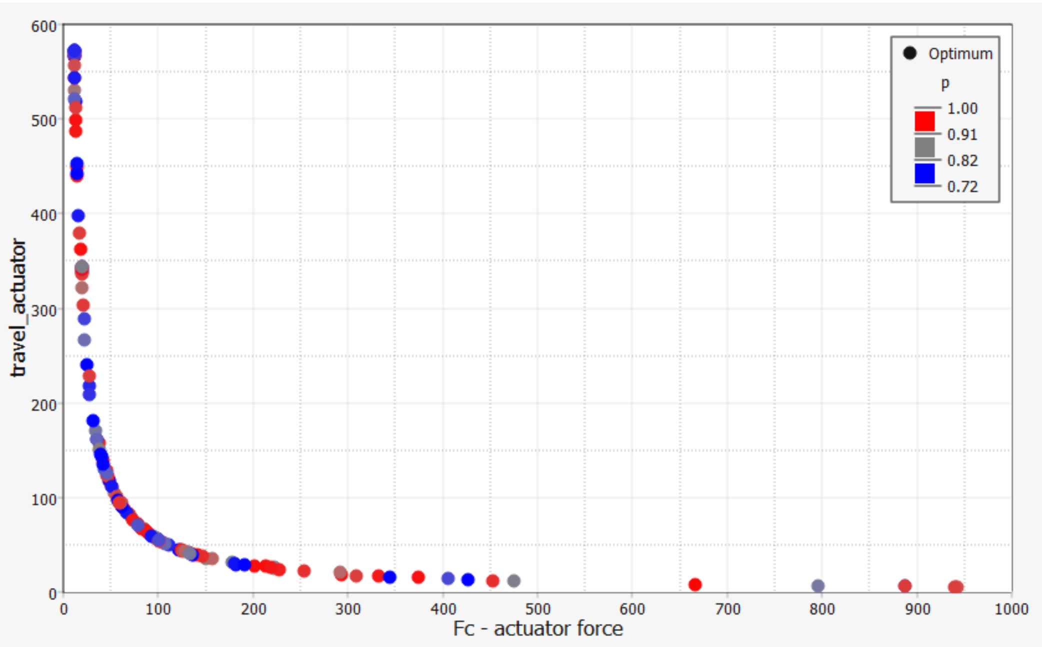

Figure 68 Set of optimal solutions (Pareto front) while negotiating between actuator force and the required travel distance

At the same time, the required number of friction pads for each calculated solution is visible in Figure 65 (bullets color) while the required friction coefficient can be viewed in Figure 66.

Figure 67 indicates the way in which the alpha angle influences the travel required for the actuator to lock the 1500 N load at the same time while specifying the number of friction pads which are needed.

The set of optimal solutions (Pareto front) while negotiating between actuator force and the required travel distance is shown in Figure 68 together with the results contact pressure between the friction pads (colored bullets).

In the same way, the objectives of interests can be plotted in terms of other input variables or output parameters to facilitate the selection of the most beneficial solution from the set of optimal solutions (the Pareto front).

3.3 Non-parametric optimization

3.3.1 Description of the topic

The non-parametric optimization is usually referring to multiple techniques for doing structural optimization, applied on finite element models, such as:

- Topology optimization
- Shape optimization
- Topography optimization
- Free-size optimization
- Size optimization

The most known and used technique is the topology optimization which involves searching for the optimal distribution of material in a given volume, discretized with finite elements. During the topologic optimization process, the elements that are not useful from a structural point of view are deleted - topological optimization (Figure 69).

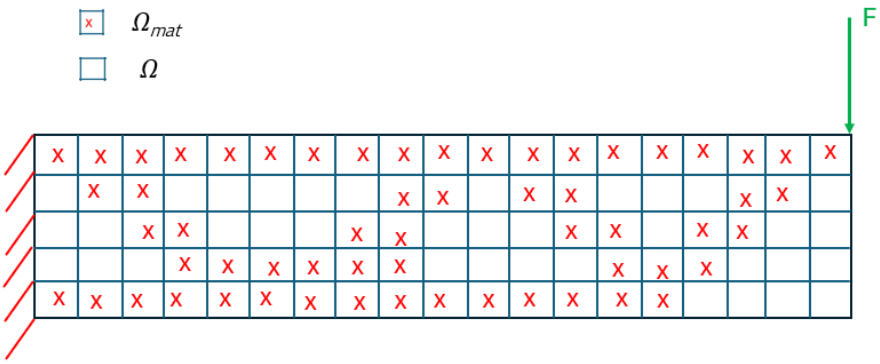

Figure 69 Topologic optimization

Mathematically, topological optimization searches for a subset $\Omega_{mat} \subset \Omega$ where Ω is the searchable domain (initial volume) and the design variables are represented by the densities of each finite element.

Within the shape optimization technique (Figure 70), the positions of the nodes of the finite elements are changed - such that to achieve the desired objective at the same time as satisfying the imposed constraints. It means that the shape of the finite elements will be altered (either by extension or compression) to reach the desired objective while satisfying the imposed constraints. This technique may be applied on both 2D or 3D finite element models.

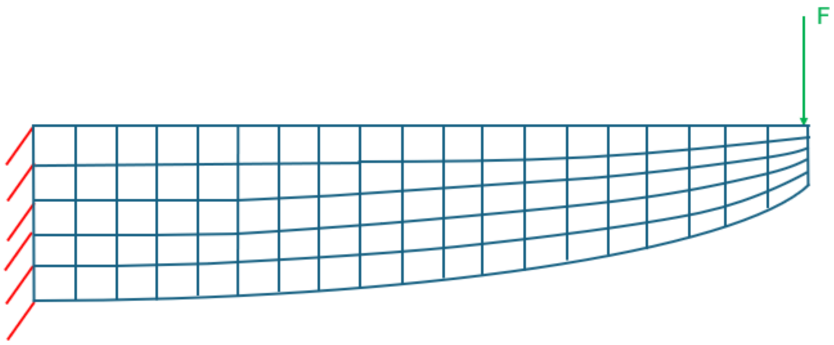

Figure 70 Shape optimization

Topography optimization (Figure 71) is changing the shape of discretized surfaces to, for example, increase the stiffness of the structures. Topography optimization is normally applied on 2D finite element models.

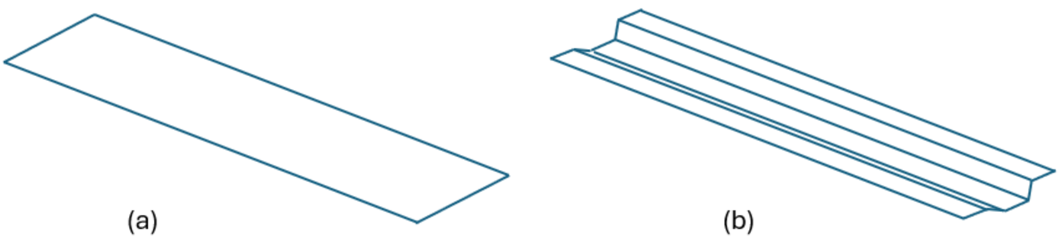

Figure 71 Topography optimization

In case of a free-size optimization problem, Figure 72, the thickness of each 2D finite element which is part of the design space, is modified independently according to the specified objectives and constraints.

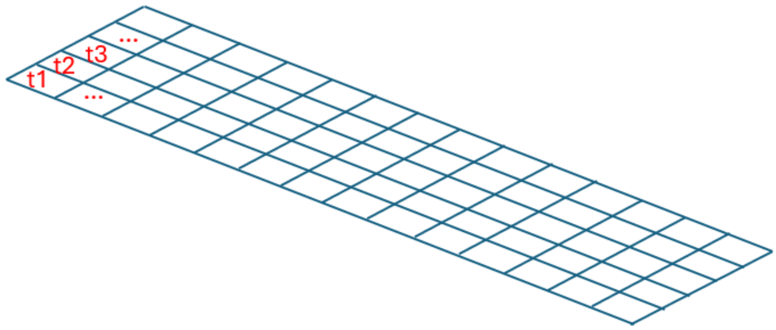

Figure 72 Free-size optimization

A size optimization problem will also modify the thickness of 2D finite elements only that this is done not for each finite element independently but for specified sets of elements (patches), as it is described in Figure 73.

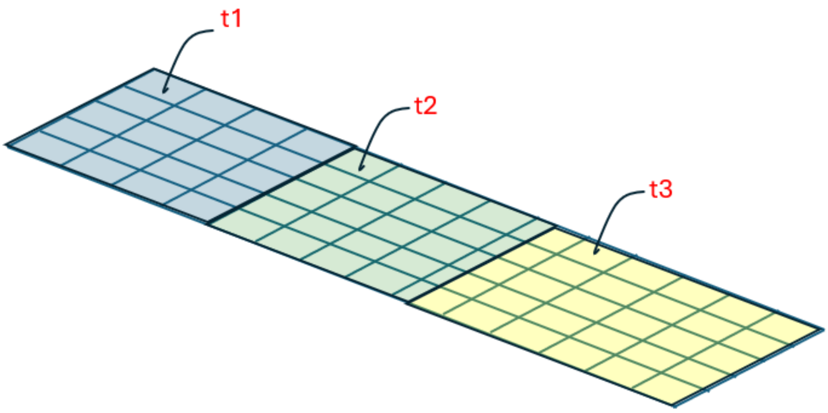

Figure 73 Size optimization

3.3.2 Achievements

I. Topology optimization of high-temperature pressure vessel of a 20KW ThermoLift Heat Pump (Research project coordinated by Velea M. N., 2019)

The present work describes the process and methodology of optimizing thermomechanical stressed components with the aim of reducing the amount of material used to make the part. The need for structural optimization of these components arises, first, from economic reasons, namely, to reduce material costs, as very expensive materials are used (Inconel 718, Stainless steel 316, SS17-4PH). These components are part of a heat pump that ensures both the heating or cooling of the internal temperature of a building complex and the heating of domestic water.

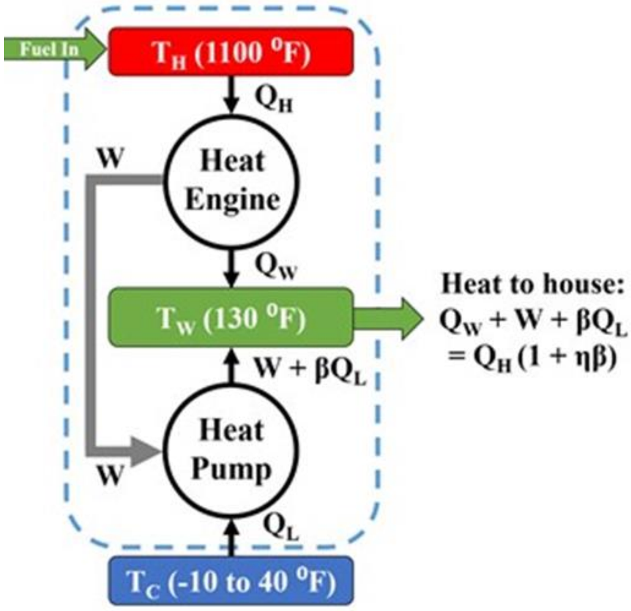

Figure 74 Description of the working principle for the investigated heat-pump

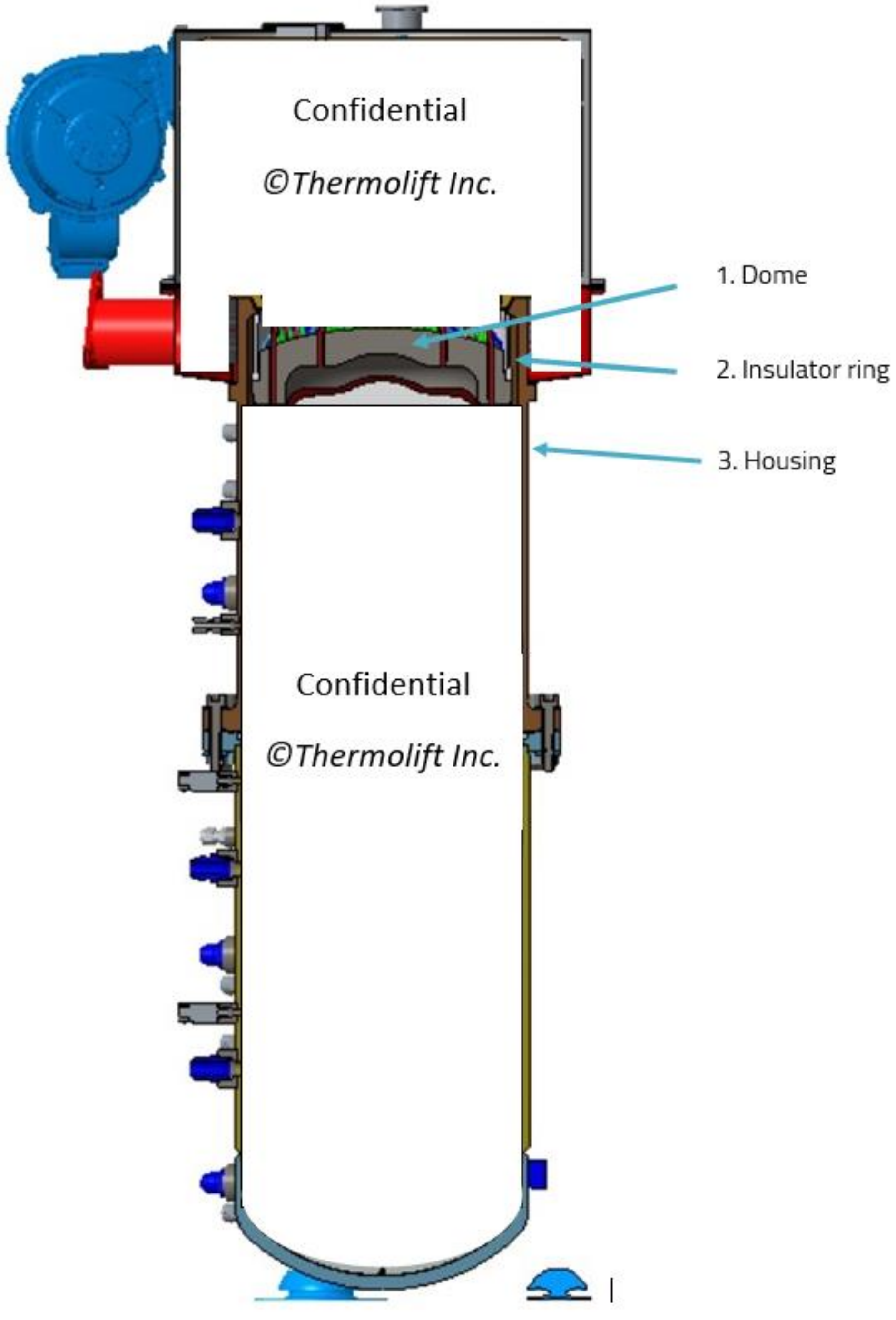

Figure 75 Parts of interests within the optimization process

The dome is a very important component for the whole pump. It takes a large part of the stress and transmits it through the insulating ring in the pump housing. It is subject both to high mechanical stresses resulting from internal pressures and to stresses due to high temperatures applied to it. It is desired to optimize it primarily to reduce the cost of the material from which it is made, but also to make the internal space of the heat pump more efficient. Currently the part is made of stainless-steel type 316 and weighs about 12.7 kg (Figure 76 and Figure 77).

The dome features a precise number of bores arranged radially in several rows. Stainless steel tubes will later be installed in these bores. For privacy reasons, these components are not shown here.

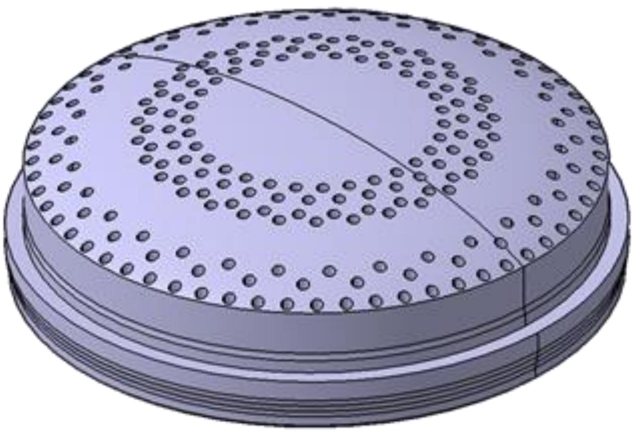

Figure 76 Initial geometry of the dome (upper part)

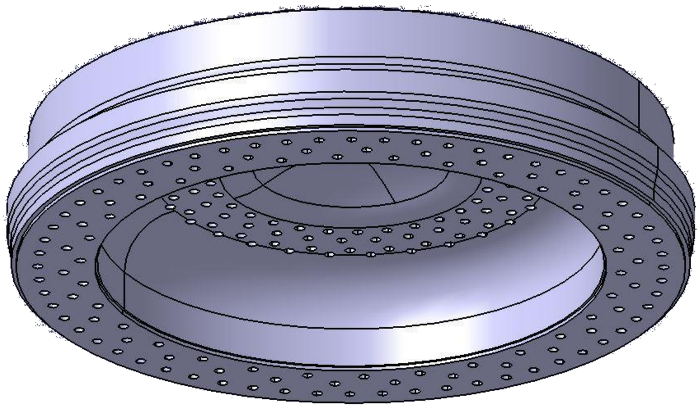

Figure 77 Initial geometry of the dome (bottom)

The insulating ring is a component that fulfills two functional roles: the role of mechanical resistance, being the most loaded component in the whole assembly, as well as the role of thermal insulation between two rooms with different temperatures. It is made of a steel alloy with very high mechanical properties (Inconel). The price of the material is high, which is why it is desired to optimize it or, if possible, to replace the existing material with another cheaper one, but without the mechanical properties of the entire system being affected by this change.

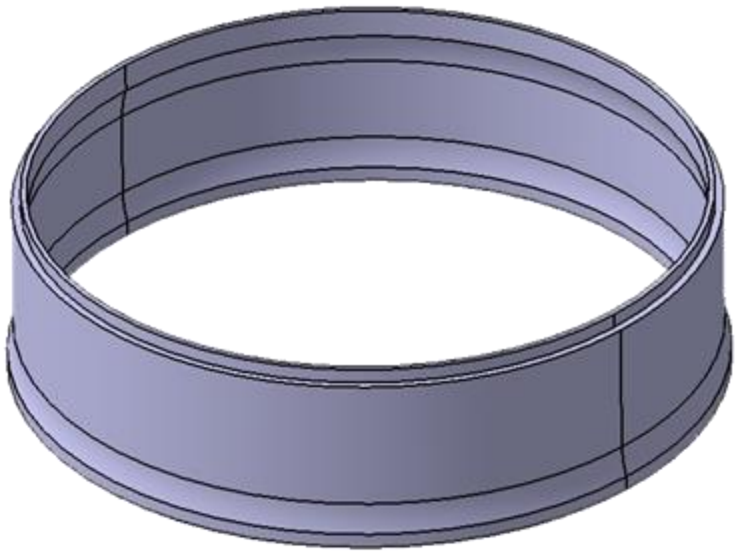

Figure 78 The initial geometry of the insulator ring

The housing has both the role of strength and stiffness to combine stresses and the role of supporting the components of the assembly. It also provides insulation of the systems against environmental factors and the necessary mechanical protection for the elements inside them. The housing was not subjected to the optimization process. However, it was included into the optimization model to make the model as close as possible to reality regarding the stresses and displacements obtained.

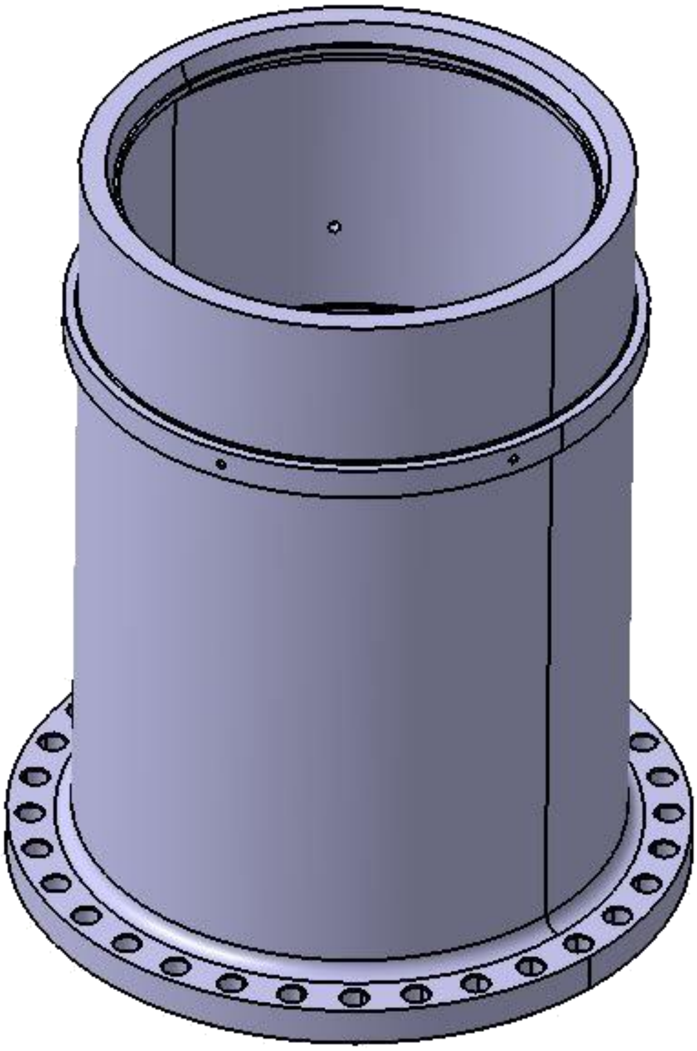

Figure 79 Housing

The assembly of the three components, dome, insulator ring and housing will be done by welding.

The thermal demands inside this heat pump are shown in Figure 80. The highest temperature is recorded in the upper and lower part of the dome.

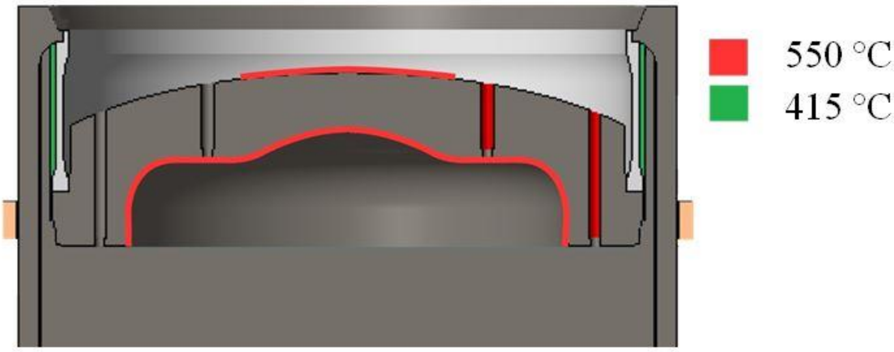

Figure 80 Thermal loads

The mechanical loads are generated by the pressures developed inside the pump while it is running. The highest loads are present at the level of the dome - 120 bar applied on the inferior side of the dome (Figure 81).

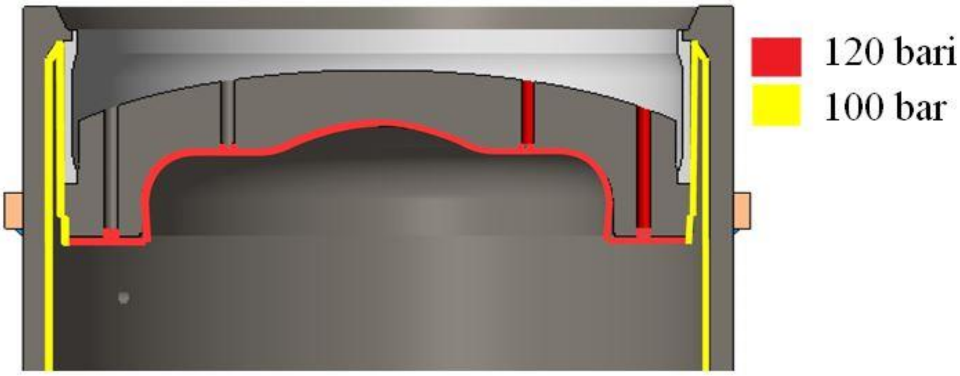

Figure 81 Mechanical loads

Altair Inspire software was used for the optimization procedure. The main reason for choosing this software is that thermal and mechanical stresses can be considered at the same time in the optimization analysis. Another advantage offered by the Altair Inspire analysis program is the speed of the work mode for the preparation of an analysis model, but also the algorithm that provides a result in a much shorter time compared to other competing software (the discretization method is automatic). The user has the freedom to enter a minimum element size for different elements. If this value is not filled in by the user, the software will automatically assign an element size based on the dimensions of the part in question.

Of course, this speed in work offered by this program leads to disadvantages. A simplification of certain optimization settings and constraints is noted. A major drawback observed while using this program is the impossibility of defining material properties as a function of temperature. As a solution to this problem, the introduction of material properties according to the maximum temperature applied to them was considered.

Three materials are used in the analysis, stainless steel type 316, steel 17-4PH, and Inconel 718, which have the properties in Figure 82.

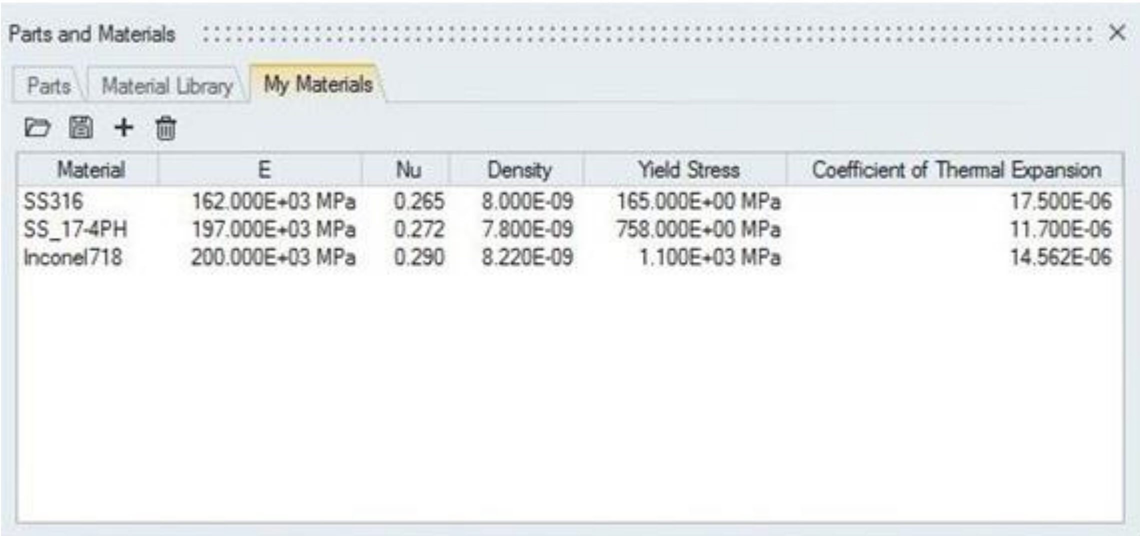

Material	E	Nu	Density	Yield Stress	Coefficient of Thermal Expansion
SS316	162.000E+03 MPa	0.265	8.000E-09	165.000E+00 MPa	17.500E-06
SS_17-4PH	197.000E+03 MPa	0.272	7.800E-09	758.000E+00 MPa	11.700E-06
Inconel718	200.000E+03 MPa	0.290	8.220E-09	1.100E+03 MPa	14.562E-06

Figure 82 Defining the properties of the materials used

In Figure 83 the total displacements of the initial system configuration is shown. The maximum displacement has a value of approximately 1.2 mm and is recorded at the level of the dome on the side at its contact with the insulating ring. A significant part of these displacements is due to thermal expansion.

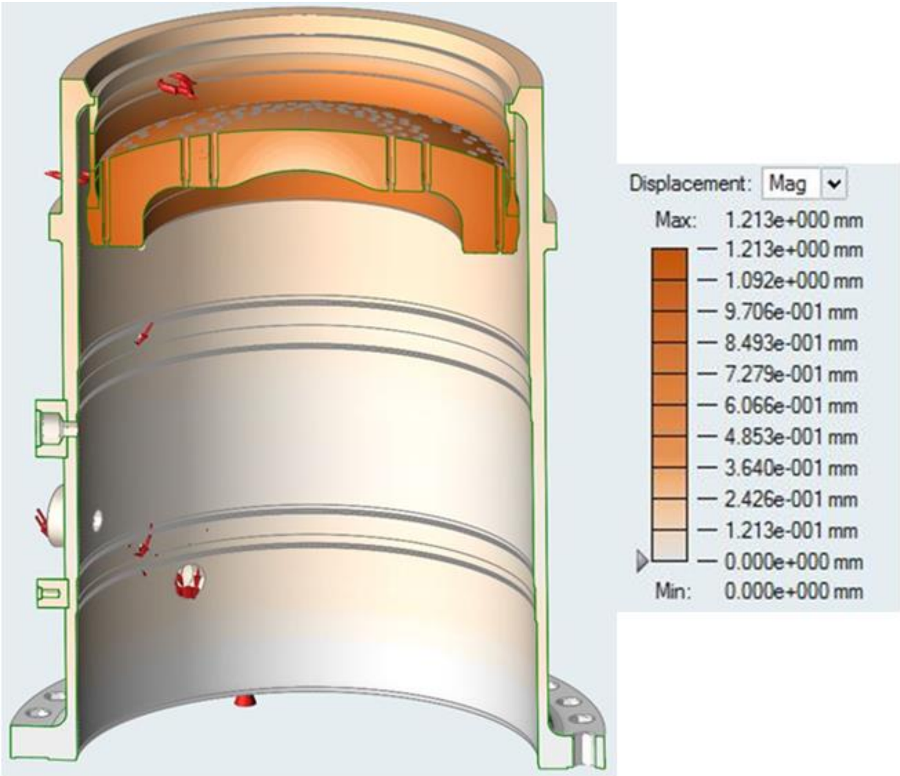

Figure 83 Displacements for the initial configuration

Figure 84 shows the von-Misses stresses that develop during pump operation. The highest stress values are recorded at the level of the insulating ring, around the contact with the housing, where a stress value of about 900 MPa is recorded. This stress values do not reach the yield strength of the material at that temperature. Very high peak stress was recorded which were not considered at this stage of the work, because they are originated by the stress concentrators.

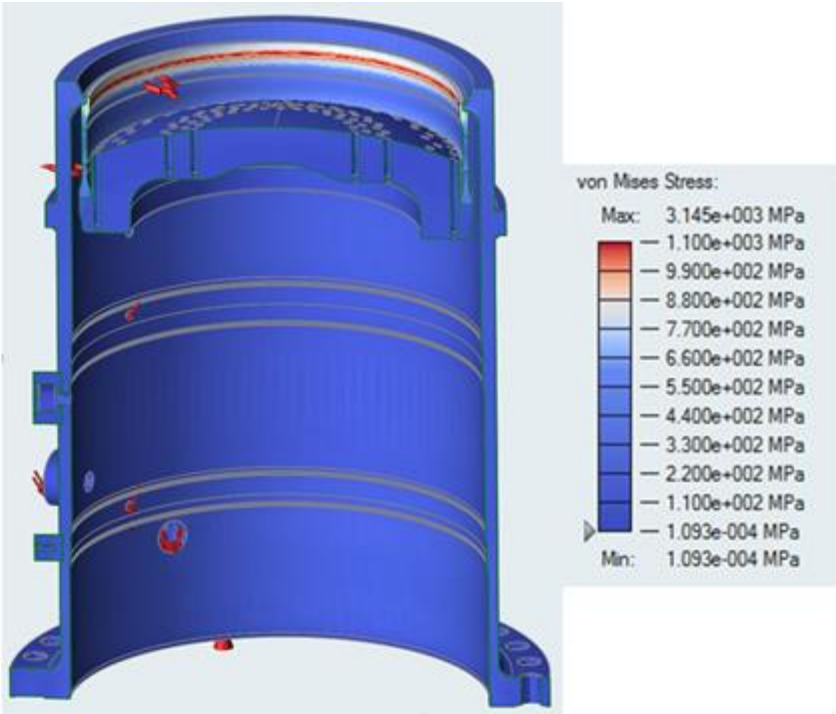

Figure 84 Stresses obtained for the initial configuration

Figure 85 shows the sketch with the initial and extended volume of the component. Both the constraints imposed by contact interface with other components and the maximum available space were considered. The outline of the initial geometry was represented with a yellow line and with a blue line the contact surfaces with other components. These surfaces are not frozen, meaning that they will be kept intact within the optimization process.

Figure 86 indicates the total volume considered as design space for the topology optimization process.

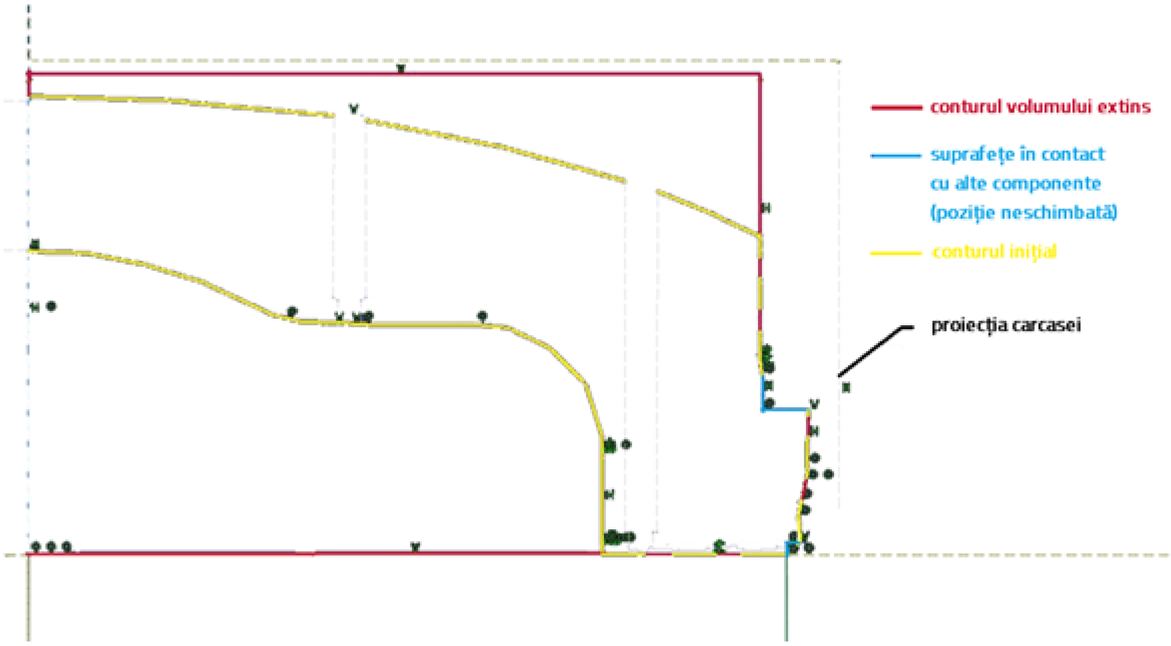

Figure 85 Volume expansion for the dome component – determine the interference limits with the adjacent components

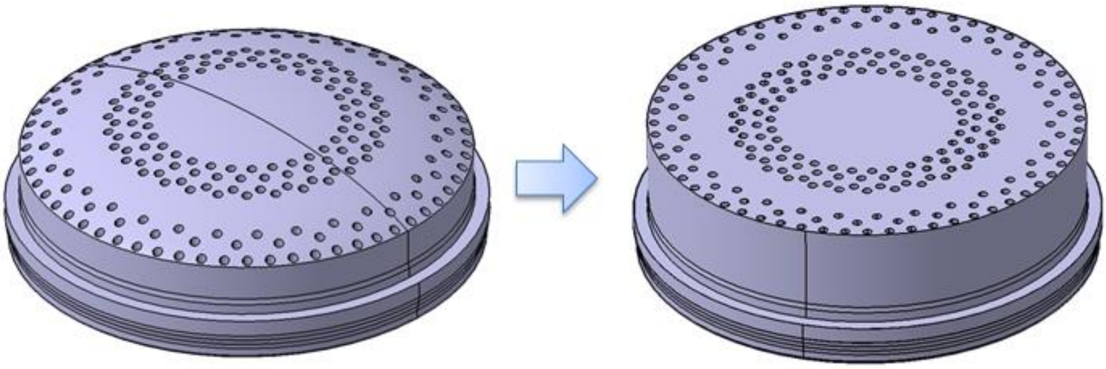

Figure 86 Volume expansion for the dome component

Figure 87 indicates the volume extension for the insulator ring by considering the interference limits with the adjacent components. The resulted volume is shown in Figure 87.

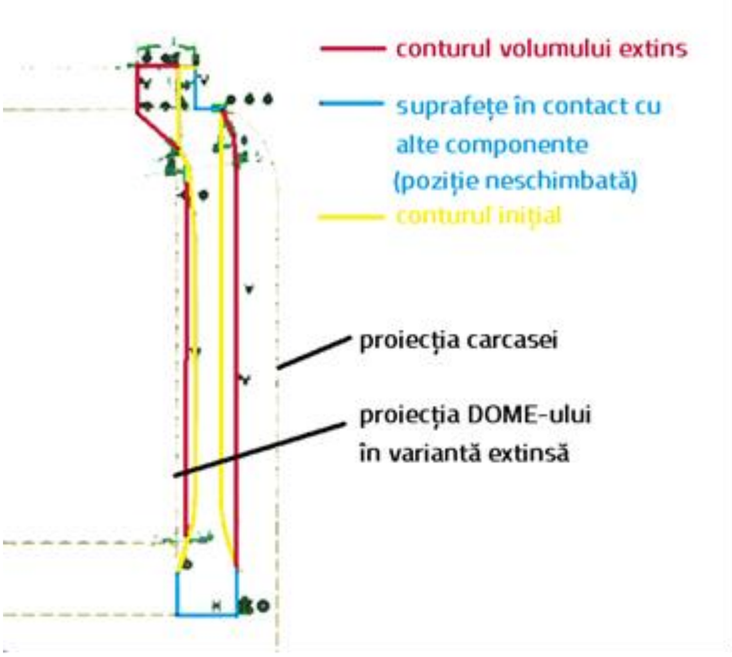

Figure 87 Volume expansion for the insulator ring – determine the interference limits with the adjacent components

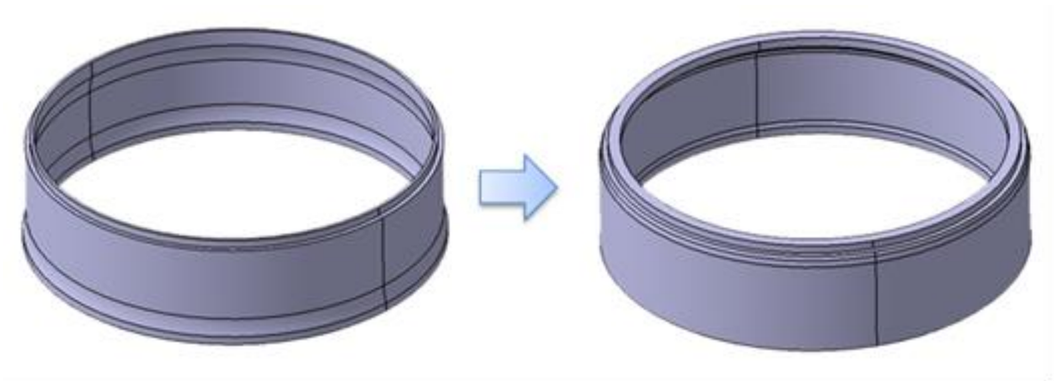

Figure 88 Volume expansion for the insulator ring

Two topological optimization methods were chosen for the optimization process of the studied parts. Both methods were run in parallel to obtain and compare the results.

Method 1:

Objective: to maximize the stiffness of the components.

Constraint: Final volume to be up to 30% of initial volume

Method 2:

Objective: Mass minimization

Constraint: safety factor 1.2

For both methods, a minimum thickness of stiffening elements greater than or equal to 9 mm was chosen, Figure 89. Axial symmetry constraints were also imposed on the dome geometry, Figure 90, by defining 50 symmetry planes.

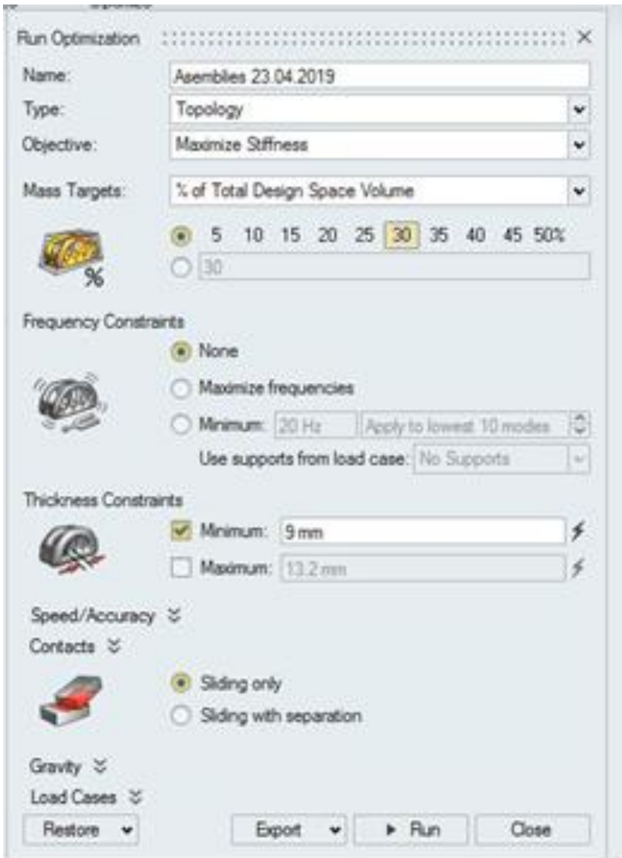

Figure 89 Topology optimization set-up

Multiple optimization processes were carried out. It was also observed that the definition of symmetry planes, as shown in Figure 90, helped to reduce the calculation time from several tens of hours to a few hours.

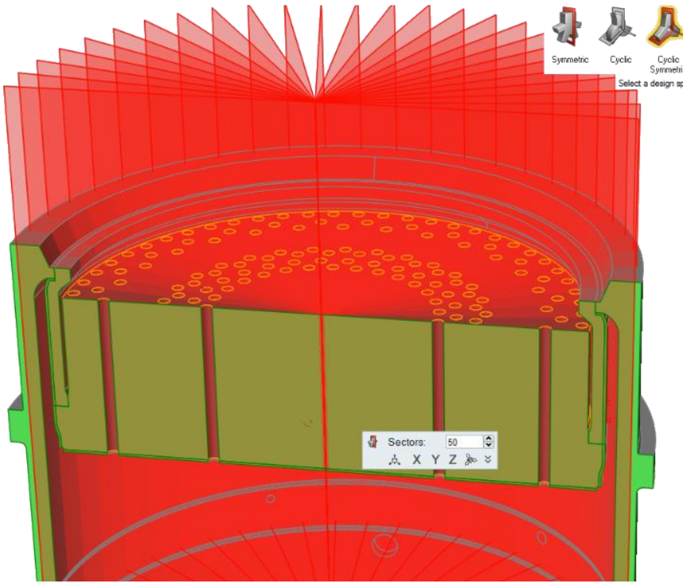

Figure 90 Axial symmetry planes applied on the dome geometry

The results presented below (Figure 91) represent the best variant found as a constructive solution, this being obtained using the first method, respectively by maximizing the stiffness and by imposing a volume fraction limit of 30%.

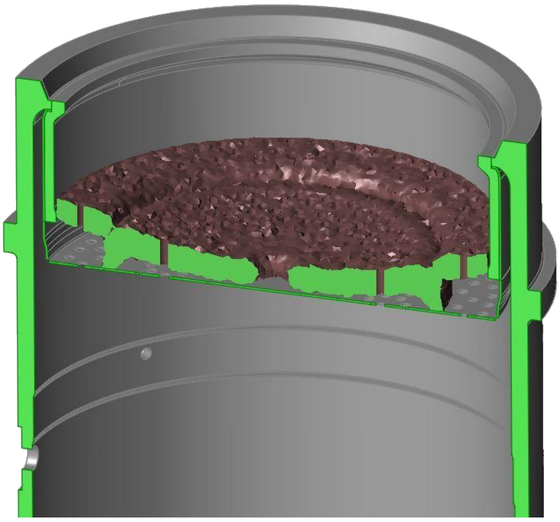

Figure 91 Best topology obtained for the dome – indicates a better behavior of the dome if the curvature is reversed

Form Figure 91 it can be observed an unexpected behavior which is that the dome geometry is curved in the opposite direction. By following this idea, the geometry has been reconstructed, Figure 92, such that more available design space exits on the bottom side.

Figure 92 Initial volume is extended on the bottom side of the dome.

Figure 93 illustrates the obtained topology after the optimization process where mass minimization was considered with an imposed safety factor of 1.2.

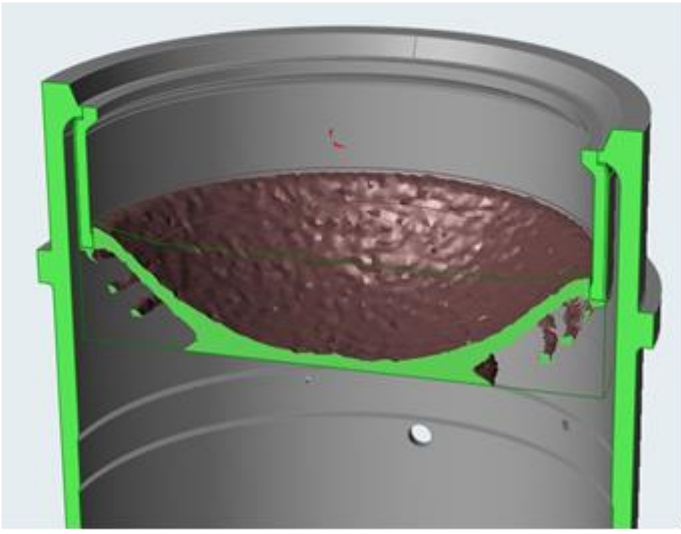

Figure 93 The best topology obtained for the dome

Based on the best topology obtained (Figure 93) the dome geometry has been reconstructed as shown in Figure 94.

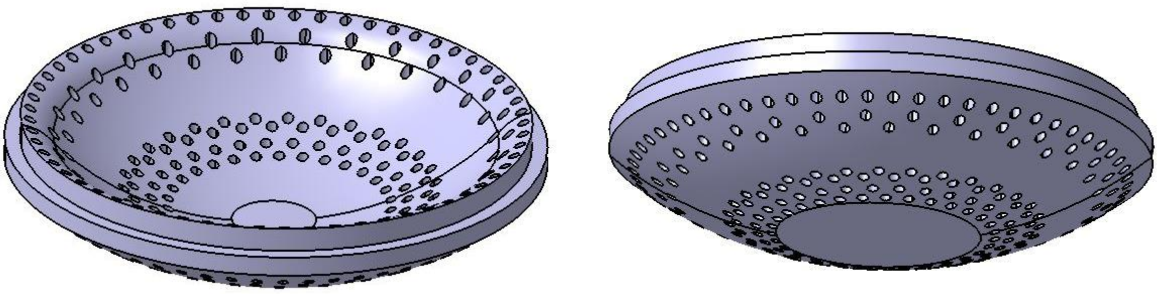

Figure 94 Dome geometry after reconstruction based on the topology optimization results

While optimizing the insulator ring, it was observed a tendency of the algorithm to produce a curvature towards the exterior (Figure 95). This shape will be taking into consideration while reconstructing the geometry of the insulation ring (Figure 96).

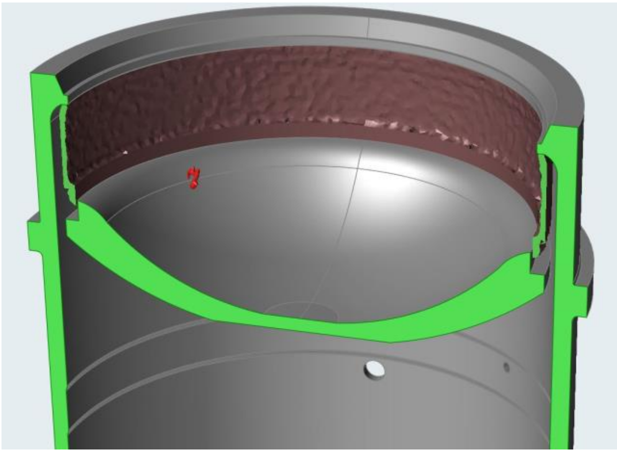

Figure 95 Topology optimization output for the insulator ring

Geometria rezultată se va lua în considerare pentru reconstrucția acesteia și analiza cu elemente finite a geometriei reconstruite în vederea validării.

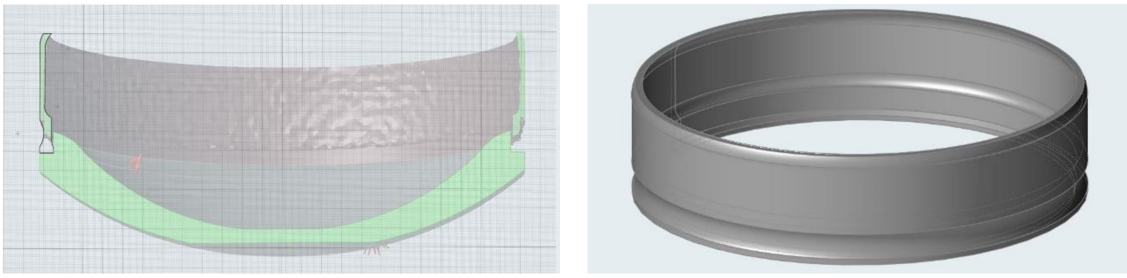

Figure 96 Insulator ring geometry after reconstruction based on the topology optimization results

Figure 97 indicates the stress distribution obtained within the reconstructed geometries of the dome and insulation ring. The maximum stress level within the insulator ring is reduced to 550 MPa while within the dome is below 200 MPa.

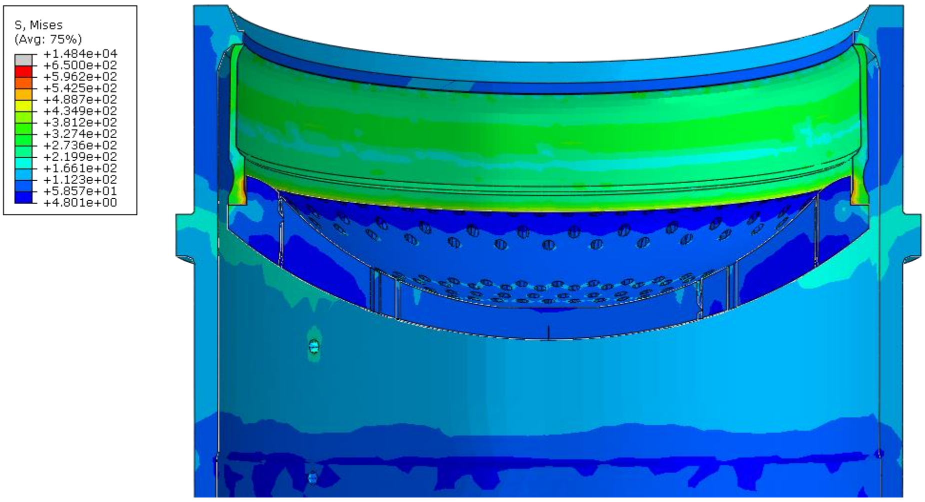

Figure 97 von Misses stress distribution within dome and insulation ring

Related to the resulted displacement, an improvement compared to the initial state can be noticed from Figure 98, where the maximum displacement reached is 1,17 mm.

A stiffer and less tensioned construction is therefore obtained compared to the initial geometry (Figure 84) while the volume of the dome is reduced by approx. 45 %; the volume of the insulation ring remains approximately the same, compared to the reference model, but the stress level is significantly reduced through the new geometry.

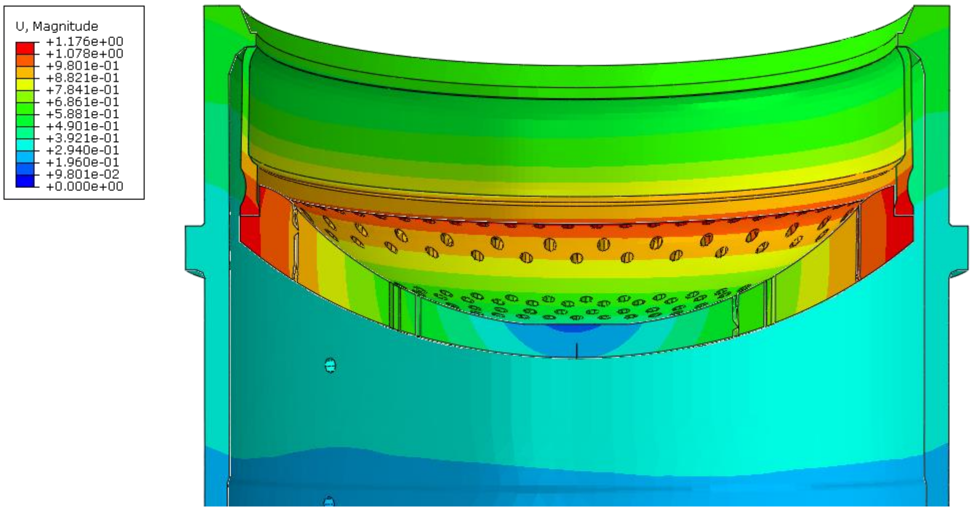

Figure 98 Displacements results

3.4 Multi-objective optimization

3.4.1 Description of the topic

Multi-objective optimization problems are those in which the aim is to achieve at least two objectives simultaneously, regardless of the number of input variables. For example, let be a system with one input variable x and two outputs f_1 and f_2 (Figure 99), functions described by equations (26) and (27) and shown graphically in Figure 100 for $x \in [2,7]$.

Figure 99

$$f_1(x) = 2x^2 - 21x + 75 \tag{26}$$

$$f_2(x) = 2x^2 - 14x + 40 \tag{27}$$

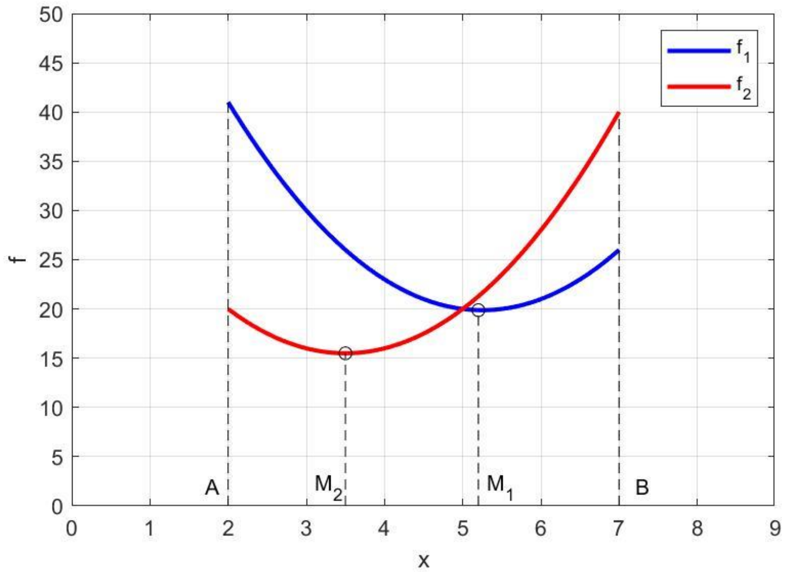

Figure 100 Graphical representation of objective functions (Equations and (26) and (27))

Figure 100 shows that the minimum of function f_1 is obtained when x=5.2 and has the value 19.88 (M1) and the minimum of function f_2 is obtained when x=3.5 and has the value 15.5 (M2).

In the situation where it is desired to minimize both functions f_1 and f_2 simultaneously, the problem becomes a multi-objective optimization one and the obtained result is described by a set of possible solutions - i.e. feasible solutions (Figure 101- blue line).

While in a single-objective problem the superiority of a solution over other solutions is determined directly by comparing the objective function values, in a multi-objective optimization problem the dominance ratio between solutions in the feasible domain is sought. Thus, the solutions can be dominated or dominant. Dominant solutions are those ones that are not dominated by any other solution in the feasible domain, form the set of Pareto solutions, or the Pareto front (Figure 101). The Pareto front, described in detail in Figure 102, is composed of those solutions that correspond to the values contained in the interval [M2, M1] in Figure 100.

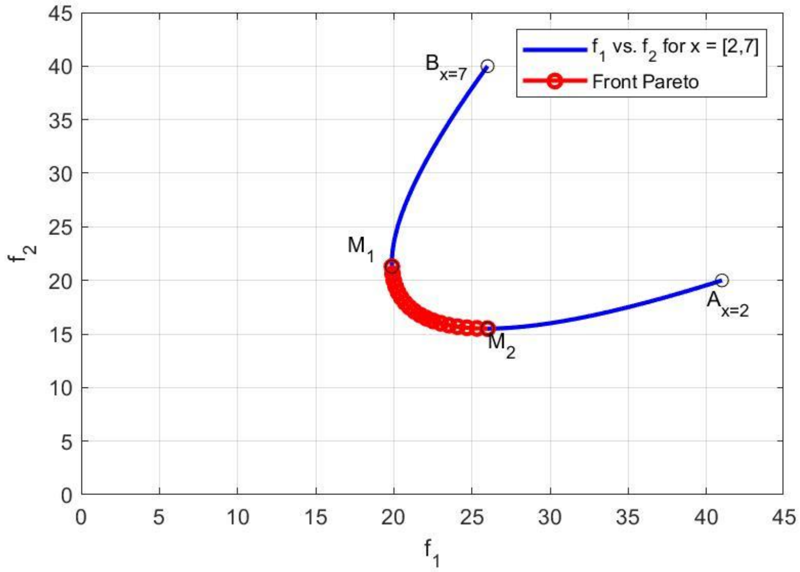

Figure 101 Representation of the Pareto front for the given optimization problem

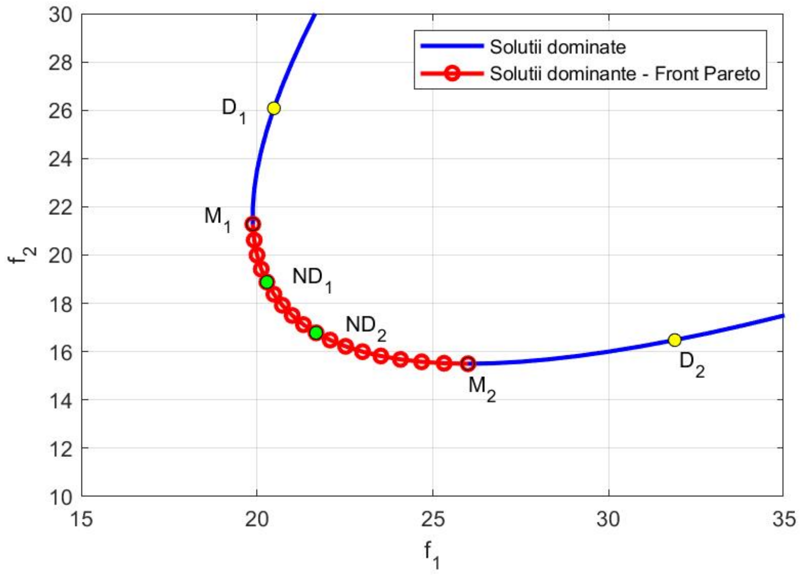

Figure 102 Dominant solutions (Pareto front) vs. dominated solutions

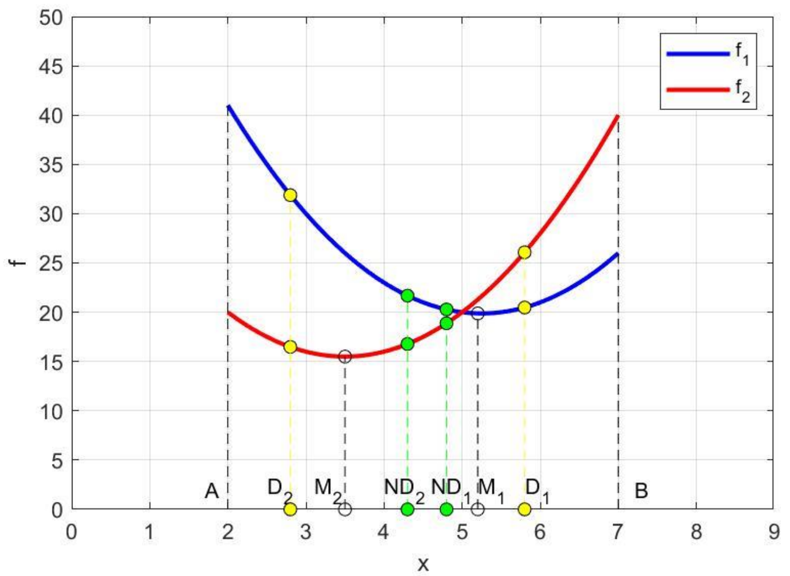

Figure 103 Identifying the values of the input variable for the dominant and dominated solutions

Solutions D1 and D2 are dominated solutions, meaning that there are other solutions that dominate them, that offer better solutions for both objective functions f_1 and f_2 ; these type of solutions correspond to values of the variable x outside the interval [M2, M1] , as indicated in

Figure 102 and Figure 103. Examples of dominant solutions, which are part of the Pareto front, are ND1 and ND2, which correspond to values of the variable *x* from within the interval [M2, M1].

Therefore, a multi-objective optimization problem results in a set of optimal solutions forming the Pareto set; choosing one of the solutions requires a negotiation between the objective functions by using specific selection methods.

3.4.2 Achievements

I. *Multi-objective optimization of vehicle bodies made of FRP sandwich structures (Velea et al., 2014)*

The article entitled *Multi-objective optimization of vehicle bodies made of FRP sandwich structures* (Velea et al., 2014) describes the contribution of the first author within the project entitled *OptFRPBody (Optimization of Body in FRP-Composite for small Electric Vehicle)*, at KTH – Royal Institute of Technology, Department of Aeronautical and Vehicle Engineering. The total budget of the project was 9400 kSEK (c:a 1M€) and the funding was supported by Mistra Innovation – The foundation for Strategic Environmental Research, Sweden.

In this project, an optimization methodology was developed and applied on a FRP sandwich body of an electric vehicle – ZBee, where single-objective and multi-objective optimization studies are performed stepwise using a commercially available software package (Altair Hyperworks). The single-objective optimization allows the identification of the load paths within the composite body, according to the loading conditions previously defined. Within the multi-objective optimization, the optimum thickness and distribution for each of the layers that form the composite body are searched within the design space to obtain the best performance with respect to weight, material cost, global and local stiffness. Strength requirements are also considered as constraints within the optimization. A conflict situation appears when several objectives are considered within the optimization, meaning that an increased performance in one objective may often lead to a decreased performance for the others. Therefore, a trade-off between objectives is needed. The interpretation of results is partially made by using trade-off plots, the so-called Pareto frontiers. A method for the overall selection of the most beneficial solutions is proposed and applied in order to choose between the best obtained solutions according to the importance of the objectives.

The ZBee concept represents the materialized vision of the Swedish company – Clean Motion AB – regarding energy efficient electric vehicles. This urban vehicle, classified as scooter according to EU regulations, has been designed for short distance transportation of up to three people and smaller goods. Figure 104 shows the 2nd generation of the ZBee vehicle. The body in white was entirely made of FRP composites. Certain sections within the body were made of FRP sandwich structure for an increased bending stiffness, having PVC foams and polymer honeycombs as cores. The composite body was made of 9 parts which were adhesively bonded together to form a whole.

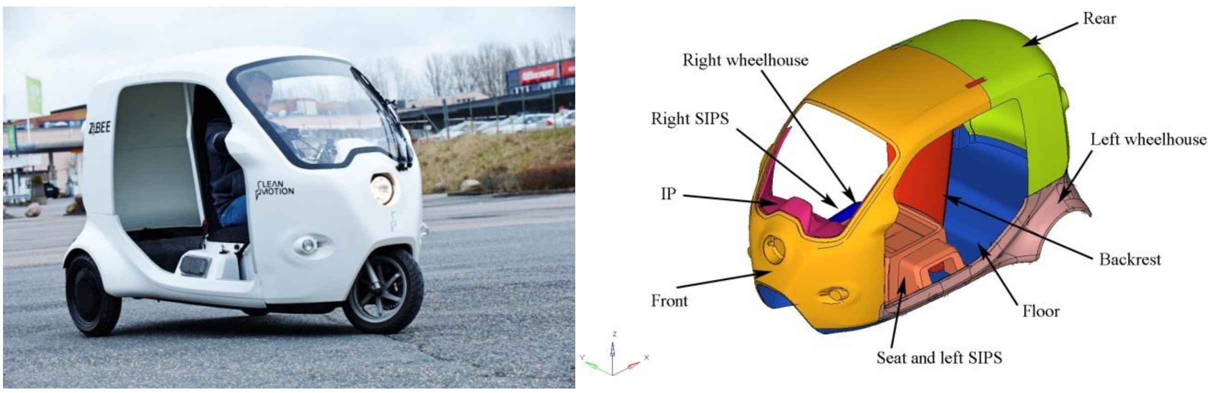

Figure 104 The 2nd generation of ZBee vehicle

A new generation of the ZBee – the 3rd generation –, Figure 105, aims at an increased performance in terms of weight, material costs, local and global stiffness behavior compared to the 2nd generation.

Space for even more increased performance exists because overall properties of FRP composites may be tailored to satisfy specific design requirements by changing the values of the constituents' specific parameters (Walker & Smith, 2003). This goal can be attained if appropriate advanced optimization tools are used.

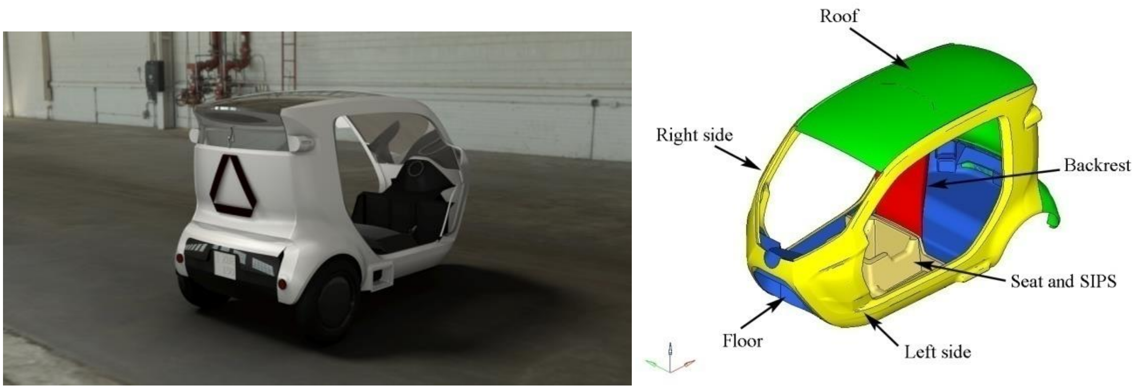

Figure 105 The 3rd generation of ZBee vehicle – new composite body design

An optimization problem is most often formulated when trying to improve the vehicles' performance by weight reduction. An optimal solution of the objective function (e.g. mass) is searched within a design space defined by the upper and lower limits of the design variables (e.g. materials' properties) and by certain imposed constraints (e.g. required stiffness, strength etc.) (Harte et al., 2004).

However, lowering the weight of a vehicle will most often imply a reduction of other performance criteria such as the stiffness and strength properties, material cost or the safety performance. Therefore, there are cases where several objectives need to be defined and considered within the optimization procedure in which case a conflict situation appears between objectives, meaning that an increased performance in one objective leads to a decreased performance for the others (M. F. Ashby, 2000). Several complex techniques and algorithms have been proposed for solving such multi-objective optimization problems (Badalló et al., 2013; R. T. Marler & Arora, 2004; K. Wang et al., 2002)

The weighted sum approach has been used as an attempt to simplify the problem complexity of finding solutions within multi-objective optimization problems, where all the objectives' functions are summed into a single objective function, giving weight penalties for each of them (Walker & Smith, 2003). Then, a solution may be obtained by running one of the many existing single-objective optimization algorithms. The main drawback regarding the weighted sum method is the quantification of weight penalties because the results are strongly dependent on them (Kaufmann et al., 2010), although methods for dealing with this issue have been studied and proposed (R. Marler & Arora, 2010).

Therefore, to obtain a large spectrum of solutions, dedicated multi-objective optimization algorithms remain here of interest (Almeida & Awruch, 2009; D. S. Lee et al., 2012). One of the most spread algorithms within the current available commercial FE packages is the so-called MOGA (Multi-objective Optimization Genetic Algorithm). Instead of providing one single solution, MOGA produces a set of solutions by searching within the design space for a set of Pareto optimal solutions (Konak et al., 2006). The interpretation of results in the case of a multi-objective optimization study is partially made with the help of the trade-off curves, the so-called Pareto frontiers (Deb, 2011). The obtained Pareto frontiers only indicate the set of solutions that gives the best compromise between objectives, but there is a further need for choosing one single solution from the set. This can be done either by intuition or by reformulating the objectives as constraints, except one of them, or by using a composite objective function (M. F. Ashby, 2000).

All the analyses and optimization studies have been performed within the Hyperworks 11 software package. Hypermesh facilities were used to simplify the geometry, to generate the mesh, to define material properties and to assign load cases. Optistruct solver was used for FE analyses and single-objective optimization studies. Hyperstudy and RADIOSS solver were used for multi-objective optimization studies.

The FE mesh is generated on the outer surface of the body parts. The target finite element size was set to 10 mm. Quad and triangular shell elements were used to realize an initial automated mesh of the body parts. The generated finite elements have been checked and refined where needed, according to the HyperMesh quality indexes default values (Altair, 2014). The resulted mesh has 688638 degrees of freedom, Figure 106. The connection between body parts (i.e. the adhesive) has been modelled using rigid elements to simplify the model.

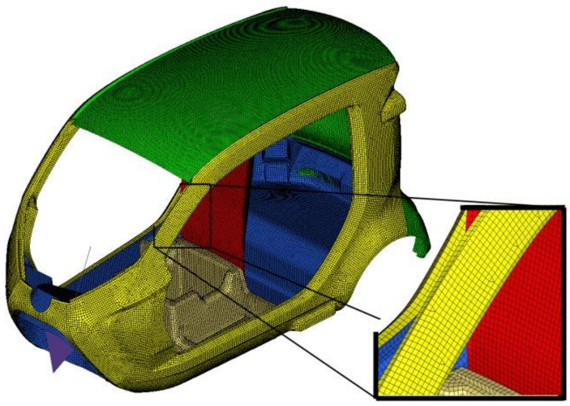

Figure 106 Meshed body

The composite structures the body parts are made of are modelled as laminates; each laminate being composed by several plies (layers). The material properties were thus defined individually for each of the layers within the software. Table 4 shows the types of layers that were used within the body structure of the ZBee-Generation 3 and their corresponding material characteristics. The acronyms GF-weave and GF-csm represent a bi-directional weave and glass fibre chopped strands mats respectively. SORIC represents a polymer honeycomb core material.

Table 4 The materials properties used within the optimization studies

Material Type	Material characteristics					
	E_1=E_2 [MPa]	G_{12} [MPa]	ρ [Kg/m^3]	X_t=X_c [MPa]	Y_t=Y_c [MPa]	S [MPa]
GF-weave	16740	2237	1704	241	241	7
GF-csm	8462	1712	1432	129	129	9
PUR foam	55	21	150	1.8	1.8	1.18
PVC foam	130	35	100	2	2	1.6
SORIC	800	35	1160	4	4	3
Gelcoat	3800	1387	1200	-	-	-

Within the analysis and optimization of the ZBee composite body there have been considered 6 loading conditions. The corresponding loads and constraints are illustrated in Figure 2.2.

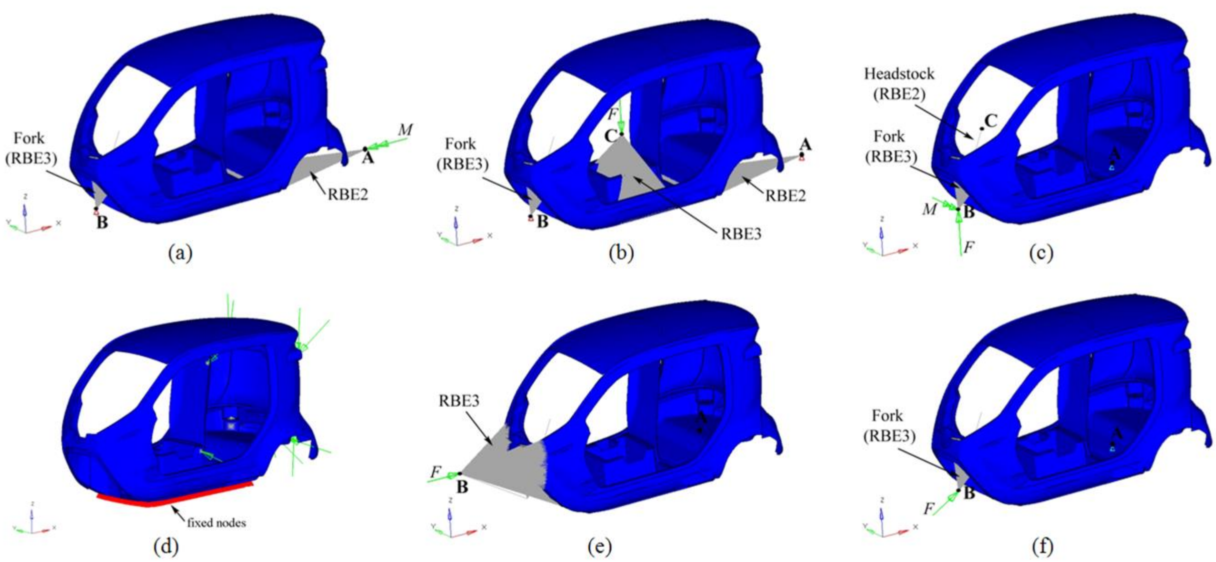

Figure 107 The applied loads and constraints

(a) – Global torsion

This load case has the purpose of evaluating the torsion stiffness of the whole composite body. Figure 107(a) shows the considered boundary conditions, where node B has all the degrees of freedom retained. The torsion stiffness K_t is thus determined using Equation (28), where M_{xA} is the moment applied along X-axis at point A and θ_{xA} represents the rotation measured around X-axis at point A.

$$K_t = \frac{M_{x_A}}{\theta_{x_A}} \quad \left[\frac{\mathrm{Nm}}{\mathrm{deg}}\right] \tag{28}$$

(b) – Global bending

The bending stiffness K_b of the composite body is determined using Equation (29), where F_{zC} is the force applied along Z-axis at point C and δ_{zC} represents the displacement measured along Z-axis at point C. The node B has all degrees of freedom retained while node A is allowed to slide along X-direction, Figure 107(b).

$$K_t = \frac{M_{x_A}}{\theta_{x_A}} \quad \left[\frac{\mathrm{Nm}}{\mathrm{deg}}\right] \tag{29}$$

(c) – Front wheel brake

This load case has been introduced to evaluate the local stiffness of the composite body around the front wheel, Figure 107(c). It is assumed that the vehicle is travelling on a downhill gradient of 15° and only the front wheel is braking (worst case). Taking into consideration the legal requirements that the vehicle needs to stop with an average deceleration of 2.7 m/s, a braking force F and a braking moment M are determined and both are applied on point B (center of the front wheel); the displacement of point C (the headstock top point) is then determined using Equation (30), where δ_x, δ_y and δ_z represent the displacements of point C evaluated within the analyses along the three orthogonal axes).

$$\delta = \sqrt{{\delta_x}^2 + {\delta_y}^2 + {\delta_z}^2} \ \ [mm] \tag{30}$$

(d) – Belt point forces

Specific local stiffness at belt points is also required. Within this load case, static forces are applied at belt points and their displacements are evaluated and used as constraints within the optimization study. The degrees of freedom are restrained for all the bottom nodes, Figure 107(d).

(e) – Front impact

For the homologation of the vehicle, several safety requirements need to be fulfilled and therefore equivalent load scenarios also need to be included within the simulations. Dynamic non-linear FE analyses are usually considered for investigating this type of crash scenarios (Duddeck, 2008) but these imply a high computational time, especially in the case of a multi-objective optimization. For this reason, an equivalent static load case is here approximated, Figure 107(e), where a force F is applied on the depended node B and distributed within interpolation constraint elements – RBE3 (Altair, 2014) on an estimated impact area from the composite body. The magnitude of the force F equals M·10g, where M is the full vehicle mass and g is the gravitational acceleration. The displacement of point B is then evaluated and used within the optimization studies as a constraint or objective in the form of Equation (30).

As in the case of the Front wheel brake load case, the inertia relief is used here too for obtaining the load equilibrium of the model. The degrees of freedom of node A, Figure 107(e), are constrained to restrain the rigid body motion.

Although this is a roughly simplified way to simulate a front impact scenario, it is anyway expected that the applied static force will unveil the load paths by increasing the thickness of specific layers as required to satisfy the displacement constraint of point B. Other authors have used the same approach for single-objective topology optimization (Cavazzuti et al., 2011).

(f) – Curb strike

This load case allows the effect of the load distributed within the composite body to be considered when the front wheel hits a curb. The force F, Figure 107(f), is calculated as M·3g, where M is the full vehicle mass and g is the gravitational acceleration. It is assumed that the curb has a height of 100mm, and the wheel radius is 230mm. The force is then applied in the center of the wheel represented by the point B, Figure 2.2(f), at an angle of 34° from Ox axis, within the xOy plane, and it is transferred to the composite body by the interpolation constraint elements – RBE3 (Altair, 2014), that represent the fork. The displacement of point B is evaluated and used within the optimization studies as a constraint or objective in the form of Equation (30).

The proposed optimization methodology consists of three main steps, Figure 108.

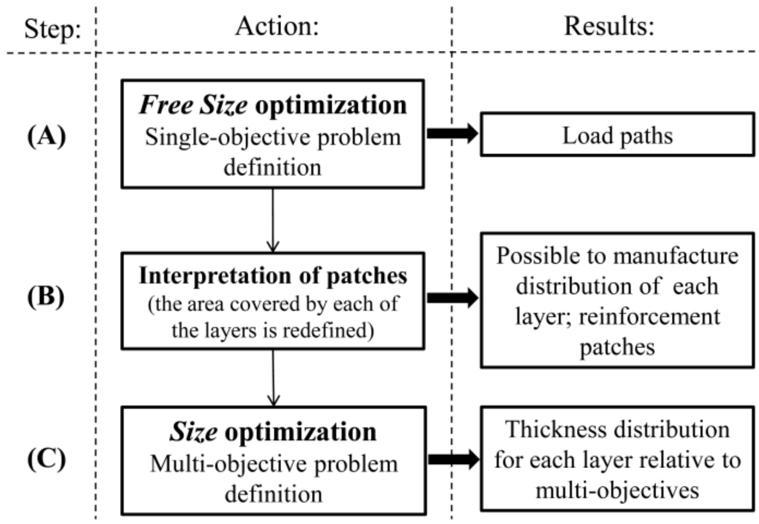

Figure 108 Optimization methodology applied on the composite body

First, a single-objective free size optimization is performed on the composite body modelled. Within the second step, the area covered by each layer is redefined according to the obtained distribution of thicknesses from the free size optimization results. The last step consists of performing a multi-objective size optimization to the redefined patches.

A detailed description of these three steps is given further on.

When referring to composite laminates, the mathematical formulation of the single-objective *free size* optimisation problem may be described as it follows (adapted from (Zhou et al., 2009)):

Minimize $f(x) = f(x_{11}, \dots, x_{ij})$

Subject to $x_{ij}^L \le x_{ij} \le x_{ij}^U, \quad i = 1, \dots, Nl; j = 1, \dots, Ne$

$g_k(x) - g_k^U \le 0, \quad k = 1, \dots, m;$

where:

- $f(x)$ is the objective function
- x_{ij} represents the thickness of the i^{th} layer of the j^{th} finite element
- $g_k(x)$ and g_k^U are the k^{th} constraint response and its upper bound
- Nl and Ne represent the number of layers and the number of elements
- m is the number of constraints

The goal at this stage is to identify the load paths through the composite body for the given loading conditions. The initial structure of the parts is made of six layers all over the body, according to the section illustrated in Figure 109.

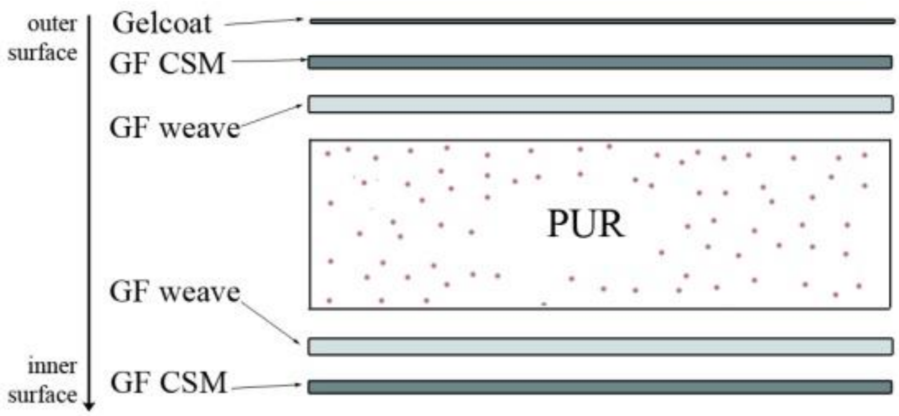

Figure 109 Section within the composite body structure

The initial thicknesses of the GF-weave and GF-csm layers, Table 5, have been predicted using Equation (31).

$$h = \frac{W_f}{\rho_f} + \frac{W_m}{\rho_m}, \tag{31}$$

where:

- W_f and W_m represent the weight of the fibres and of the matrix per unit area; W_f is given in Table 5.
  W_m is calculated for each as $W_m = (W_f/w_f) - W_f$, where $w_f = \rho_f v_f / (\rho_f v_f + \rho_m v_m)$, v_f represents the fibre volume fraction and it is equal to 0.4 for GF-weave and 0.2 for GF-csm. The matrix volume fraction v_m is equal to $1 - v_f$.
- ρ_f and ρ_m are the densities of the glass fibres and of the polyester matrix, and they are equal to 2520 Kg/m^3 and 1160 Kg/m^3 respectively, (Åström, 2002).

Table 5 Initial thickness and layers' distribution within the composite body

Layer Type	Placement	W_f [g/m^2]	Initial thickness [mm]
Gelcoat	complete layer	-	0.600
outer GF-csm	complete layer	300	0.595
outer GF-weave	complete layer	600	0.595
PUR	complete layer	-	30
inner GF-weave	complete layer	600	0.595
inner GF-csm	complete layer	300	0.595

Within the *free size* optimisation, the thickness value of the layers shown in Table 5 is allowed to vary freely within a predefined interval for each finite element. These thicknesses represent the design variables, and their upper and lower limits are shown in Table 6. The thickness of the Gelcoat layer is kept constant.

Table 6 Design variables within the *free size* optimisation step

Layer	**Thickness [mm]**	
	lower limit	**upper limit**
outer GF-csm	0.2	1.2
outer GF-weave	0	1.2
PUR	0	30
inner GF-weave	0	1.2
inner GF-csm	0.2	1.2

The imposed design constraints within the *free size* optimisation may be interpreted as performance targets that should be met, for each of the considered load cases. The applied constraints are described in Table 7.

Table 7 Constraints applied within the free size optimisation

Load case	**Constraint**	**Description**
Torsion stiffness	$K_{t3} \geq 2K_{t2}$	Torsion stiffness of the 3rd generation, Equation (28), should be at least equal to two times the one of the 2nd generation.
Bending stiffness	$K_{b3} \geq 2K_{b2}$	Bending stiffness of the 3rd generation, Equation (29), should be at least equal to two times the one of the 2nd generation.
Front wheel brake	$\delta_{C3} \leq \delta_{C2}$	Displacement of point C, Figure 107 (c) of the 3rd generation should be less than or equal to the one of the 2nd generation.
Belt points stiffness	$\delta_{belt\_points\_3} \leq \delta_{belt\_points\_2}$	Displacements of belt points, Figure 107(d) on the 3rd generation should be less than or equal to the ones of the 2nd generation.
Front impact	$\delta_{B3} \leq \delta_{B2}$	Displacement of point B, Figure 107(e) of the 3rd generation should be less than or equal to the one of the 2nd generation.
Curb strike	$\delta_{B3} \leq \delta_{B2}$	Displacement of point B, Figure 107(f) of the 3rd generation should be less than or equal to the one of the 2nd generation.

The values for the objective functions K_{t3} and K_{b3} are constrained to be at least equal to two times the corresponding values for the 2nd generation to force the PUR layer to grow in a more realistic shape instead of a scattered distribution.

The single objective is to minimize the mass of the composite body by varying the defined design variables, Table 7, while satisfying the imposed design constraints, Table 7.

The contour plot representing the thickness distribution of the PUR layer, Figure 110, shows a thickness distribution up to 60 mm around the bucket region, although the upper limit of the corresponding design variable has been set to 30 mm, Table 6. This happens because a T-joint exists around the bucket and therefore the model implies two layers of PUR foam that are concurring within that region.

A feasible solution has been reached within this optimisation step, where the mass has been decreased by 29.9 % compared to the 2nd generation, at the same time by satisfying all the constraints defined in Table 7.

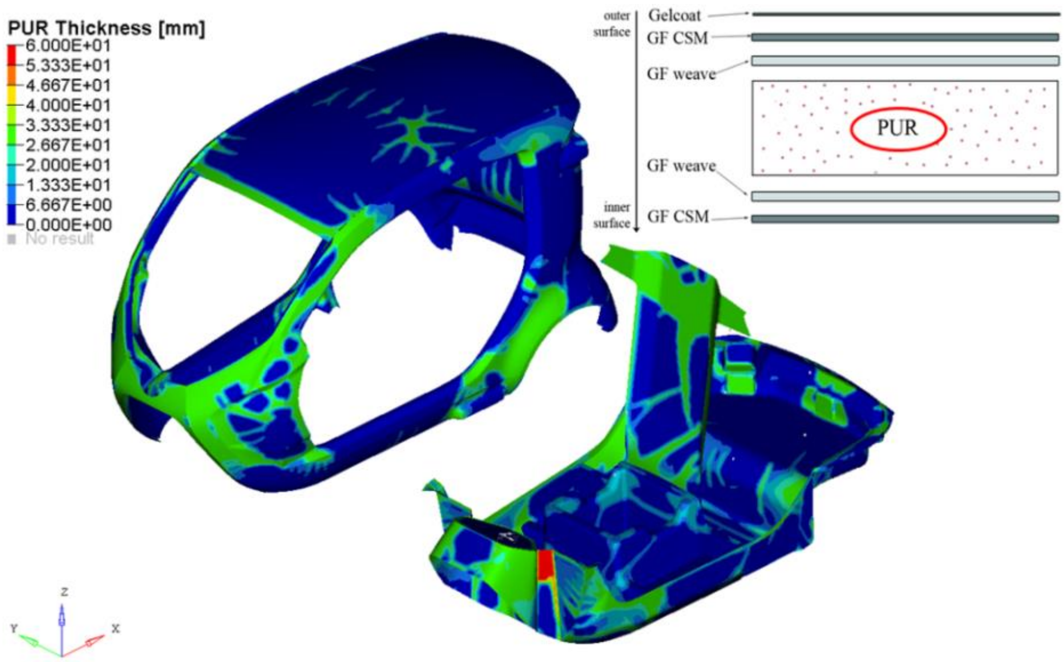

Figure 110 Thickness distribution of the PUR foam layer

Although a theoretical feasible solution was obtained within the free-size optimization, the resulting thickness distribution of each layer within the composite body is hard to reproduce, especially the layer that represents the core, Figure 3.3. For this reason, the area covered by each layer is interpreted following the free size optimization results and redefined to reach a shape that is possible to manufacture. This step requires the assistance of experts on manufacturing technologies of composites.

Figure 111 shows the distribution of the PUR foam within the composite body (gray areas) as it was interpreted based on the information provided by the free size optimization results, Figure 110, and by the recommendations coming from manufacturing experts. One of the benefits of using PUR as a core within the composite body is that it may be extruded by using molds into complex shapes that can better follow the load paths indicated by the analysis.

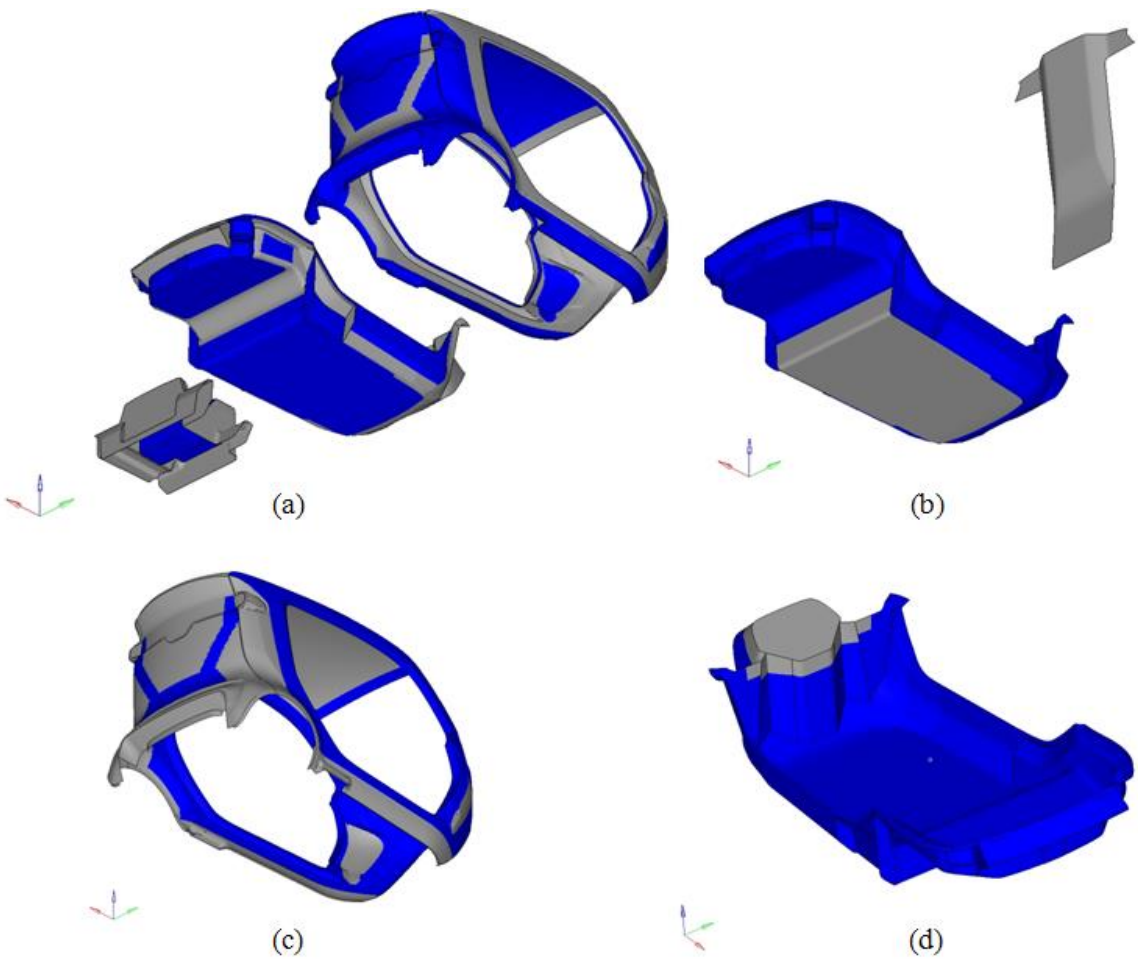

Figure 111 Interpretation of the layers' distribution within the composite body following the free size results: (a) PUR foam; (b) PVC foam; (c) SORIC honeycomb ; (d) GF weave reinforcement.

However, there are regions within the composite body where higher local bending stiffness is required; PVC foam has higher stiffness properties comparing to PUR foam, Table 4, and therefore it may provide a better behaviour. Still, milling the PVC foam into complex shapes may be an expensive process and thus this solution is acceptable only on relatively flat regions within the body. Such areas are shown in Figure 111(b): the backrest and the bottom area of the floor. The backrest part allows the transfer of loads between floor, sides, seat and roof and therefore its contribution to the global behaviour of the body is important. Also, the bottom area of the floor requires higher bending stiffness due to the loads coming from the road within the connection of the wheels to the body, and from the seat and the backrest.

There are regions within the model where no PUR was required following the considered loading conditions, Figure 110. However, to avoid stability issues (Cervellera et al., 2005), a 3 mm SORIC honeycomb (LANTOR, 2011) is required to be placed where no PUR is located - within the roof and the sides, Figure 111(c).

Reinforcement patches consisting of glass fibre weaves have been considered within the floor region where the front wheel fork is connected to composite body, Figure 111(d).

Within a next step, the size optimisation is performed, on the previously identified patches, by considering multiple objectives. In the context of composite laminates, the mathematical description of the multi-objective size optimisation problem may be formulated as it follows:

Minimize $F(x_{ij}) = [f_1(x_{ij}),\ f_2(x_{ij}), \dots, f_n(x_{ij})\ ]^T$

Subject to $x_{ij}^L \leq x_{ij} \leq x_{ij}^U, \quad i = 1, \dots, Nl; j = 1, \dots, Ns$

$g_k(x) - g_k^U \leq 0, \quad k = 1, \dots, m;$

where:

- n is the number of objective functions;
- x_{ij} represents a vector of design variables; it may be formed by thicknesses and fibre orientation angles for each of the i^{th} layer placed within the j^{th} set of elements
- $g_k(x)$ and g_k^U are the k^{th} constraint response and its upper bound
- Nl and Ns represent the number of layers and the number of the elements sets the composite body is divided in
- m is the number of constraints

A multi-objective genetic algorithm (MOGA) that is implemented in HyperStudy is used to perform the *size* optimization by considering 7 objective functions (Table 8).

Table 8 Objective functions defined within the size optimisation

Objective	Function	Description
minimize	Mass of the composite body	Evaluated within the simulation
minimize	Material Cost	Defined by Equation (32)
maximize	Torsion Stiffness	Defined by Equation (28)
maximize	Bending Stiffness	Defined by Equation (29)
minimize	Headstock displacement	Defined by Equation (30)
minimize	Front impact penetration	Defined by Equation (31)
minimize	Front wheel centre displacement	Defined by Equation (32)

The objective function representing the material cost is modelled according to Equation (32) and considering the assumptions made in

Table 9.

$$C = \sum_{i=1}^{n}\sum_{j=1}^{m}\left(C_{kg} \times A_{ij} \times \rho_{ij} \times T_{ij}\right) \tag{32}$$

where:

- n – the number of body parts
- m – the number of layers within body part
- C_{kg} – material cost per Kg
- A_{ij} – area covered by *j* layer within *i* part
- ρ_{ij} – material density of *j* layer within *i* part
- T_{ij} – thickness of *j* layer within *i* part

Table 9 Assumptions regarding the costs per Kg of the materials used within the composite body

Material	**Cost per Kg [SEK/Kg]**
PVC	500
PUR	200
GF-weave-poly	28
GF-csm	20
SORIC	100
Gelcoat	15

Table 10 Design variables within the *size* optimisation step

Layer	**Placement**	**Thickness [mm]**		
		lower limit	**initial value**	**upper limit**
outer GF-csm	complete layer	0.2	0.595	1.2
outer GF-weave - reinforcement	see Figure 111 (d)	0	2.38	2.975
outer GF-weave	complete layer	0.2	0.595	1.2
PUR	see Figure 111(a)	0	30	40
PVC	see Figure 111(b)	0	15	20
inner GF-weave	complete layer	0.2	0.595	1.2
inner GF-weave - reinforcement	see Figure 111 (d)	0	2.38	2.975
inner GF-csm	complete layer	0.2	0.595	1.2

The considered design variables represent the thicknesses of the layers redefined in step B (interpretation of patches) and they are shown in Table 10. Because the layers that form the composite laminates are considered to have equal in-plane properties, Table 4, the fibre orientation angle is not included in the optimisation.

According to the defined sections within the body and by considering the number of layers, Table 10, it resulted a total number of 42 variables.

Three constraints were considered within this optimisation step, Table 11.

Table 11 Constraints applied within the multi-objective optimisation

Load case	Constraint	Description
Torsion stiffness	$K_{t3} \geq 0.5K_{t2}$	Torsion stiffness of the 3rd generation, Equation (28), should be at least equal to half of the one of the 2nd generation.
Bending stiffness	$K_{b3} \geq 0.5K_{b2}$	Bending stiffness of the 3rd generation, Equation (29), should be at least equal to half of the one of the 2nd generation.
Failure index	$F \leq 0.2$	The failure index F gives the failure condition of the laminate and it is determined using the Tsai-Hill criterion, Equation (33).

The values for the objective functions K_{t3} and K_{b3} are allowed within this optimisation step to decrease up to half the values of the 2nd generation in order to increase the trade-off space with the conflicting objectives, by adding more solutions. Thus, low performance values for K_{t3} and K_{b3} will allow reaching high performance values for the conflicting objectives, as it will be shown further on.

$$F = \frac{\sigma_1^2}{X^2} + \frac{\sigma_1 \sigma_2}{X^2} + \frac{\sigma_2^2}{Y^2} + \frac{{\tau_{12}}^2}{S^2} \tag{33}$$

where:

- σ_1 and σ_2 are the in-plane stresses along longitudinal and transverse direction,
- τ_{12} represents the shear stress,
- X and Y represent the allowable stress in longitudinal and transverse direction,
- S is the allowable shear stress.

A value below 1 for the failure index given by Equation (33) indicates that the stress is within the allowable limits. However, within the optimisation, this failure index is constrained to have a value below or equal to 0.2. This constraint is applied on certain finite elements that were identified as critical within a single run analysis considering the layers shown in Figure 111 and their initial thickness value shown in Table 10.

The obtained values for the objective functions from the multi-objective size optimisation are graphically presented from Figure 112 to Figure 117 and arranged in a tabular form within Table 12, as normalized values to the ones characterizing the 2nd generation of the ZBee; the *Mass* objective is plotted against all the other considered objectives. For the objectives to be minimized, improvements are observed if their normalized value is below 1, while a value above 1 indicates improvements of the objectives to be maximized.

The plots shown, Figure 112 to Figure 117, are also divided into four regions (I - IV) in order to clearly show and classify the performance offered by each of the design solutions. The performance is increased for both objectives if the solution comes from region I or it is decreased for both of the objectives if the solution comes from region IV. Regions II and III contain those solutions where only one of the objectives has an increased performance.

The trade-off between two objectives may be then realized by choosing the solution preferably from those placed within region I, Figure 112 to Figure 117, by identifying the Pareto front (red line), and by making the trade-off between the points that define the Pareto front, in terms of the objective importance. However, when it comes to multiple objectives, difficulties with using the Pareto front arise from the fact that the best compromise between two objectives does not necessarily represent the best one between some other two objectives. Therefore, an overall performance of the objectives is needed, that relates the contribution of each objective when searching the most beneficial overall solution. Such an overall performance function is adapted here from (M. F. Ashby, 2000), where proportion factors are applied to relate the contribution of the objectives, Equation (34).

$$P_S = \frac{\sum_{i=1}^{n} p_i \times \overline{O_i} - \sum_{j=1}^{m} p_j \times \overline{O_j}}{100} \tag{34}$$

where:

- P_s represents the overall performance function;
- $\overline{O_i}$ represents the normalized value of the i^{th} objective to be minimized i=1,...,n;
  $\overline{O_i} = \xi\left(O_{i_{max}} - O_{i_{min}}\right) + O_{i_{min}}, \xi \in [0,1]$
- $\overline{O_j}$ represents the normalized value of the j^{th} objective to be maximized, j=1,...,m;
  $\overline{O_j} = \xi\left(O_{j_{max}} - O_{j_{min}}\right) + O_{j_{min}}, \xi \in [0,1]$
- p_i represents the proportion to which the value of the i^{th} objective contributes to the overall performance function P, in percents;
- p_j represents the proportion to which the value of the j^{th} objective contributes to the overall performance function P, in percents;
- $\sum_{i=1}^{n} p_i + \sum_{j=1}^{m} p_j = 100\%$.

The minimum value of the overall performance function P_s gives the best compromise between the considered objectives while considering the desired value for the proportions p_i and p_j.

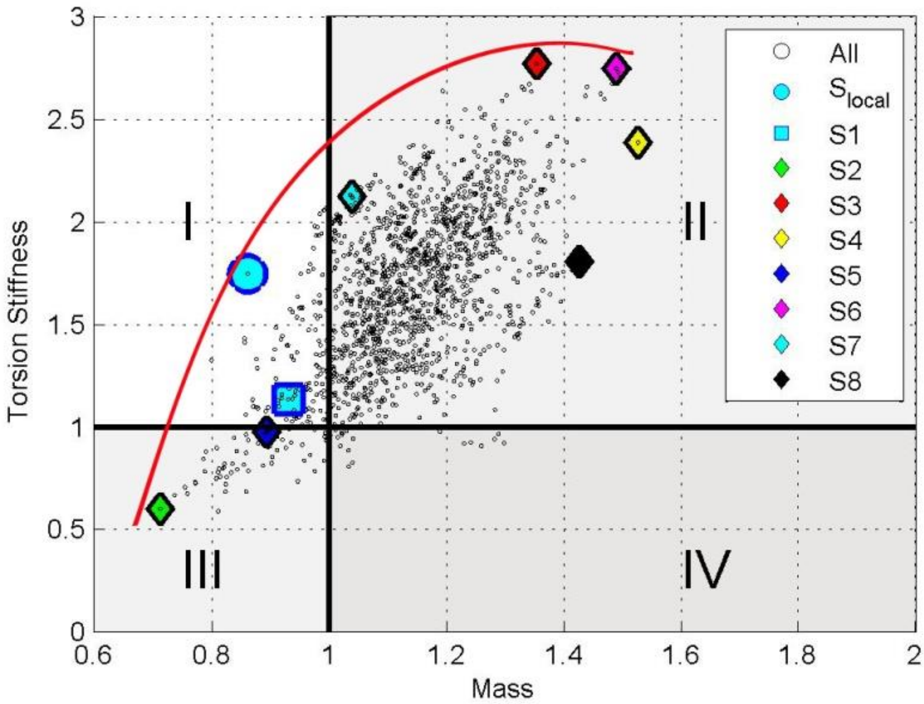

Figure 112 Mass vs. Torsion Stiffness

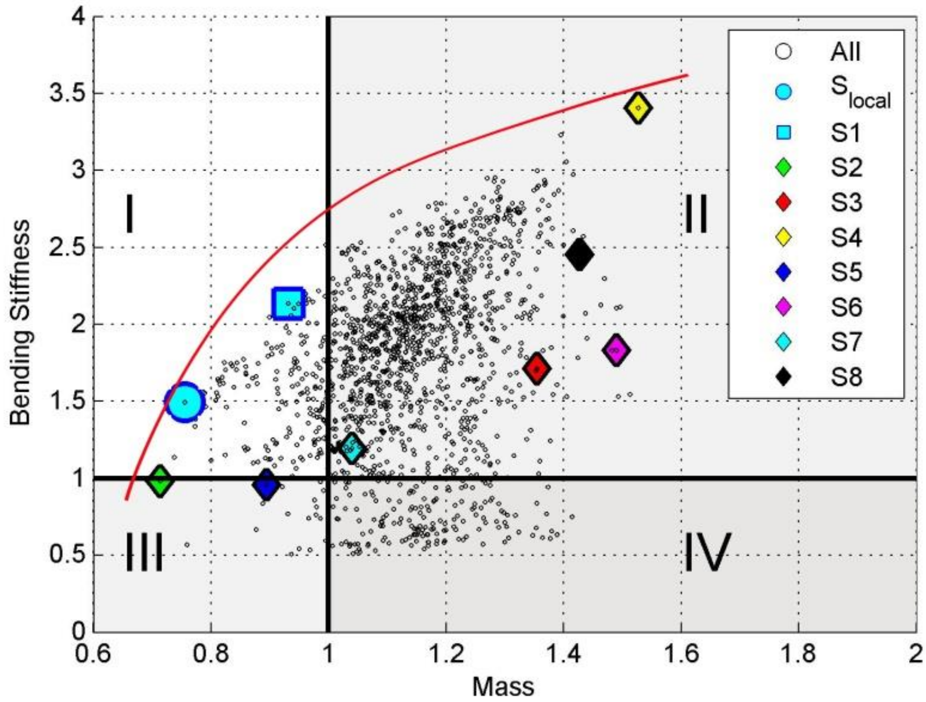

Figure 113 Mass vs. Bending Stiffness

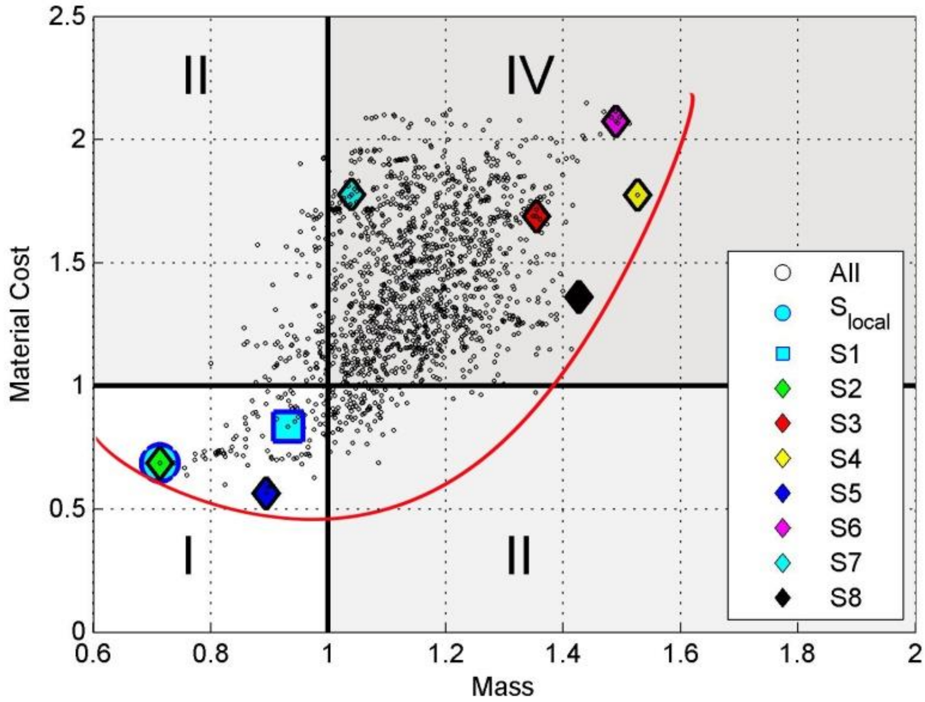

Figure 114 Mass vs. Material Cost

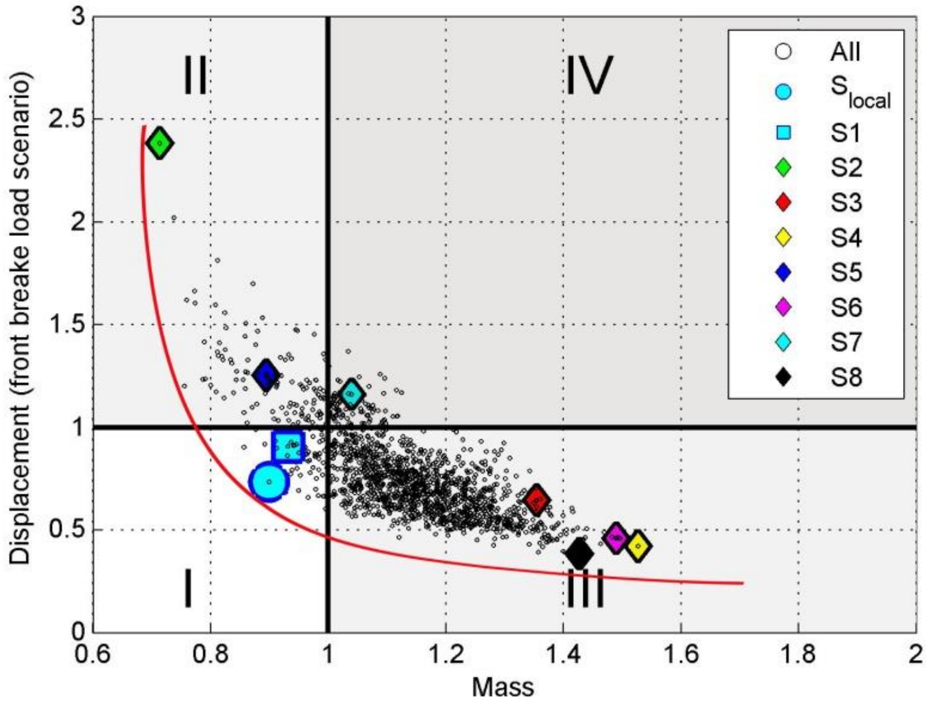

Figure 115 Mass vs. Displacement of point C from Figure 111 (c)

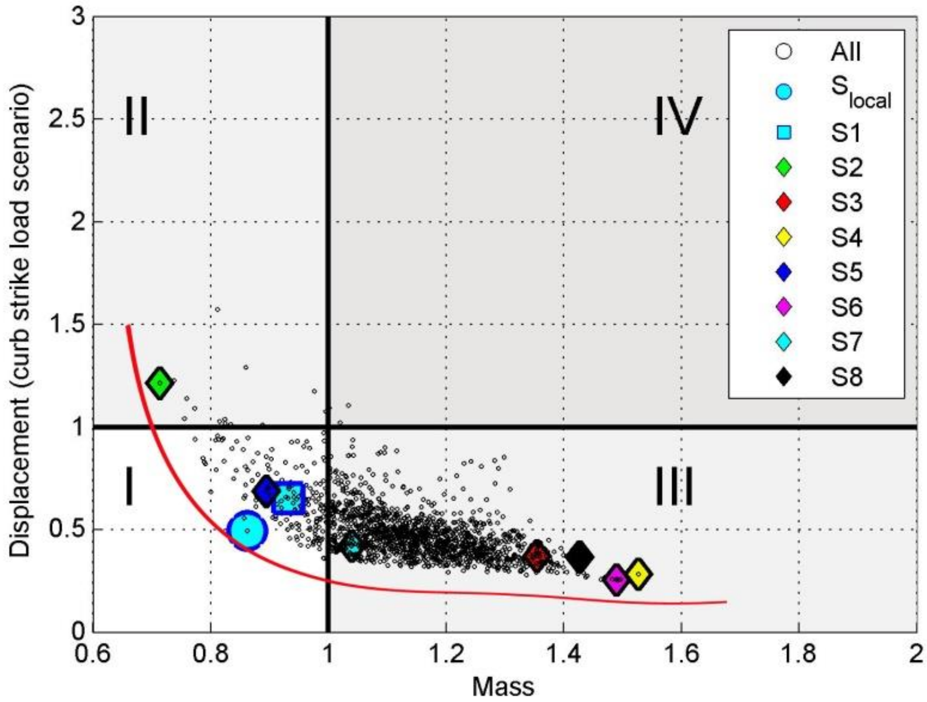

Figure 116 Mass vs. Displacement of point B from Figure 111 (f)

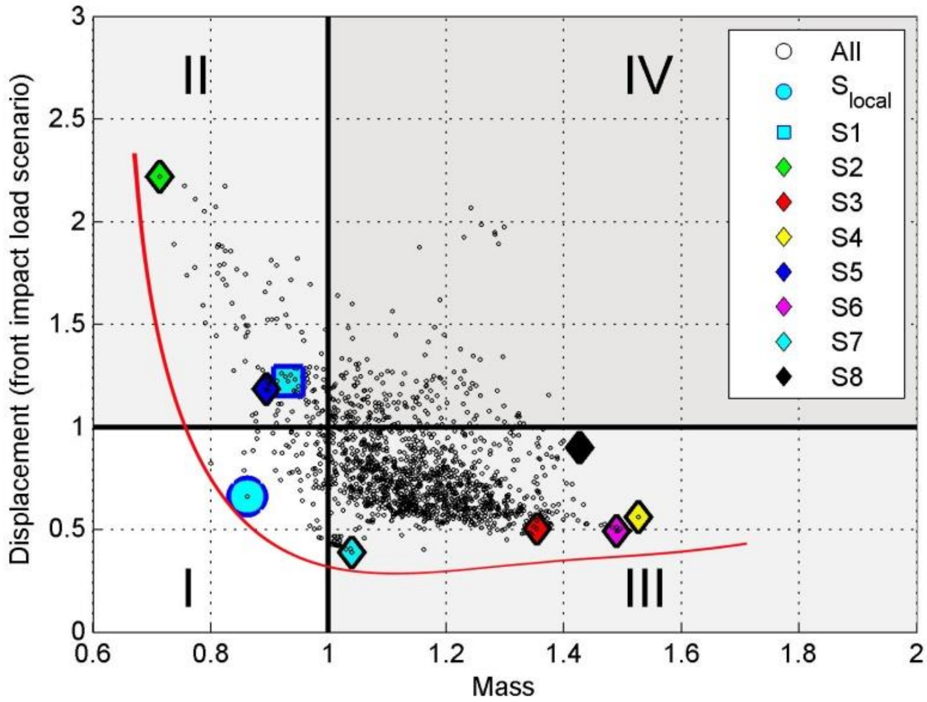

Figure 117 Mass vs. Displacement of point B from Figure 111 (e)

Table 12, correlated with the graphical representations shown within Figure 112 to Figure 117, shows a selection of eight possible solutions obtained by varying the proportion factor *p* in such a way to give different contributions of the objective functions to the obtained design solution. Within Table 12, *Obj* columns show the resulted values of the objective functions, for each of the possible solutions.

The solutions denoted S_{local} which are shown only within Figure 112 to Figure 117, are obtained by defining equal proportion factors (both having a value of 50%) for each of the plotted objective functions, on each graph. This is a simple verification that the selection method used here gives the best compromise between two selected objectives.

Table 12 Responses' values and their corresponding proportion factors for different design solutions

Responses	Selected Solutions															
	S1		S2		S3		S4		S5		S6		S7		S8	
	Obj	p %	Obj	p %	Obj	p %	Obj	p %	Obj	p %	Obj	p %	Obj	p %	Obj	p %
Mass	1.05	25	**0.80**	**94**	1.52	1	1.72	1	1.01	1	1.68	1	1.17	1	1.61	1
Material Cost	0.83	20	0.69	1	1.69	1	1.77	1	**0.56**	**94**	2.07	1	1.78	1	1.36	1
Torsion Stiffness	1.14	-20	0.61	-1	**2.79**	**-94**	2.40	-1	0.98	-1	2.76	1	2.14	1	1.82	1
Bending Stiffness	2.10	-20	0.97	-1	1.68	-1	**3.35**	**-94**	0.94	-1	1.80	1	1.17	1	2.41	1
Displacement (front brake)	0.91	5	2.38	1	0.65	1	0.42	1	1.25	1	0.46	1	1.16	1	**0.38**	**94**
Displacement (front impact)	1.22	5	2.22	1	0.50	1	0.56	1	1.18	1	0.49	1	**0.39**	**94**	0.90	1
Displacement (curb strike)	0.65	5	1.21	1	0.37	1	0.28	1	0.69	1	**0.26**	**94**	0.42	1	0.37	1
Hill Failure Index - *F*	0.03	-	0.03	-	0.02	-	0.04	-	0.02	-	0.03	-	0.02	-	0.04	-
P_s	-0.010		0.0264		-0.9264		-0.9293		0.0109		0.0057		0.0074		0.0051	

Within the solution denoted *S1*, the contribution of the *Mass* objective function has a proportion of 25%, the *Material Cost* 20%, both *Torsion Stiffness* and *Bending Stiffness* objectives represent 20%, while all the remain objectives only 5% each. This case shows a tied trade-off between objectives, where the *Mass* objective has the most important influence on the solution, followed by *Material Cost*, *Torsion Stiffness* and *Bending Stiffness* with equal importance. The solution *S1* gives improvements for all the objective functions except the one corresponding to the front impact load scenario, Figure 117. This can be further on fine-tuned as required by redefining the proportion factors p.

The negative sign on the proportion factor applied to *Torsion Stiffness* and *Bending Stiffness* indicates that these objectives are to be maximized. The minimum value obtained for the overall performance function P_s is in this case equal to -0.010, which allows further on the identification of the solution number that gives the best overall performance, Figure 118.

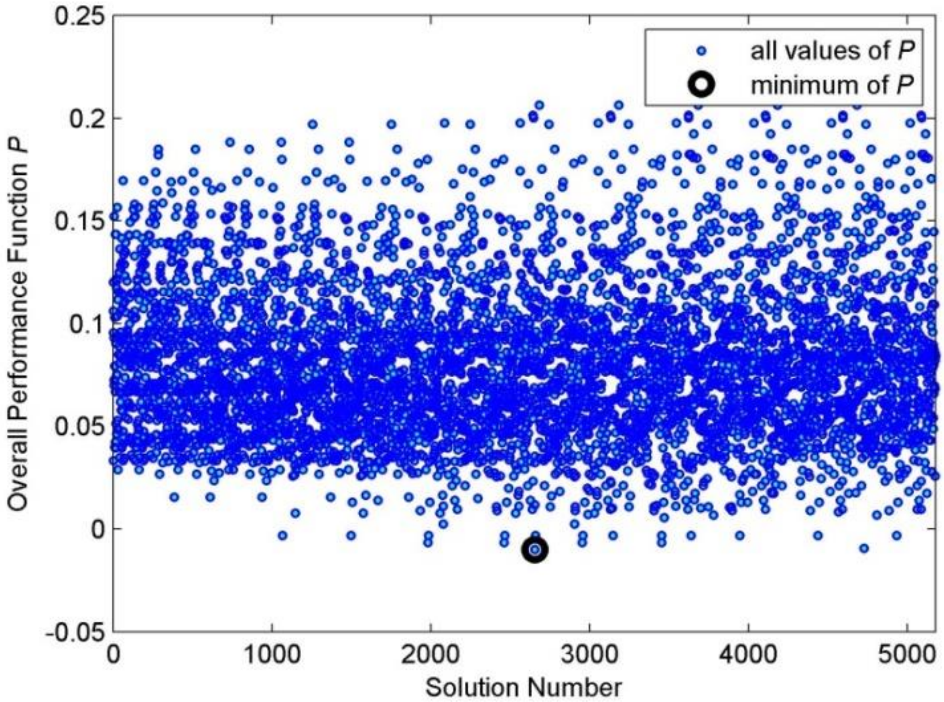

Figure 118 The complete set of solutions vs. Overall performance function Ps obtained within S1

In the same manner, *S2 - S8* represent solutions where different proportion factors are defined, Table 12, to look for extreme dominated solutions and also to demonstrate the utility of the proposed selection method. Thus, *S2* represents *Mass* dominated solution (p = 94%). *S3* and *S4* represent *Torsion Stiffness* dominated solution (p = -94%) and *Bending Stiffness* dominated solution (p = -94%) respectively. As it was previously described, the negative sign indicates that the objective that dominates the solution needs to be maximized. Further on, *S5 – S8* are solutions dominated by objectives which are to be minimized, all of these objectives having the proportion factor p equal to 94%. The Failure Index constraint, Table 11, has been found to be active for seldom design solutions; however, it was not active for the selected solutions *S1- S8*, Table 10.

To produce such kind of overall optimum solutions by using the herein proposed method there is a need to first define the proportion factors *p*. With other words, one should be able to answer the question: what is the proportion with which each objective should contribute to the chosen design solution?

Each design solution corresponds to a distinct set of values for the design variables (layers' thickness); within the optimisation, the design variables vary between the predefined limits.

The obtained values of the design variables are shown within Figure 119 and Figure 120, for each of the selected solutions, *S1 - S8*, for the Backrest and Roof sections. These plots represent sections within the composite parts, showing the thickness value for each of the layers. The symmetric distribution of the layers comes from the fact that symmetry constraints were considered within the optimisation problem definition.

Similar plots may be generated for each part and used for extracting the thickness that must be used for each layer, for all body parts, within the manufacturing process.

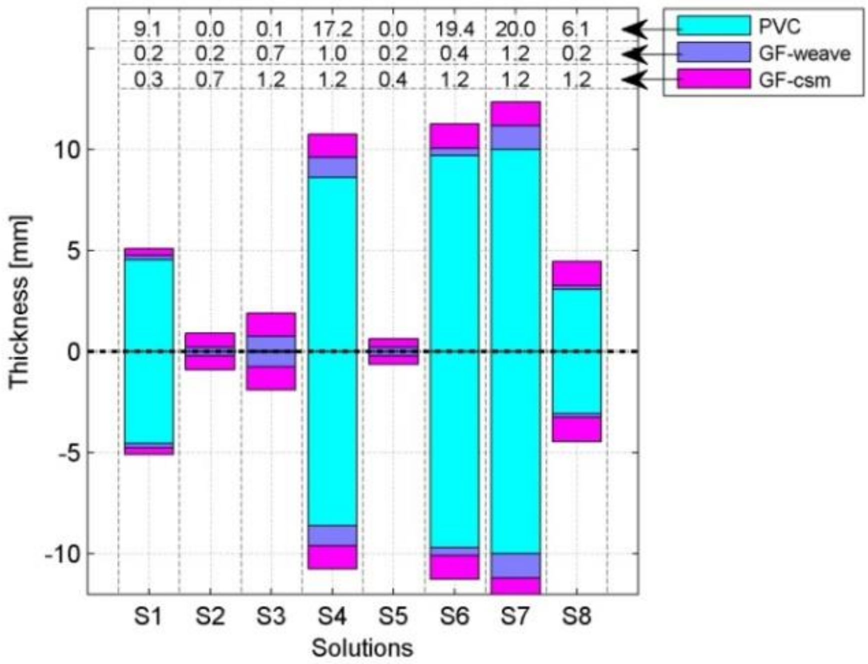

Figure 119 Values of the layers' thicknesses obtained for the Backrest body part, for the selected design solutions

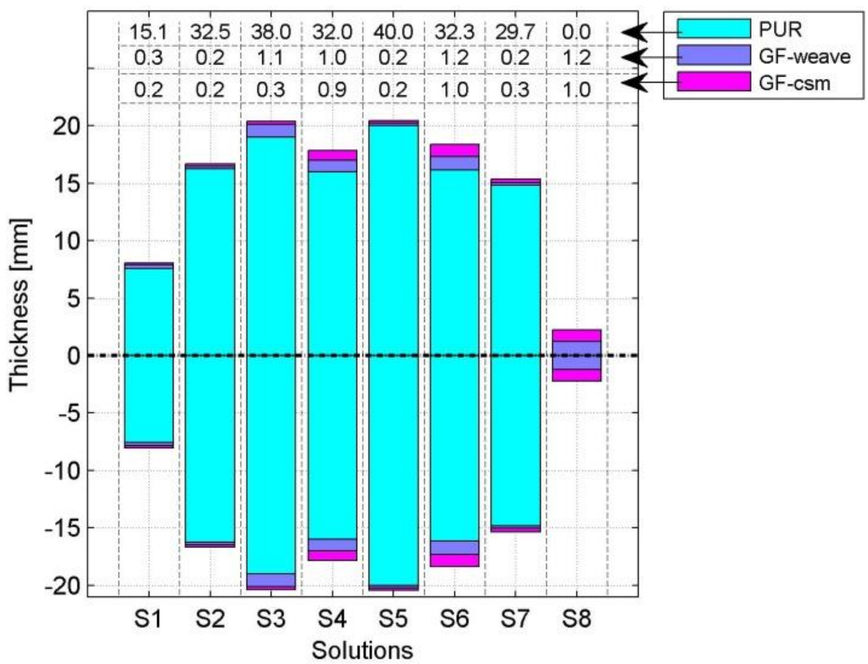

Figure 120 Values of the layers' thicknesses obtained for the Roof body part, for the selected design solutions

II. Thermal expansion of composite laminates (Velea & Lache, 2015)

When connecting composite materials and isotropic materials, their different thermal expansion coefficients may introduce additional stress in the structure. This article shows the way the fiber composite laminates may be designed and optimized to fit the thermal expansion of the pair isotropic material and thus resulting similar thermal deformations in both materials. An optimization model is developed based on the micromechanics theory of composite laminates where the plies angles represent the design variables while the objectives are represented by the thermal expansion coefficients of the laminate.

Composite materials and structures may provide multiple benefits, first with respect to weight. Their mechanical properties may be tailored according to the imposed loading conditions by changing the fiber or matrix, the fiber orientation or the stacking sequence. All these degrees of freedom allow optimizing the structure to obtain the best stiffness and strength to weight ratio (Velea et al., 2014). In addition to the applied mechanical loads, thermal loads may also occur when a system is working within a large interval of temperatures. Especially when metal parts are in contact with the composite parts, care must be taken within the design process due to different thermal behavior of materials. Therefore, one of the problems when joining dissimilar materials is referring to thermal expansion. Connecting materials with different thermal expansion coefficients usually generates additional stress in the structure. If not properly designed, the connection may fail under the combined thermal and mechanical load.

This work presents a design method of the fiber reinforced composite laminates in order to obtain thermal expansion coefficients equal to the one of the metal that the composite part must be in contact with. After presenting the theoretical background a calculation example is given in order exemplify the presented design method.

Having given the fiber and matrix individual properties, the overall properties of the lamina (one single ply) may be determined by using the Rule of Mixture approach (Vinson, 2005). The thermal expansion coefficients of the lamina in local coordinates (1-2), α_1 and α_2 will therefore be determined with Equation (35) for 1-direction and with Equation (36) for 2-direction, Figure 121.

$$\alpha_1 = \frac{v_f \alpha_{f1} E_{f1} + v_m \alpha_m E_m}{v_f E_{f1} + v_m E_m}. \quad (35)$$

$$\alpha_2 = v_f \alpha_{f2} \left(1 + \frac{\nu_{f_{12}} \alpha_{f1}}{\rho_f}\right) + v_m \alpha_m (1 + \nu_m). - \left(v_f \nu_{f_{12}} + v_m \nu_m\right) \alpha_1. \quad (36)$$

where:

αf1 – thermal expansion coefficient of the fiber, in the fiber direction;

αf2 – thermal expansion coefficient of the fiber perpendicular to the fiber direction; αm – thermal expansion coefficient of the matrix;

vf – fibre volume fraction;

vm – matrix volume fraction;

Ef1 – Young's modulus of the fiber, along the fiber direction;

Em – Young's modulus of the matrix;

νf12 – Poisson's ratio of the fiber;

νm – Poisson's ratio of the matrix;

ρf – density of the fiber.

Once the thermal expansion coefficients are determined in local coordinates (1-2) for individual plies and based on a predefined stacking sequence, the thermal expansion coefficients of the laminate in global coordinates α_x, α_y and α_{xy} may be determined using Equation (37). In Equation (37), A represents the extensional stiffness matrix, calculated using Equation 4.

$$\begin{Bmatrix} \alpha_x \\ \alpha_y \\ \alpha_{xy} \end{Bmatrix} = 0.5[\square]^{-1} \begin{bmatrix} K_1 V_{0A} + K_2 V_{1A} \\ K_1 V_{0A} - K_2 V_{1A} \\ K_3 V_{2A} \end{bmatrix}. \quad (37)$$

$$A = \begin{bmatrix} A_{11} & A_{12} & A_{16} \\ A_{12} & A_{22} & A_{26} \\ A_{16} & A_{26} & A_{66} \end{bmatrix}. \quad (38)$$

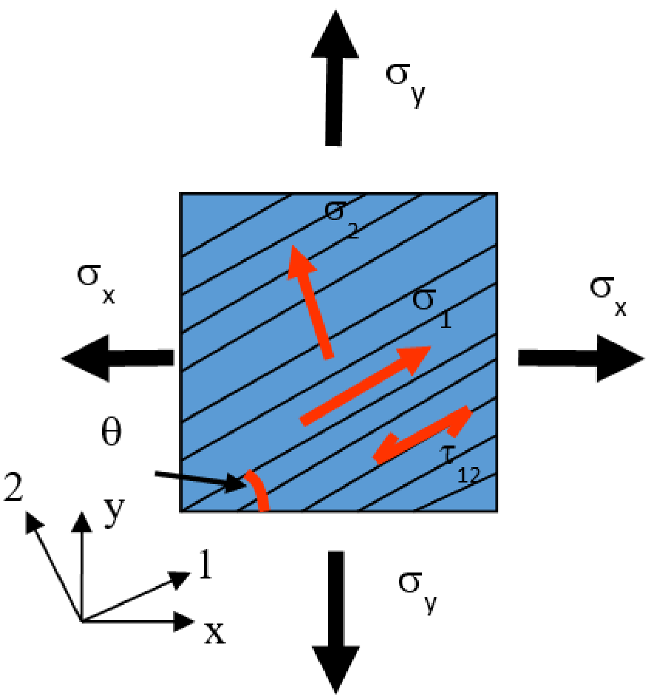

Figure 121 Local and global coordinates of the lamina

Equations (39) to (44) represent the components of the extensional stiffness matrix A:

$$A_{11} = U_1 V_{0A} + U_2 V_{1A} + U_3 V_{3A} \tag{39}$$

$$A_{22} = U_1 V_{0A} - U_2 V_{1A} + U_3 V_{3A} \tag{40}$$

$$A_{12} = U_4 V_{0A} - U_3 V_{3A} \tag{41}$$

$$A_{66} = U_5 V_{0A} - U_3 V_{3A} \tag{42}$$

$$A_{16} = 0.5 U_2 V_{2A} + U_3 V_{4A} \tag{43}$$

$$A_{26} = 0.5 U_2 V_{2A} - U_3 V_{4A} \tag{44}$$

with:

$$V_{0A} = h \tag{45}$$

$$V_{1A} = \sum_{k=1}^{n} t_k \, cos\, 2\, \theta_k \tag{46}$$

$$V_{2A} = \sum_{k=1}^{n} t_k \, sin\, 2\, \theta_k \tag{47}$$

$$V_{3A} = \sum_{k=1}^{n} t_k \, cos\, 4\, \theta_k \tag{48}$$

$$V_{4A} = \sum_{k=1}^{n} t_k \, sin\, 4\, \theta_k \tag{49}$$

where:

h – represents the total thickness of the laminate;

n – represents the number of lamina;

θk – represents the orientation angle of the kth lamina.

$$U_1 = \frac{1}{8}(3Q_{11} + 3Q_{22} + 2Q_{12} + 4Q_{66}) \tag{50}$$

$$U_2 = \frac{1}{2}(Q_{11} - Q_{22}) \tag{51}$$

$$U_3 = \frac{1}{8}(Q_{11} + Q_{22} - 2Q_{12} - 4Q_{66}) \tag{52}$$

$$U_4 = \frac{1}{8}(Q_{11} + Q_{22} + 6Q_{12} - 4Q_{66}) \tag{53}$$

$$U_5 = \frac{1}{8}(Q_{11} + Q_{22} - 2Q_{12} + 4Q_{66}) \tag{54}$$

$U_1 \ldots U_5$ represents the Tsai-Pagano material invariants (Tsai & Melo, 2014) and they are calculated through Equations (50)-(54), where:

$$Q_{11} = \frac{E_1}{(1 - \nu_{12}\nu_{21})} \tag{55}$$

$$Q_{22} = \frac{E_2}{(1 - \nu_{12}\nu_{21})} \tag{56}$$

$$Q_{12} = \frac{\nu_{12}E_2}{(1 - \nu_{12}\nu_{21})} \tag{57}$$

$$Q_{66} = G_{12} \tag{58}$$

K1, K2, K3 from equation (37) represent the thermal material constants, defined through the Tsai-Pagano constants by Equations (59)-(61).

$$K_1 = (U_1 + U_4).(\alpha_1 + \alpha_2) + U_2(\alpha_1 - \alpha_2) \tag{59}$$

$$K_2 = U_2(\alpha_1 + \alpha_2) + (U_1 + 2U_3 - U_4)(\alpha_1 - \alpha_2) \tag{60}$$

$$K_3 = U_2.(\alpha_1 + \alpha_2) + 2(U_3 + U_5)(\alpha_1 - \alpha_2) \tag{61}$$

A hybrid connection is considered as a study case, where a metal shaft component with the external radius R2 = 50 mm is fixed inside a Carbon Fibre Reinforced Plastics tube, having the interior radius of R1 = 50 mm (Figure 122).

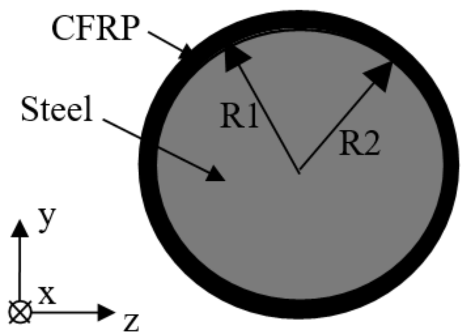

Figure 122 Hybrid steel-composite connection

Let us consider that this assembly will operate in a range of temperatures from 20 to 200 Celsius degrees. In terms of the thermal expansion coefficients, thermal deformations will occur in both materials, according to Equation (62).

$$\Delta R = \alpha_y R \Delta T. \tag{62}$$

While for steel, polymer matrix and carbon fiber the thermal expansion coefficients are known, Table 13, in case of the CFRP laminates the thermal expansion coefficient will strongly be influenced by the individual properties of the matrix and fiber and also by the plies' orientation angles (Marín et al., 2012), (Equations (1) and (2)).

Table 13 Thermal expansion coefficients (Åström, 2002)

Thermal expansion [1/°C]	**Steel**	**Carbon fibre**	**Epoxy resin**
$\boldsymbol{\alpha}_1$	16E-6	-0.6E-6	55E-6
$\boldsymbol{\alpha}_2$	16E-6	8.5E-6	55E-6

According to the example given above, and considering Equation (62), at 200 Celsius degrees, the radius of the steel part R2 will increase from 50 mm to 50.1449 mm while the radius of the CFRP part R1 will increase from 50 mm to only 50.0071 mm. This means that the steel part will press on the CFRP part and thus generate additional in-plane stress within the structure.

As it can be noticed from Table 13, the steel has a larger thermal expansion coefficient than the fiber but lower than the matrix. Moreover, fiber contracts at high temperatures, having a negative thermal expansion coefficient. To avoid additional stress caused by the larger thermal deformations of the steel part in comparison to the one of the CFRP part, it is therefore important to design the laminate such that it has similar thermal expansion coefficient as the steel has. This problem may be formulated as an optimization problem where the objective is to find the configuration of the laminate that will give the desired thermal expansion coefficient. Considering that fiber and matrix properties are given, Table 1, the problem is reducing to the optimization of the orientation angles θ_k where k=1…n, and n represents the total number of plies.

The mathematical model described above was defined within Excel. HyperStudy software was then used to solve the optimization problem by linking the Excel file to the solver. The objective function consist of reaching a target value of 16E-6 [1/°C] for α_y – thermal expansion along Y direction of the composite laminate, Figure 121, and thus to obtain the same thermal deformation as steel along the radial direction of the tube, Figure 122. The predefined stacking sequence is $[45/-45/45/-45/45/-45]_S$ which represents a symmetric laminate with 12 layers. θ_k represents the design variables; the laminate being symmetric, we have only 6 different θ angles as independent variables. The in-plane stiffness parameters of the laminate Ex and Ey are also considered within the optimization as constraints: Ex ≥ 10000 MPa and Ey ≥ 10000 MPa.

Figure 123 illustrates the values obtained for αx and αy. As expected, while αy reaches target value of 16E-6 [1/°C], αx is decreasing and becomes negative (the material contracts at high temperatures).

Figure 124 shows the values obtained for the plies' orientation angles that allow obtaining the desired value of α_y. Although the desired thermal expansion behavior is reached, the mechanical properties of the composite laminate are altered along Y-direction due to the resulted staking sequence $[20/-20/20/-20/20/-20]_S$.

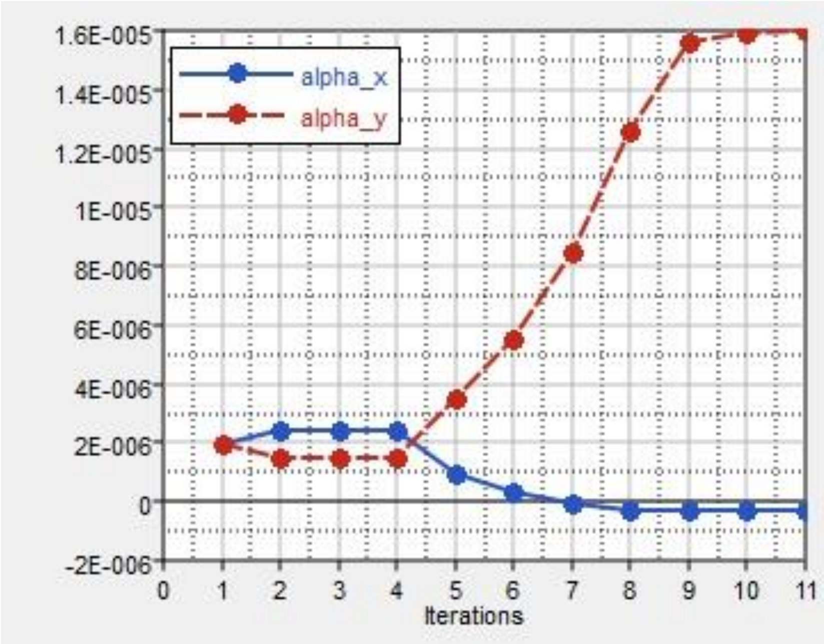

Figure 123 Thermal expansion coefficients of the laminate

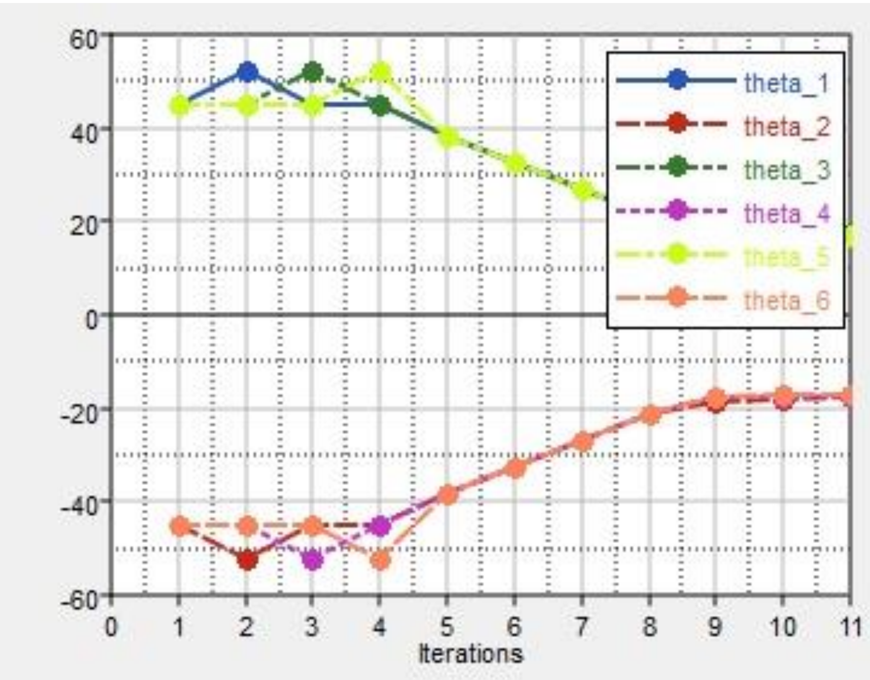

Figure 124 Values of the plies' orientation angles

Figure 125 presents the values obtained for the in-plane stiffness parameters E_x and E_y of the laminate. By looking at both Figure 123 and Figure 125, it turns out that the laminate stiffness increase while the thermal expansion coefficient decrease, along each of the in-plane orthogonal direction X and Y. This observation is also visible from Figure 126 and Figure 127: small values for the thermal expansion coefficients imply large values for the laminate stiffness and vice versa. This behavior is disadvantageous for the here-in-considered case study. A trade of between high stiffness and low thermal expansion coefficient is needed. However, there are situations where high stiffness and low thermal expansion are of interest. Future studies may also consider the stiffness and strength of the laminate along both in-plane directions as objectives to be maximized. A trade-off solution may be selected this way by considering both mechanical and thermal loads.

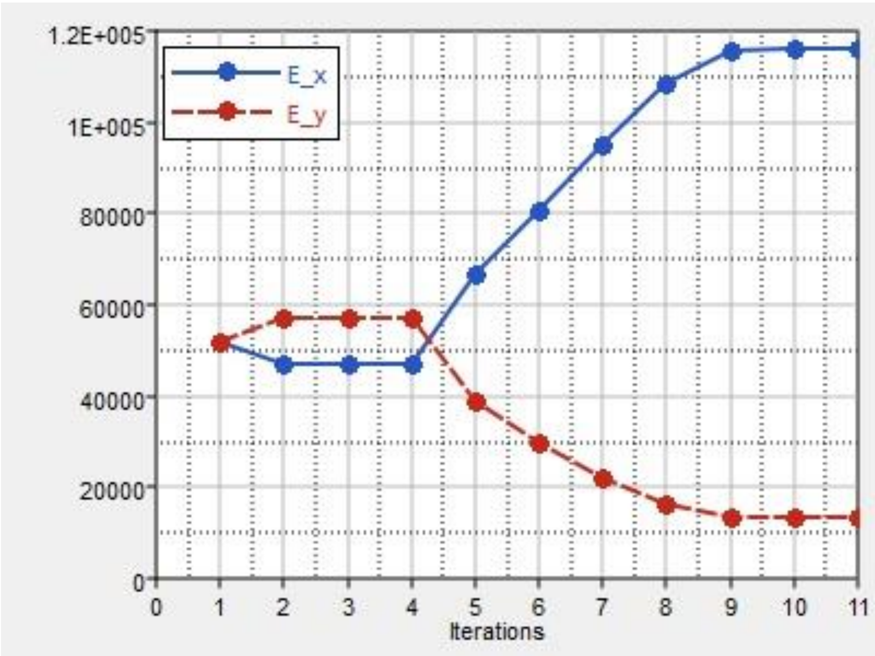

Figure 125 The resulted stiffness of the laminate

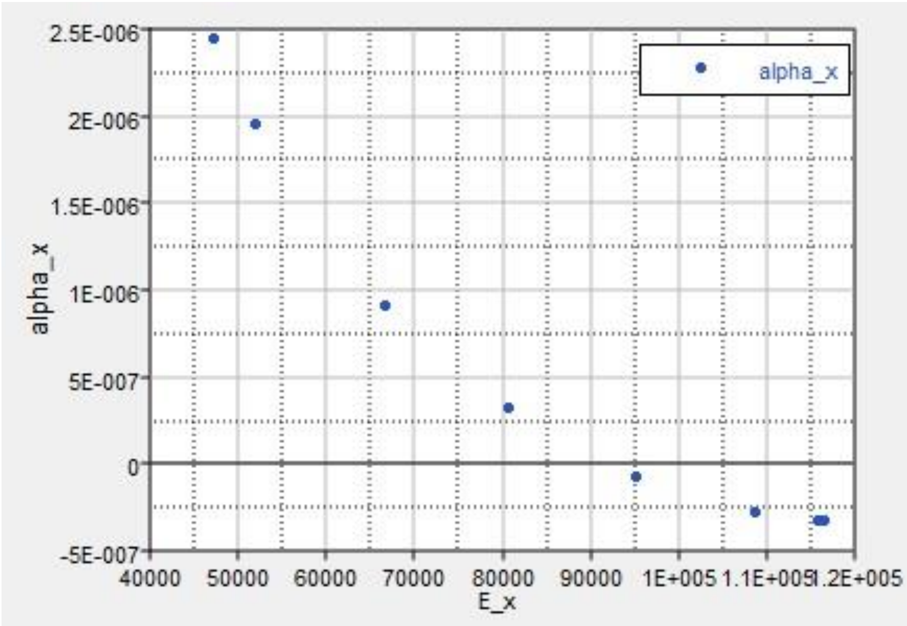

Figure 126 Thermal expansion coefficient αx of the laminate in terms of the laminate stiffness Ex along X-direction

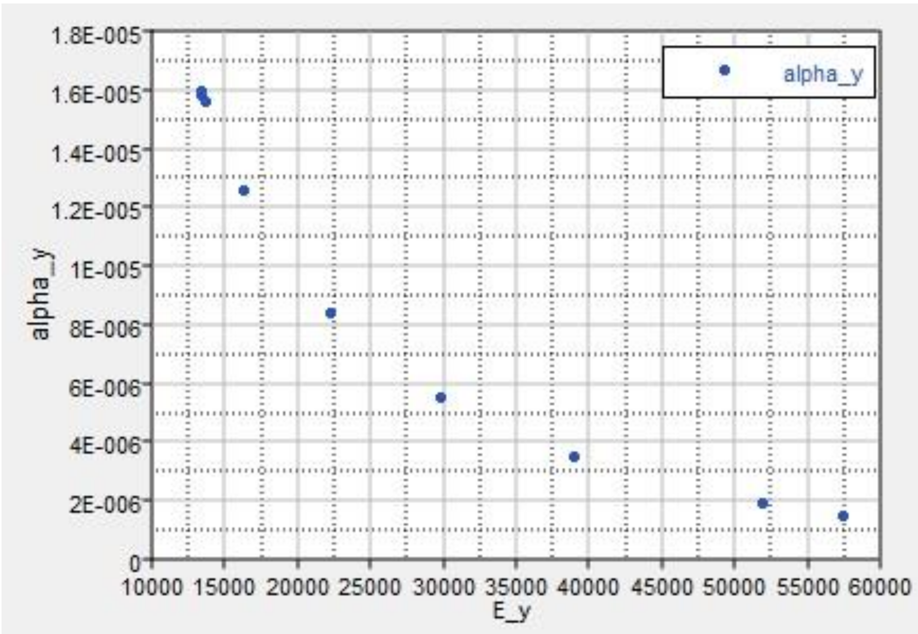

Figure 127 Thermal expansion coefficient αy of the laminate in terms of the laminate stiffness Ey along Y-direction

(B-ii) The evolution and development plans for career development

Evolution

The achievements related to the topics described within the habilitation thesis have started to appear since the university studies when I have developed a new hexagonal open-cell cellular structure produced through a continuous production flow by the mechanical expansion of a flat sheet material. A patent proposal was submitted at that time. Later, within the PhD studies, several scientific articles were published on this topic. This novel cellular structure is used to obtain ultra-lightweight sandwich panels (significant reduction of relative density).

In the final year (fifth), I was the beneficiary of an Erasmus scholarship to develop the diploma project within the lightweight structures group from KU Leuven, Belgium. This work was carried out under the guidance of Professor Dirk Vandepitte. The resulting dissertation was entitled: *Thermoplastic sandwich forming: numerical and experimental research*. During this period of time, I participated at the 8th International Conference on Sandwich Structures, held in Porto in May 2008 where I took the benefit of meeting researchers and industry representatives and thus having the opportunity to identify the actual directions of interest in lightweight structures.

Although I was proposed to start my doctoral studies at KU Leuven, I enrolled into a PhD program in Romania, Brasov, in 2008, under the supervision of Professor Simona Lache. As a PhD student, I visited (for a total time of 4 months) the Lightweight Structures research group from KTH - Royal Institute of Technology, Sweden, led at that time by Professor Stefan

Halstrom. There I took the benefit of being guided by Professor Dan Zenkert and by Professor Per Wennhage. In 2011, before the doctoral thesis defense, I participated at the International Exhibition of Inventions from Geneva, where my invention entitled *Sandwich panel with expanded cellular core* was awarded the gold medal.

The public defense of my PhD thesis, entitled *Advanced cellular structures for the construction of sandwich panels*, took place in September 2011.

In March 2012 I was employed as a researcher, for 1.5 years, at KTH - Royal Institute of Technology, where I worked with Professor Dan Zenkert and Professor Per Wennhage within a project related to the optimization of the composite body of an electric vehicle (ZBee – www.cleanmotion.se). I was responsible for the multi-objective optimization of the composite structure. Based on the research conducted during this time, the team published, within the Composite Structures journal, the article entitled *Multi-objective optimization of vehicle bodies made of FRP sandwich structures* (Velea et al., 2014)

In July 2013 I have been employed as an Assistant Professor within the Department of Mechanical Engineering at Transilvania University of Braşov. Besides teaching activities related to composite materials (new manufacturing technologies, modelling the composite materials and structures, strength of materials), I collaborated with colleagues from Transilvania University of Brasov and researchers from University of Cambridge and from KTH to analyze the behavior of lightweight structures made of reinforced thermoplastic material where the fibers and the matrix are made from the same polymer - PET. Related to this topic, the team published several articles among which the most significant are: (Schneider, Velea, et al., 2015; Velea et al., 2016; Velea & Lache, 2019b).

Between February 2015 and November 2021, I collaborated with Schaeffler Romania in the field of lightweight structures. More specifically, I was working on the development of new lightweight products for the automotive industry including concept proposals, pre-development, and technical calculations of composite structures.

The collaboration with Schaeffler Romania is still on ongoing but in the field of software development – software tools for calculating and optimizing mechanical systems.

In 2018 I have been promoted to Associate Professor, being responsible for teaching topics such as: Lightweight Structures, Structural Optimization, The Optimization of Mechanical Systems, Applied informatics, Strength of Materials.

Since 2018 I have been also the coordinator of the master program entitled Simulation and Testing in Mechanical Engineering.

Development plans for career development

Related to **scientific research**, the following objectives are pursued to develop the university career:

- Enlarging the existing research group with scientific interests and objectives in the field of light structures and optimization methods;
- creating and maintaining professional links with researchers from other European countries; attracting funds from research grants;
- collaboration with the national economic environment in order to regain trust into the Romanian academic sphere, and to provide success collaboration stories regarding transfer of knowledge to industry;
- capitalizing on research results by publishing scientific papers in international journals;
- protecting and exploiting the results of research with economic potential by obtaining invention patents and carrying out technological transfer to the industrial environment.

From a **didactic perspective**, the development plan of the university career is centered on the approach of a particular style of teaching - learning - evaluation that includes the following characteristics:

The teaching process

- aims to motivate and attract students by highlighting the practical implications of the taught subjects;
- presents an interdisciplinary approach, facilitating the creation of connections between the knowledge accumulated by students in other disciplines and those to be acquired;
- includes the invitation of external specialists from the research or industry environment in the course/seminar/laboratory hours to reinforce and demonstrate through practical, real examples, how to use the concepts presented in the taught subjects;
- includes the presentation of the objectives at the beginning of the semester, thus allowing the student to be easily anchored in the new concepts presented during the course/seminar/laboratory classes.

The learning process

- it follows the development of the students' practical spirit simultaneously with the transmission of the theoretical framework;
- it is achieved by empowering students by assigning them work assignments with results that are easy to interpret and transpose into reality;
- it involves the organization of scientific events in which students are encouraged to solve practical problems from the thematic area of the taught subjects.

The evaluation process

- presents an objective character, presenting the real stage of professional development of each student;
- the evaluation criteria are built based on the objectives established in the teaching process.

Continuous preparation and updating of the information package taught through the acquisition of new scientific and educational knowledge and skills, as well as an evolution on the professional university levels in accordance with the results obtained along the way, are taken into consideration.

The involvement in **management activities** will be carried on and extended as needed in the appropriate context.

(B-iii) Bibliography

Almeida, F. S., & Awruch, A. M. (2009). Design optimization of composite laminated structures using genetic algorithms and finite element analysis. *Composite Structures*, *88*(3), 443–454. https://doi.org/http://dx.doi.org/10.1016/j.compstruct.2008.05.004

Altair. (2014). *HyperWorks 13, Online Help and Documentation*.

An, X., & Fan, H. (2016). Hybrid design and energy absorption of luffa-sponge-like hierarchical cellular structures. *Materials & Design*, *106*, 247–257. https://doi.org/https://doi.org/10.1016/j.matdes.2016.05.110

Armacell Benelux. ArmaFORM PET/AC Technical data, Rue de Trois Entities 9-B-4890 Thimister Clermont. <www.armacell.com> [accessed 02.04.2014]. (n.d.).

Armacell Benelux. ArmaFORM PET/W Technical data, Rue de Trois Entities 9-B-4890 Thimister Clermont. <www.armacell.com> [accessed 02.04.2014]. (n.d.).

Ashby, M. (2011). Hybrid Materials to Expand the Boundaries of Material-Property Space. *Journal of the American Ceramic Society*, *94*(SUPPL. 1), s3–s14. https://doi.org/10.1111/J.1551-2916.2011.04559.X

Ashby, M., A G Evans, N A Fleck, L Gibson, J W Hutchinson, & Wadley, H. (2000). *Metal foams - a design guide*. Butterworth-Heinemann.

Ashby, M. F. (2000). Multi-objective Optimization in Material Design and Selection. *Acta Materialia*, *48*, 359–369. https://doi.org/http://dx.doi.org/10.1016/S1359-6454(99)00304-3

Ashby, M. F. (2011). *Materials Selection in Mechanical Design* (Fourth). Elsevier Butterworth-Heinemann.

Ashby, M. F. (2013). Designing architectured materials. *Scripta Materialia*, *68*(1), 4–7. https://doi.org/10.1016/j.scriptamat.2012.04.033

Ashby, M. F., & Bréchet, Y. J. M. (2003). Designing hybrid materials. *Acta Materialia*, *51*(19), 5801–5821. https://doi.org/10.1016/s1359-6454(03)00441-5

Åström, B. T. (2002). *Manufacturing of Polymer Composites*. Nelson Thornes Ltd.

Badalló, P., Trias, D., Marín, L., & Mayugo, J. A. (2013). A comparative study of genetic algorithms for the multi-objective optimization of composite stringers under compression loads. *Composites Part B: Engineering*, *47*(0), 130–136. https://doi.org/http://dx.doi.org/10.1016/j.compositesb.2012.10.037

Baroutaji, A., Sajjia, M., & Olabi, A.-G. (2017). On the crashworthiness performance of thin-walled energy absorbers: Recent advances and future developments. *Thin-Walled Structures*, *118*, 137–163. https://doi.org/https://doi.org/10.1016/j.tws.2017.05.018

Barthelat, F. (2015). Architectured materials in engineering and biology: fabrication, structure, mechanics and performance. *International Materials Reviews*, *60*(8), 413–430. https://doi.org/10.1179/1743280415Y.0000000008

Cavazzuti, M., Baldini, A., Bertocchi, E., Costi, D., Torricelli, E., & Moruzzi, P. (2011). High performance automotive chassis design: a topology optimization based approach. *Structural and Multidisciplinary Optimization*, *44*(1), 45–56. https://doi.org/10.1007/s00158-010-0578-7

Cervellera, P., Zhou, M., & Schram, U. (2005). Optimization driven design of shell structures under stiffness, strength and stability requirements. *6th World Congress of Structural and Multidisciplinary Optimization*.

Comfil® APS. Thermoplastic Composites Denmark, 08.2013, www.comfil.biz, D. K. 8883 G. (2014). *No Title*.

Costas, M., Morin, D., Langseth, M., Díaz, J., & Romera, L. (2017). Static crushing of aluminium tubes filled with PET foam and a GFRP skeleton. Numerical modelling and multiobjective optimization. *International Journal of Mechanical Sciences*, *131–132*, 205–217. https://doi.org/https://doi.org/10.1016/j.ijmecsci.2017.07.004

Costas, M., Morin, D., Langseth, M., Romera, L., & Díaz, J. (2016). Axial crushing of aluminum extrusions filled with PET foam and GFRP. An experimental investigation. *Thin-Walled Structures*, *99*, 45–57. https://doi.org/https://doi.org/10.1016/j.tws.2015.11.003

Cote, F., Deshpande, V. S., Fleck, N. A., & Evans, A. G. (2004). The Out-of-Plane Compressive Behavior of Metallic Honeycombs. *Materials Science and Engineering A*, *380*, 272–280.

Dassault Systemes, A. A. U. M. (n.d.). Prescribed Conditions, Constraints & Interactions. In *Abaqus Analysis User's Manual: Vol. V*. Dassault Systèmes.

Deb, K. (2011). Multi-objective Optimisation Using Evolutionary Algorithms: An Introduction. In L. Wang, A. H. C. Ng, & K. Deb (Eds.), *Multi-objective Evolutionary Optimisation for Product Design and Manufacturing* (pp. 3–34). Springer London. https://doi.org/10.1007/978-0-85729-652-8_1

Dima, D. G., Dobre, F., Velea, M. N., & Dima, D. (2016). *Kugelgewindetrieb* (Patent DE102017114852A1;RO132354A2).

Dima, D., & Velea, M. (2016). *Radflansch und Verfahren zur Herstellung des Radflansches* (Patent DE102016205493A1).

Dragoni, E. (2013). Optimal mechanical design of tetrahedral truss cores for sandwich constructions. *Journal of Sandwich Structures and Materials*, *15*(4), 464–484. https://doi.org/10.1177/1099636213487364

Duddeck, F. (2008). Multidisciplinary optimization of car bodies. *Structural and Multidisciplinary Optimization*, *35*(4), 375–389. https://doi.org/10.1007/s00158-007-0130-6

Fan, H., Qu, Z., Xia, Z., & Sun, F. (2014). Designing and compression behaviors of ductile hierarchical pyramidal lattice composites. *Materials & Design*, *58*, 363–367. https://doi.org/https://doi.org/10.1016/j.matdes.2014.01.011

Fang, J., Sun, G., Qiu, N., Pang, T., Li, S., & Li, Q. (2018). On hierarchical honeycombs under out-of-plane crushing. *International Journal of Solids and Structures*, *135*, 1–13. https://doi.org/https://doi.org/10.1016/j.ijsolstr.2017.08.013

Gibson, L. J., & Ashby, M. F. (1999). *Cellular Solids. Structure and Properties* (2nd ed.). Cambridge University Press.

Harris, J. A., Winter, R. E., & McShane, G. J. (2017). Impact response of additively manufactured metallic hybrid lattice materials. *International Journal of Impact Engineering*, *104*, 177–191. https://doi.org/https://doi.org/10.1016/j.ijimpeng.2017.02.007

Harte, A. M., McNamara, J. F., & Roddy, I. D. (2004). A multilevel approach to the optimisation of a composite light rail vehicle bodyshell. *Composite Structures*, *63*(3–4), 447–453. https://doi.org/http://dx.doi.org/10.1016/S0263-8223(03)00193-4

Kaufmann, M., Zenkert, D., & Wennhage, P. (2010). Integrated cost/weight optimization of aircraft structures. *Structural and Multidisciplinary Optimization*, *41*(2), 325–334. http://dx.doi.org/10.1007/s00158-009-0413-1

Kazemahvazi, S., Russell, B. P., & Zenkert, D. (2012). Impact of carbon fibre/epoxy corrugated cores. *Composite Structures*, *94*(11), 3300–3308. https://doi.org/http://dx.doi.org/10.1016/j.compstruct.2012.04.034

Kazemahvazi, S., Schneider, C., & Deshpande, V. S. (2015a). A constitutive model for self-reinforced ductile polymer composites. *Composites Part A: Applied Science and Manufacturing*, *71*, 32–39. https://doi.org/https://doi.org/10.1016/j.compositesa.2015.01.003

Kazemahvazi, S., Schneider, C., & Deshpande, V. S. (2015b). A constitutive model for self-reinforced ductile polymer composites. *Composites Part A: Applied Science and Manufacturing*, *71*(0), 32–39. https://doi.org/http://dx.doi.org/10.1016/j.compositesa.2015.01.003

Kazemahvazi, S., Schneider, C., & Deshpande, V. S. (2015c). A constitutive model for self-reinforced ductilepolymer composites. *Composite Part A: Applied Science and Manufacturing*, *71*, 32–39.

Kazemahvazi, S., Tanner, D., & Zenkert, D. (2009). Corrugated all-composite sandwich structures. Part 2: Failure mechanisms and experimental programme. *Composites Science and Technology*, *69*(7–8), 920–925. http://www.sciencedirect.com/science/article/B6TWT-4V47CJG-1/2/4b6110f9ac87211ac1ea338cb40c2187

Kazemahvazi, S., & Zenkert, D. (2009). Corrugated all-composite sandwich structures. Part 1: Modeling. *Composites Science and Technology*, *69*(7–8), 913–919. http://www.sciencedirect.com/science/article/B6TWT-4V42JC9-4/2/0a3a64143827b18904daf272fe3f3ebc

Konak, A., Coit, D. W., & Smith, A. E. (2006). Multi-objective optimization using genetic algorithms: A tutorial. *Reliability Engineering & System Safety*, *91*(9), 992–1007. https://doi.org/http://dx.doi.org/10.1016/j.ress.2005.11.018

Kooistra, G. W., Deshpande, V., & Wadley, H. N. G. (2007). Hierarchical Corrugated Core Sandwich Panel Concepts. *Journal of Applied Mechanics*, *74*(2), 259–268.

Kooistra, G. W., & Wadley, H. N. G. (2007). Lattice truss structures from expanded metal sheet. *Materials & Design*, *28*(2), 507–514. http://www.sciencedirect.com/science/article/B6TX5-4HBSGN2-2/2/e96866708716e90410af368f9ee88b02

LANTOR. (2011). *Data Sheet - Lantor Soric XF* .

Lee, D. S., Morillo, C., Bugeda, G., Oller, S., & Onate, E. (2012). Multilayered composite structure design optimisation using distributed/parallel multi-objective evolutionary algorithms. *Composite Structures*, *94*(3), 1087–1096. https://doi.org/http://dx.doi.org/10.1016/j.compstruct.2011.10.009

Lee, S., & Espinosa, H. D. (2005). *DYNAMIC FAILURE OF METALLIC CELLULAR MATERIALS*.

Marín, L., Trias, D., Badalló, P., Rus, G., & Mayugo, J. A. (2012). Optimization of composite stiffened panels under mechanical and hygrothermal loads using neural networks and genetic algorithms. *Composite Structures*, *94*(11), 3321–3326. https://doi.org/http://dx.doi.org/10.1016/j.compstruct.2012.04.024

Marler, R., & Arora, J. (2010). The weighted sum method for multi-objective optimization: new insights. *Structural and Multidisciplinary Optimization*, *41*, 853–862. http://dx.doi.org/10.1007/s00158-009-0460-7

Marler, R. T., & Arora, J. S. (2004). Survey of multi-objective optimization methods for engineering. *Structural and Multidisciplinary Optimization*, *26*(6), 369–395. http://dx.doi.org/10.1007/s00158-003-0368-6

McKown, S., Shen, Y., Brookes, W. K., Sutcliffe, C. J., Cantwell, W. J., Langdon, G. S., Nurick, G. N., & Theobald, M. D. (2008). The quasi-static and blast loading response of lattice structures. *International Journal of Impact Engineering*, *35*(8), 795–810. https://doi.org/https://doi.org/10.1016/j.ijimpeng.2007.10.005

Nagel, G. (n.d.). *Impact and Energy Absorption of Straight and Tapered Rectangular Tubes*.

Papalambros, P. Y., & Wilde, D. J. (1988). *Principles of Optimal Design. Modelling and Computation*. Cambridge University Press.

Poulikidou, S., Schneider, C., Björklund, A., Kazemahvazi, S., Wennhage, P., & Zenkert, D. (2015). A material selection approach to evaluatematerial substitution for minimizing the lifecycle environmental impact of vehicles. *Materials & Design*, *83*, 704–712.

Queheillalt, D. T., Murty, Y., & Wadley, H. N. G. (2008). Mechanical Properties of an Exdruded Pyramidal Lattice Truss Sandwich Structure. *Scripta Materialia*, *58*, 76–79.

Rezaei, R., Karamooz Ravari, M. R., Badrossamay, M., & Kadkhodaei, M. (2016). Mechanical characterization and finite element modeling of polylactic acid BCC-

Z cellular lattice structures fabricated by fused deposition modeling. *Proceedings of the Institution of Mechanical Engineers, Part C: Journal of Mechanical Engineering Science*. https://doi.org/10.1177/0954406215626941

Russell, B. P., Liu, T., Fleck, N. A., & Deshpande, V. S. (2011). Quasi-static three-point bending of carbon fiber sandwich beams with square honeycomb cores. *Journal of Applied Mechanics, Transactions ASME*, *78*.

Russell, B. P., Malcom, A., Wadley, H. N. G., & Deshpande, V. S. (2010). Dynamic compressive response of composite corrugated cores. *Journal of Mechanics of Materials and Structures*, *5*(3).

Schneider, C., Kazemahvazi, S., Åkermo, M., & Zenkert, D. (2013). Compression and tensile properties of self-reinforced poly(ethylene terephthalate)-composites. *Polymer Testing*, *32*(2), 221–230. https://doi.org/http://dx.doi.org/10.1016/j.polymertesting.2012.11.002

Schneider, C., Kazemahvazi, S., Russell, B. P., Zenkert, D., & Deshpande, V. S. (2016). Impact response of ductile self-reinforced composite corrugated sandwich beams. *Composites Part B: Engineering*, *99*, 121–131. https://doi.org/http://dx.doi.org/10.1016/j.compositesb.2016.06.046

Schneider, C., Kazemahvazi, S., Zenkert, D., & Deshpande, V. S. (2015). Dynamic compression response of selfreinforcedpoly(ethylene terephthalate)composites and corrugated sandwich cores. *Composite Part A: Applied Science and Manufacturing*, *77*(96–105).

Schneider, C., Velea, M. N., Kazemahvazi, S., & Zenkert, D. (2015). Compression properties of novel thermoplastic carbon fibre and poly-ethylene terephthalate fibre composite lattice structures. *Materials and Design*, *65*, 1110–1120. https://doi.org/10.1016/j.matdes.2014.08.032

Sebaey, T. A., & Mahdi, E. (2017). Crushing behavior of a unit cell of CFRP lattice core for sandwich structures' application. *Thin-Walled Structures*, *116*, 91–95. https://doi.org/https://doi.org/10.1016/j.tws.2017.03.016

Shin, K. B., Lee, J. Y., & Cho, S. H. (2008). An Experimental Study of Low-Velocity Impact Responses of Sandwich Panels for Korean Low Floor Bus. *Composite Structures*, *84*, 228–240.

Smith, M., Cantwell, W. J., Guan, Z., Tsopanos, S., Theobald, M. D., Nurick, G. N., & Langdon, G. S. (2011). The quasi-static and blast response of steel lattice structures. *Journal of Sandwich Structures & Materials*, *13*(4), 479–501. https://doi.org/10.1177/1099636210388983

Sun, F., Lai, C., Fan, H., & Fang, D. (2016). Crushing mechanism of hierarchical lattice structure. *Mechanics of Materials*, *97*, 164–183. https://doi.org/https://doi.org/10.1016/j.mechmat.2016.02.016

Sun, G., Jiang, H., Fang, J., Li, G., & Li, Q. (2016). Crashworthiness of vertex based hierarchical honeycombs in out-of-plane impact. *Materials & Design*, *110*, 705–719. https://doi.org/https://doi.org/10.1016/j.matdes.2016.08.032

Sun, Y., & Gao, L. (2013). Structural responses of all-composite improved-pyramidal truss sandwich cores. *Materials & Design*, *43*(0), 50–58. https://doi.org/http://dx.doi.org/10.1016/j.matdes.2012.06.033

Sypeck, D. J., & Wadley, H. N. G. (2001). Multifunctional microtruss laminates: Textile synthesis and properties. *J. Mater. Res.*, *16*(3).

Tancogne-Dejean, T., Spierings, A. B., & Mohr, D. (2016). Additively-manufactured metallic micro-lattice materials for high specific energy absorption under static and dynamic loading. *Acta Materialia*, *116*, 14–28. https://doi.org/https://doi.org/10.1016/j.actamat.2016.05.054

Tsai, S. W., & Melo, J. D. D. (2014). An invariant-based theory of composites. *Composites Science and Technology*, *100*(0), 237–243. https://doi.org/http://dx.doi.org/10.1016/j.compscitech.2014.06.017

Ullah, I., Brandt, M., & Feih, S. (2016). Failure and energy absorption characteristics of advanced 3D truss core structures. *Materials & Design*, *92*, 937–948. https://doi.org/https://doi.org/10.1016/j.matdes.2015.12.058

Velea, M. N., & Lache, S. (2011). In-plane effective elastic properties of a novel cellular core for sandwich structures. *Mechanics of Materials*, *43*(7), 377–388. https://doi.org/10.1016/j.mechmat.2011.04.006

Velea, M. N., & Lache, S. (2015). Thermal expansion of composite laminates. *Bulletin of the Transilvania University of Braşov, Series I: Engineering Sciences*, *8 (57)*(1).

Velea, M. N., & Lache, S. (2018). Failure mode maps of a hierarchical sandwich structure made of self-reinforced PET. *AIP Conference Proceedings*, *1932*. https://doi.org/10.1063/1.5024172

Velea, M. N., & Lache, S. (2019a). Energy absorption of all-PET 2nd order hierarchical sandwich structures under quasi-static loading conditions. *Thin-Walled Structures*, *138*. https://doi.org/10.1016/j.tws.2019.01.039

Velea, M. N., & Lache, S. (2019b). Energy absorption of all-PET 2nd order hierarchical sandwich structures under quasi-static loading conditions. *Thin-Walled Structures*, *138*, 117–123. https://doi.org/10.1016/J.TWS.2019.01.039

Velea, M. N., Lache, S., & Frincu, D. (2018). *Sandwich structure with triangular prism-shaped primary core and process for making the same* (Patent RO130161B1). OSIM Romania.

Velea, M. N., Schneider, C., & Lache, S. (2016). Second order hierarchical sandwich structure made of self-reinforced polymers by means of a continuous folding process. *Materials and Design*, *102*. https://doi.org/10.1016/j.matdes.2016.04.049

Velea, M. N., Wennhage, P., & Lache, S. (2012). Out-of-plane effective shear elastic properties of a novel cellular core for sandwich structures. *Materials and Design*, *36*, 679–686. https://doi.org/10.1016/j.matdes.2011.12.017

Velea, M. N., Wennhage, P., & Zenkert, D. (2014). Multi-objective optimisation of vehicle bodies made of FRP sandwich structures. *Composite Structures*, *111*(1), 75–84. https://doi.org/10.1016/j.compstruct.2013.12.030

Vinson, J. R. (2005). *Plate and Panel Structures of Isotropic, Composite and Piezoelectric Materials, Including Sandwich Structures*. Springer.

Wadley, H. N. G., & Kooistra, G. W. (2009). *Cellular Lattice Structures With Multiplicity Of Cell Sizes And Related Method Of Use* .

Walker, M., & Smith, R. E. (2003). A technique for the multiobjective optimisation of laminated composite structures using genetic algorithms and finite element analysis. *Composite Structures*, *62*(1), 123–128. https://doi.org/http://dx.doi.org/10.1016/S0263-8223(03)00098-9

Wang, K., Kelly, D., & Dutton, S. (2002). Multi-objective optimisation of composite aerospace structures. *Composite Structures*, *57*(1–4), 141–148. https://doi.org/http://dx.doi.org/10.1016/S0263-8223(02)00078-8

Wang, X., Shen, J., Zuo, Z. H., Huang, X., Zhou, S., & Xie, Y. M. (2015). Numerical investigation of compressive behaviour of luffa-filled tubes. *Composites Part B: Engineering*, *73*, 149–157. https://doi.org/https://doi.org/10.1016/j.compositesb.2014.12.017

Xiao, L., & Song, W. (2018). Additively-manufactured functionally graded Ti-6Al-4V lattice structures with high strength under static and dynamic loading: Experiments. *International Journal of Impact Engineering*, *111*, 255–272. https://doi.org/https://doi.org/10.1016/j.ijimpeng.2017.09.018

Xiong, J., Ma, L., Wu, L., Wang, B., & Vaziri, A. (2010). Fabrication and crushing behavior of low density carbon fiber composite pyramidal truss structures. *Composite Structures*, *92*(11), 2695–2702. https://doi.org/http://dx.doi.org/10.1016/j.compstruct.2010.03.010

Xiong, J., Vaziri, A., Ma, L., Papadopoulos, J., & Wu, L. (2012). Compression and impact testing of two-layer composite pyramidal-core sandwich panels. *Composite Structures*, *94*(2), 793–801. https://doi.org/10.1016/j.compstruct.2011.09.018

Yang, M., & Qiao, P. (2008). Quasi-static Crushing Behavior of Aluminum Honeycomb Materials. *Journal of Sandwich Structures and Materials*, *10*, 133–160.

Yin, S., Wu, L., & Nutt, S. (2013). Stretch–bend-hybrid hierarchical composite pyramidal lattice cores. *Composite Structures*, *98*(0), 153–159. https://doi.org/http://dx.doi.org/10.1016/j.compstruct.2012.11.004

Yin, S., Wu, L., & Nutt, S. R. (2014). Compressive efficiency of stretch–stretch-hybrid hierarchical composite lattice cores. *Materials & Design*, *56*, 731–739. https://doi.org/http://dx.doi.org/10.1016/j.matdes.2013.11.012

Zenkert, D. (1997). The Handbook of Sandwich Construction. In *The Handbook of Sandwich Construction*. Engineering Materials Advisory Services Ltd.

Zhang, G., Wang, B., Ma, L., Xiong, J., & Wu, L. (2013). Response of sandwich structures with pyramidal truss cores under the compression and impact loading. *Composite Structures*, *100*, 451–463. https://doi.org/http://dx.doi.org/10.1016/j.compstruct.2013.01.012

Zhang, J. M., & Peijs, T. (2010). Self-reinforced poly(ethylene terephthalate) composites by hot consolidation of Bi-component PET yarns. *Composites Part A: Applied Science and Manufacturing*, *41*(8), 964–972. https://doi.org/https://doi.org/10.1016/j.compositesa.2010.03.012

Zhang, J. M., Reynolds, C. T., & Peijs, T. (2009). All-poly(ethylene terephthalate) composites by film stacking of oriented tapes. *Composites Part A: Applied Science and Manufacturing*, *40*(11), 1747–1755. https://doi.org/https://doi.org/10.1016/j.compositesa.2009.08.008

Zhang, X., & Zhang, H. (2013). Theoretical and numerical investigation on the crush resistance of rhombic and kagome honeycombs. *Composite Structures*, *96*(0), 143–152. https://doi.org/http://dx.doi.org/10.1016/j.compstruct.2012.09.028

Zhou, C.-C., Yin, G.-F., & Hu, X.-B. (2009). Multi-objective optimization of material selection for sustainable products: Artificial neural networks and genetic algorithm approach. *Materials & Design*, *30*(4), 1209–1215. https://doi.org/10.1016/j.matdes.2008.06.006